Photonic and Device Design Principles for Ultrahigh-Efficiency (>50%), Spectrum-Splitting Photovoltaics

Thesis by
Carissa Nicole Eisler

In Partial Fulfillment of the Requirements
for the Degree of
Doctor of Philosophy

California Institute of Technology
Pasadena, CA
2016
(Defended November 3, 2015)

Abstract

The sun has the potential to power the Earth's total energy needs, but electricity from solar power still constitutes an extremely small fraction of our power generation because of its high cost relative to traditional energy sources. Therefore, the cost of solar must be reduced to realize a more sustainable future. This can be achieved by significantly increasing the efficiency of modules that convert solar radiation to electricity. In this thesis, we consider several strategies to improve the device and photonic design of solar modules to achieve record, ultrahigh ($> 50\%$) solar module efficiencies. First, we investigate the potential of a new passivation treatment, trioctylphosphine sulfide, to increase the performance of small GaAs solar cells for cheaper and more durable modules. We show that small cells (mm^2), which currently have a significant efficiency decrease ($\sim 5\%$) compared to larger cells (cm^2) because small cells have a higher fraction of recombination-active surface from the sidewalls, can achieve significantly higher efficiencies with effective passivation of the sidewalls. We experimentally validate the passivation qualities of treatment by trioctylphosphine sulfide (TOP:S) through four independent studies and show that this facile treatment can enable efficient small devices. Then, we discuss our efforts toward the design and prototyping of a spectrum-splitting module that employs optical elements to divide the incident spectrum into different color bands, which allows for higher efficiencies than traditional methods. We present a design, the polyhedral specular reflector, that has the potential for $> 50\%$ module efficiencies even with realistic losses from combined optics, cell, and electrical models. Prototyping efforts of one of these designs using glass concentrators yields an optical module whose combined spectrum-splitting and concentration should correspond to a record module efficiency of 42%. Finally, we consider how the manipulation of radiatively emitted photons from subcells in multijunction architectures can be used to achieve even higher efficiencies than previously thought, inspiring both optimization of incident and radiatively emitted photons for future high efficiency designs. In this thesis work, we explore novel device and photonic designs that represent a significant departure from current solar cell manufacturing techniques and ultimately show the potential for much higher solar cell efficiencies.

Acknowledgements

I am incredibly grateful to the many people who made this thesis possible because they have helped me grow immensely as a scientist and as a person.

First and foremost, I would like to express my sincere gratitude to my advisor Professor Harry A. Atwater. He has a great intuition for picking interesting and impactful projects and it made my research here so enjoyable. Also, Harry is an enthusiastic and kindhearted person, and he's cultivated such a wonderful group of scientists. I could not imagine a better advisor for my Ph.D studies.

I would also like to thank my committee, Professor Julie Kornfield, Professor Richard Flagan, and Professor Andrei Faraon, for their guidance and encouragement. Discussing my work with them was always an extremely positive experience and I am so appreciative of their invaluable feedback.

I would like to thank the funding resources that made this research possible: DARPA, LMI-EFRC, ARPA-E, Dow Chemical Company, and the National Defense Science & Engineering Graduate Fellowship. In particular, Weijun Zhou and Rebekah Feist provided excellent feedback and support on the Full Spectrum project.

I had the immense honor of being mentored by three amazing postdoctoral researchers during my time here. I am thankful for Professor Robert Macfarlane's advice and optimism for my career after Caltech. To Professor Bethany Theiling, who I met through the Women Mentoring Women program, I feel so lucky to have had such a great role model, both in science and in life. Finally, I am so, so fortunate to have worked with Professor Matthew T. Sheldon. I was always in awe of his boundless curiosity, his endless inspiration for new research, and his ability to engage and educate anyone. He was one of the largest influences on my graduate career and I will forever aspire to be like him.

I was lucky enough to work closely with the Full Spectrum Conversion Team: Sunita Darbe, Michelle Dee, Professor Matt Escarra, Dr. Pilar Espinet, Cris Flowers, Dr. Emily Kosten, John Lloyd, Annabelle Sibué, Dirk-Jan Spaanderman, Dr. Emily Warmann, and Kelsey Whitesell-Horowitz. The work presented in this thesis would not be possible without their ingenuity and perseverance. I owe them all so much and some of my fondest memories at Caltech are of working with them. I am deeply honored to call this brilliant group of scientists my friends. Go Rainbow Warriors!

The Atwater group is composed of an amazing group of people and I have greatly benefitted from each member who has passed through during my time here. I am grateful for Dr. Ragip Pala's advice and experience on setting up the optical characterization for the optical prototype, Dr. Daniel Turner-Evans' guidance in the lab, and Naomi Coronel for being an amazing co-guru on the sputterer. I was lucky enough to work with Bridget Connor, Claire West, Kevin Chen, and Benjamin Clark, who were amazing undergraduate researchers. The women of the Atwater group also periodically organized "Ladies' Nights," which were always fun (and a little wild). In addition to the people already mentioned, Dr. Anna Beck, Ana Brown, Dr. Dennis Callahan, Jim Fakonas, Rebecca 'the younger' Glaudell, Georgia 'Peaches' Papadakis, Dr. Rebecca 'the elder' Saive, Michelle Sherrott, Yulia 'Yule Log' Tolstova, Dr. Krishnan Thyagarajan, Dr. Daniel Turner-Evans, Dr. Raymond Weitekamp, Will Whitney, and Samantha Wilson are dear friends and I appreciate their support.

My sincerest thanks goes to the talented staff of Caltech who would always strive to make the community better. Kathy Bubash has always looked out for me and I will miss her kind and gentle demeanor. I am very indebted to Tiffany Kimoto, Jennifer Blankenship, Liz Jennings, and Lyann Lau, who not only keep the Atwater group running smoothly but have also been fantastic friends who always have time to lend an ear. Thanks to Reginalda Montaya, who was always a happy start to my day, and to Alireza Ghaffari, who does an excellent job managing our lab. I am thankful for Dr. Cassandra Horii of the Center for Teaching, Learning, and Outreach, who has inspired me to be a better educator. I am also thankful to Felicia Hunt and the Caltech Center for Diversity who have been a huge source of positivity in my career. Finally, I am incredibly grateful to Dr. Carrie Hofmann. She does an excellent job of running the LMI-EFRC and has been an amazing mentor to me.

I am so grateful for the many friendships I have made at Caltech. I have so many wonderful memories of the friends I made through my chemical engineering courses: studying together over tea and homemade snacks in our apartments, having wheelie chair races down the halls of Spalding, dressing up as Professor Brady for the last day of class, attempting to surprise each other with birthday cupcakes, and so many more. In particular, Matt Coggon, Phares Carroll, Marilena Dimotsantou, Kat Fang, Zach Gibbs, Wendy Gu, Nick Hoh, Matt Shaner, and Charlie Slominski are friends I will cherish always. Also, I feel incredibly fortunate to call Kelsey Boyle, Holly Ferguson, Andreas Hoenselaar, and Allyson Pellissier my friends and I will forever cherish our time together.

I am so thankful for my support network outside of Caltech. This thesis would not be possible without Brianna and Michael Mowry, whose wonderful friendship has supported me for many, many years. Oksana Prodan and her family have always been such a positive influence and I'm so happy that our families have adopted each other. I am also incredibly lucky to know Tim Jacoby, Jennifer Jung, Marilyn Hin, Vicki Baker, Adrian Borbon, Lauren Chu, and Evan and Joyce Mendelzon, who always look out for me.

My family has always been my biggest source of love and encouragement. Grandma Angie, Aunt Jana, Kerry Decker, Aunt Sue, Uncle Rich, Matt Eisler, and Corinne Eisler always know how to bring a smile to my face. I am immensely grateful to my Aunt Nae, who introduced me to horseback riding, which was essential to my confidence. I am so thankful for my beautiful and kind cousister (cousin whose closeness resembles sisterhood), Devon Yuwiler, who has been an inspiration in all aspects of life. Watching her pursue her dreams has given me the courage to pursue my own. I am also thankful for my cat, Jujubee, who provides me endless joy and has helped me realize my true calling as a "cat lady."

Finally, I would like to thank my partner, Dr. Chris Chen, and my parents, Fred and Michelle Eisler. Chris is one of the most thoughtful people I have ever met and I am always amazed and overwhelmed by his compassion for others. I am very grateful that he and his family are a part of my life. My parents are the primary reason I was able to accomplish my dream of going to graduate school. All of my accomplishments are the product of their selfless love and support. They constantly inspire me to build a better world deserving of people like them. I am so proud and so honored to be their daughter.

Carissa Nicole Eisler
October 2015
Pasadena, CA

Contents

List of Figures

List of Tables

Relevant Publications

Matthew T. Sheldon, Carissa N. Eisler, and Harry A. Atwater. "GaAs Passivation with Trioctylphosphine Sulfide for Enhanced Solar Cell Efficiency and Durability." *Advanced Energy Materials*, 2 (3) : 339-344, 2012.

Carissa N. Eisler, Ze'ev R. Abrams, Matthew T. Sheldon, Xiang Zhang, and Harry A. Atwater. "Multijunction solar cell efficiencies: effect of spectral window, optical environment and radiative coupling." *Energy & Environmental Science*, 7 (11) : 3600-3605, 2014.

Emily C. Warmann, Carissa N. Eisler, Matthew D. Escarra, and Harry A. Atwater. "Design of photovoltaics for modules with 50% efficiency." *Submitted 2015.*

Carissa N. Eisler, Cristofer A. Flowers, Emily C. Warmann, Sunita Darbe, Michelle Dee, Matthew Escarra, Emily Kosten, John Lloyd, and Harry A. Atwater. "The Polyhedral Specular Reflector: A Spectrum-Splitting Multijunction Design to Achieve Ultrahigh (>50%) Solar Module Efficiencies." *In preparation 2015.*

Carissa N. Eisler, Cristofer A. Flowers, John Lloyd, Pilar Espinet-González, Sunita Darbe, and Harry A. Atwater. "Prototyping the Polyhedral Specular Reflector, a Spectrum-Splitting Photovoltaic Module with Seven Independently Connected Subcells." *In preparation 2015.*

Dedicated to Fred and Michelle Eisler, whose endless love and support make anything possible.

Chapter 1

Introduction

1.1 Potential and Challenges for Solar Energy Conversion

The power incident on the Earth's surface from the sun in one year (1.6 $\times 10^5$ TW) dwarfs our total annual power consumption (17.8 TW, 2010) [1]. Additionally, the availability of this power far exceeds the total reserves of all other known energy resources [2]. Photovoltaics, or devices that directly generate electricity from incident solar radiation, are a well-known technology that have been implemented worldwide. Despite the enormous availability of this solar resource, photovoltaics comprise an extremely small fraction of our total power production. In 2014, solar power was responsible for a mere 0.4% of the United States' total energy production [3]. Ultimately, this is a result of the high cost of electricity generated from solar panels as compared to more traditional sources, such as fossil fuels. These technologies are compared through their levelized cost of electricity (LCOE), described below:

$$LCOE = \frac{\text{Total Life Cycle Cost}}{\text{Total Lifetime Energy Production}} \tag{1.1}$$

According to the Department of Energy's predictions for 2018, traditional fossil fuels will achieve LCOEs from \$0.07-0.10 kWh in the United States. While their price has been continuously decreasing, photovoltaics still show a higher LCOE of nearly \$0.15 kWh, owing to the high cost of plant installation [3, 4]. Increasing the efficiency beyond current technologies can increase the total lifetime energy production and dramatically decrease the total LCOE. Therefore, the goal of this thesis work is to understand and address the major fundamental thermodynamic losses in solar energy conversion as a means to enable a large scale, sustainable energy supply.

1.2 Thermodynamics of Solar Cell Conversion

1.2.1 Efficiency Limit of a Single Junction Material

The most basic form of a solar cell is the single junction cell as described by Shockley and Queisser, shown in Figure 1.1 [5]. The cell is composed of one absorbing semiconductor material with a bandgap, E_g, that separates the valence band (states of bound electrons) from the conduction band (states of conducting electrons). The semiconductor absorbs photons with energies greater than or equal to the bandgap that can promote electrons from a bound state to a conducting state, leaving a vacancy known as a 'hole.' The hole can also conduct through the valence band. This separation of the electrons and holes creates a potential, but this potential is inherently limited by the bandgap of the semiconductor because any excess energy is dissipated through lattice vibrations, also known as thermalization. The reverse process, radiative recombination, also occurs: an excited electron recombines with a hole to produce a photon with an energy equivalent to the bandgap. These radiatively emitted photons can be absorbed and reconverted within the same device until they escape from the cell structure. In a perfect material, the only recombination in a material is radiative. Realistic materials, however, have some defect-mediated recombination sites that do not produce a photon and therefore do not have the chance for conversion of the recombined electron-hole pair.

The efficiency of a solar cell is the ratio of its electrical power generated, or the operation voltage times the total current, to the incident power from the sun. The power generated (P) in an ideal cell is given in Equation 1.2 [5, 6].

$$P = VJ = V\left[\int_{E_g}^{\infty} N_{AM1.5G}(E)dE - \frac{2\pi q}{h^3c^2}\int_{E_g}^{\infty}\frac{E^2dE}{exp\left(\frac{E-qV}{kT_o}\right)-1}\right] \tag{1.2}$$

where V is the applied voltage, J is the current density, $N_{AM1.5G}$ is the photon flux as a function of energy in the 1 sun AM1.5G spectrum, q is the charge of an electron, h is Planck's constant, c is the speed of light, k is Boltzmann's constant, and T_o is the temperature of the subcell (300K). The AM1.5G (air mass 1.5 global) is the standard spectrum for characterizing flat plate solar cells. Later, we will use the AM1.5D (air

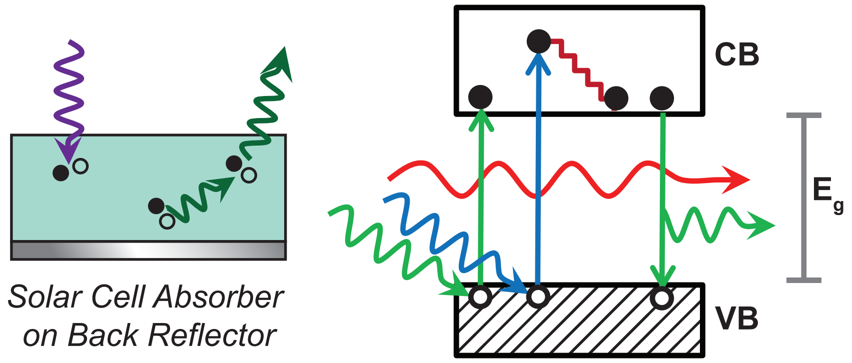

FIGURE 1.1: Schematic of absorption and emission in a basic solar cell and corresponding band diagram. (Left) schematic of a solar cell absorber on a back reflector. Incident photons are absorbed and create an electron-hole pair. Electrons and holes can recombine to form a photon with an energy equivalent to the bandgap, which can be reabsorbed or escape the cell. Here, photons can only escape through the front face because of the back reflector. (Right) Corresponding band diagram. A semiconductor with a bandgap E_g only absorbs photons with energies equal to (green) or greater than (blue) its bandgap while lower energy photons (red) are transmitted. Absorbed photons can promote an electron (solid circle) from the valence band (VB) to the conductor band (CB). A vacancy state, or hole, (empty circle) is left in its place. Excited carriers thermalize to the band edge.

mass 1.5 direct) spectrum for concentrating cells that do not convert the diffuse component. This equation is plotted in Figure 1.2. Intuitively, the total current is the current generated from absorbed photons subtracted by the current from radiative recombination, or dark current. The maximum current for a device, the short circuit current (J_{sc}), occurs when there is no applied voltage and is equal to the current generated from absorbed photons. The maximum voltage, the open-circuit voltage (V_{oc}), occurs when the total current is equal to zero, or when the short circuit current is equal to the dark current. Higher voltages are possible when there is a higher carrier potential, or when the radiative emission escaping the device is minimized. Therefore, a higher voltage is achieved for a solar cell with a back reflector (Figure 1.1) because the cell is able to prevent radiative emission from the rear of the device. The maximum power point occurs when the product of the operating current (J_{mpp}) and voltage (V_{mpp}) is maximized [5–7].

The optimum bandgap for a single junction device represents a trade-off between absorption (current) and carrier potential (voltage). Smaller bandgaps can absorb more of the incident solar spectrum, maximizing J_{sc}, but inherently limit the carrier potential, minimizing V_{oc}. Thus, the optimum bandgap is near the middle of the spectrum at 1.4 eV, yielding a maximum possible efficiency of 33%.

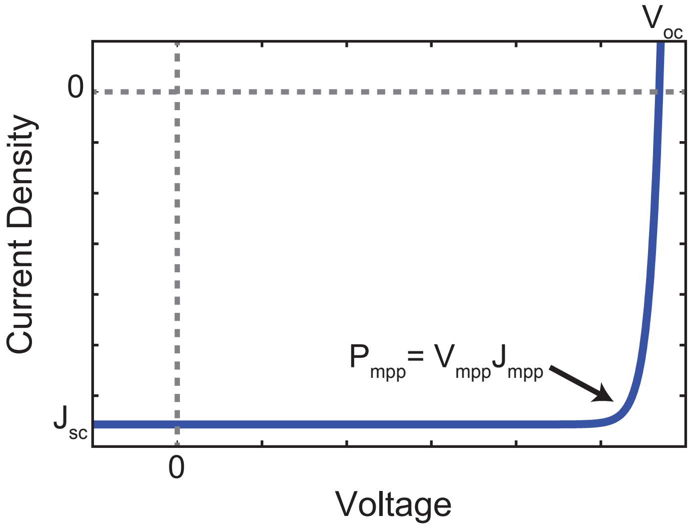

FIGURE 1.2: Ideal current-voltage characteristics of a solar cell with a bandgap of 1.4 eV. The open circuit voltage (V_{oc}), short circuit current (J_{sc}), and maximum power point (P_{mpp}) are labeled.

1.2.2 Breakdown of the Thermodynamic Losses in Solar Cell Conversion

While 33% is the limit for a single junction solar cell, much higher efficiencies are possible. Figure 1.3 plots the current experimental single junction record efficiency (28.8%) versus all of the energetic and entropic losses preventing a solar energy conversion efficiency of 100% [8, 9]. This cell is already approaching the 33% efficiency limit because of high quality material growth and excellent device design. Further improvements in device design, such as better passivation and reduced parasitic absorption losses, can bring the efficiency even closer to this limit [10, 11].

Some of the losses in Figure 1.3 are considered to be inherent in solar energy conversion. Even with a perfect heat engine, the Carnot efficiency between the sun (approximated as 6000K blackbody) and the earth (300K blackbody) is 95%. The maximum efficiency is further reduced to 93%, also known as the Landsberg limit, when semiconductors are used because there is an entropic penalty in transforming electromagnetic energy to excited electrons. Additionally, if only time-symmetric systems are considered, this maximum efficiency is reduced again to 86.8% [7].

However, the largest losses can be addressed with known technologies. The maximum efficiency can be further increased to over 40% by addressing the entropic loss of isotropic radiative emission. Incident sunlight enters the subcell with a small angular spread

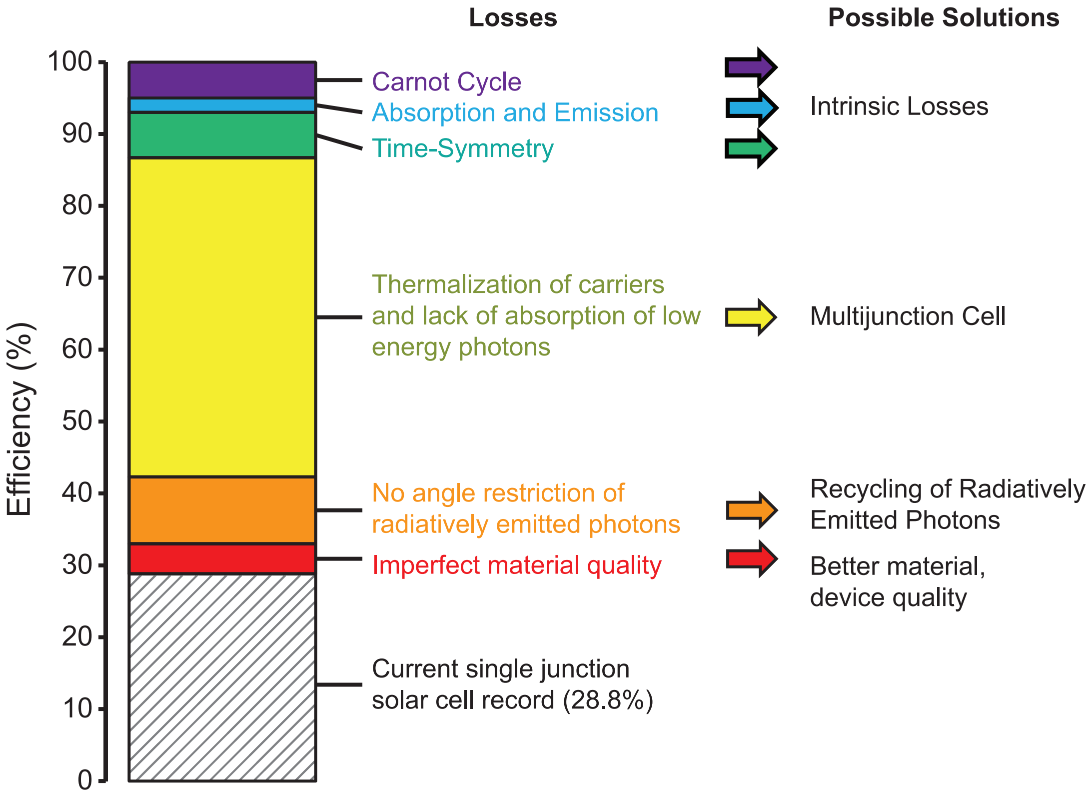

FIGURE 1.3: Bar chart detailing the major thermodynamic losses and possible solutions for solar energy conversion. Energetic and entropic losses are compared to the current record single junction solar cell (GaAs, 28.8%) [8]. Adapted from [9].

(half angle = 0.267°) but radiative emission is an isotropic process. Even if radiatively emitted photons can only escape out of the front of the solar cell by using a back reflector (half angle = 90°), there is still a large entropic loss from losing the directionality of the incident light. This loss can either be addressed by restricting the emission of radiatively emitted photons or by heavily concentrating the incident light [12, 13].

Finally, the largest loss of efficiency is attributed to the thermalization of carriers created from high energy photons and lack of absorption of low energy photons. For a single junction cell, only photons with energies equal to or exceeding the bandgap are absorbed and converted, with any additional energy beyond the bandgap lost as heat to the surrounding lattice. Solar blackbody emission is very broadband and therefore conversion with only a single bandgap is very inefficient. This loss can be minimized by incorporating many cells with different bandgaps, or subcells, thereby increasing the amount of photons absorbed and minimizing the difference between the photon energies and cell bandgaps. A band diagram of a multijunction cell is shown in Figure 1.4. Intuitively, higher efficiencies are achieved with more subcells, and a maximum efficiency of 86.7% occurs with infinite subcells combined with ideal materials and maximum concentration. Thus, realistic solar cells made from high quality materials that minimize thermalization and lack of absorption losses should still have the potential to realize >50% efficiency.

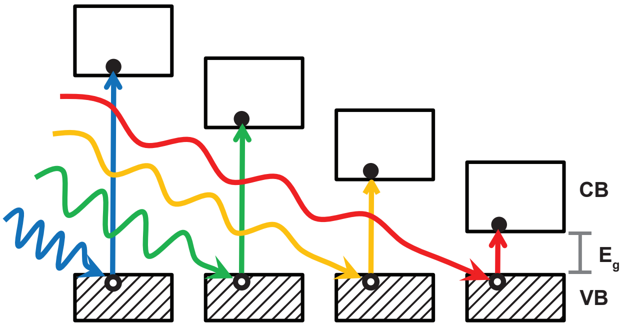

FIGURE 1.4: Band diagram of a multijunction cell. A multijunction cell includes many absorbers with different bandgaps that more efficiently convert a broadband spectrum.

1.3 State-of-the-Art Solar Cell Technologies

As mentioned in the previous section, the current single junction record is 28.8% and was achieved with a GaAs absorber (E_g = 1.42 eV) [8]. This nearly ideal efficiency was achieved through device optimization of the passivating layers and development of epitaxial liftoff [9, 14]. The optimized passivation prevents nonradiative trap states at the front and rear of the device, reducing surface recombination. Growth via epitaxial liftoff, where cell layers are grown on a sacrificial etching layer, allowed for the isolation of a thin ($\sim\mu$m) device that can be mounted on a high quality back reflector to trap some of the radiative emission and prevent parasitic absorption from the growth wafer [10, 11]. However, this efficiency was only demonstrated for a larger sized cell (1 cm^2), indicating that further device design is needed if the cost of the module necessitates smaller cells.

The current record solar efficiency is 46%, made with a multijunction cell composed of four bandgaps under 508x concentration [8]. Like the record single junction cell, they are also created from III-V compound semiconductors. However, the concentration used in the record measurement is artificial, and incorporation of real optics and electronic circuitry into a full module reduces this to a maximum efficiency of 38.9% at 333x concentration [8]. Despite the higher efficiencies attained by these multijunction cells, silicon single junction photovoltaics (20-20% efficiency) are still the dominant technology because they are cheaper to produce relative to the III-V semiconductors [15]. Therefore, even higher efficiencies are required to strongly reduce the LCOE and 50% module efficiency has been identified as a threshold to achieve the desired costs [16]. While significant strides have been made in incorporating many materials, 50% efficiencies, at either the cell or the module level, have not yet been attained using traditional fabrication methods. Therefore, disruptive technologies are required to achieve these ultrahigh (>50%) efficiencies.

1.4 Our Work Toward Ultrahigh Efficiency Solar Cells

This thesis explores several pathways, using device and photonic design principles, to significantly enhance solar cell efficiencies. In Chapter 2, we focus on improving the efficiencies of small GaAs single junction cells. While these devices can achieve extremely high efficiencies at larger sizes (cm^2), we show that the efficiency decreases for smaller sizes (mm^2) due to a lack of passivation of the recombination-heavy sidewalls of the device. We identify a trioctylphosphine sulfide (TOP:S) as a facile chemical treatment for GaAs sidewalls and verify its efficacy through four independent experiments.

Chapter 3 presents the design and optimization of a spectrum-splitting multijunction architecture for achieving ultrahigh efficiencies (>50%). Unlike traditional multijunction cells, a spectrum-splitting module employs the use of an external optical element to divide the incident solar spectrum for conversion by subcells tuned to each band, which allows for even higher efficiencies and annual energy productions than previously thought possible. We discuss the combined cell, optical, and electrical models in optimizing and predicting the module efficiency. We identify our design, the polyhedral specular reflector, as a design capable of 50% efficiency using seven subcells and a series of reflective filters to divide the incident solar spectrum.

Chapter 4 of this thesis presents the experimental efforts to fabricate a spectrum-splitting optic for high solar cell efficiency. We present two optical modules that incorporate long-pass filters and solid concentrators to divide and concentrate the incident solar spectrum into different frequency bands for conversion by the designed subcells of Chapter 3. We show that a prototype fabricated with excellent quality filters, highly transparent glass concentrators, and good alignment achieves an optical efficiency of 80%, which corresponds to a potential module efficiency of 42%.

Finally, Chapter 5 discusses design principles for future, ultrahigh efficiency photovoltaics. We show that the geometry of a multijunction cell greatly affects the optical environment of each subcell and therefore the maximum possible efficiency of the entire ensemble. We show that geometries that allow for spatially independent subcells, such as spectrum-splitting geometries, can yield the highest efficiencies possible. These designs have the best control of radiative emission through enhanced trapping of radiative emission and recovery of some radiatively emitted photons in other subcells. In each of these studies, we enable new and interesting pathways toward achieving significantly higher solar cell efficiencies.

Chapter 2

Enhanced Efficiency of Small ($<$mm^2) GaAs Solar Cells via Passivation with Trioctylphosphine Sulfide

All record efficiency solar cells ($\geq$40%) are composed of GaAs and other III-V compound semiconductors. Currently, GaAs holds the world record for single junction solar cell efficiency of 28.8%, approaching the Shockley-Queisser perfect material limit of 33% [5, 8]. Significant development in the growth of these semiconductors has led to >99% internal radiative efficiency (ratio of radiative recombination to total recombination events), showing an incredible suppression of bulk defects and trap states [11]. Additionally, effective device design through surface passivation of these semiconductors was crucial to achieve high voltages and therefore high efficiency devices. Bare GaAs surfaces are a particularly large source of nonradiative recombination: adsorbed O_2 molecules can displace Ga atoms and induce mid-gap trap states [17]. Passivation is typically achieved through the epitaxial growth of a higher bandgap III-V semiconductor that drives majority carriers away from the minority carrier contacts, preventing recombination before the carriers are collected [18–20]. This passivation only protects the front and rear faces of a cell, leaving the sidewall faces of a cell exposed upon singulation of individual devices. However, this does not negatively affect most large ($\geq$cm^2) sized solar cells whose unpassivated perimeter only accounts for a small fraction (<<1%) of the cell surface area and therefore does not negatively affect the efficiency.

Small III-V solar cells (≤mm^2) have become increasingly attractive. Many of these small, thin-film cells can be wired in parallel, yielding a more durable, flexible network [21]. Additionally, small cells can be used with concentrating optics; a smaller cell reduces the size, and therefore weight and cost, of the optical architecture [22]. We found this size to also be ideal in prototyping spectrum-splitting optics, discussed in Chapters 3 and 4. However, small cells have a much larger perimeter-to-active area ratio, resulting in increased losses due to surface recombination. Therefore, an effective passivation scheme that can be easily applied to sidewalls is desired to enable very high efficiencies of III-V cells for any cell size.

In this chapter, we will discuss our findings on using trioctylphosphine sulfide (TOP:S) as a chemical passivant for small (mm^2), high efficiency GaAs solar cells. We observed passivation through four independent experimental studies. First, surface photoluminescence increased by 50% in response to treatment by TOP:S, and we verified through x-ray photoelectron spectroscopy that 30% of the GaAs surface was bonded to GaAs. Then, TOP:S was applied to thin film GaAs solar cells that ranged in size from 1 cm^2 to 1 mm^2 and we showed a strong increase in the efficiency of small GaAs devices, approaching the efficiency of the larger sized cells. The dark current current-voltage characteristics of these cells were analyzed to show that the increase in cell efficiency of the small devices was due to the reduced recombination current around the perimeter of the device. Finally, we used light beam induced current (LBIC) mapping to show that treatment by TOP:S caused a significant increase in the photocurrent collected near the exposed edge of a device. This increased current corresponds to a surface recombination velocity of 510 cm/s, which should enable the small scale devices desirable for the designs discussed in the following chapters.

2.1 Sulfur-Based Passivation Schemes

Previous literature has shown that sulfur compounds can significantly reduce the density of surface states and increase the photoemission, and therefore quality, of GaAs samples [23–31]. Unfortunately, we have found that the best sulfur treatments, such as small molecules like Na_2S, attack III-V layers and are therefore too reactive to use in an actual GaAs cell. Figure 2.1 shows a scanning electron microscope (SEM) image of a thin film GaAs cell that has been treated with Na_2S. The treatment etched through the topmost exposed semiconductor layer, as shown by the porous semiconductor surface.

The detrimental effects of this treatment were almost immediate and the device was shorted during measurement.

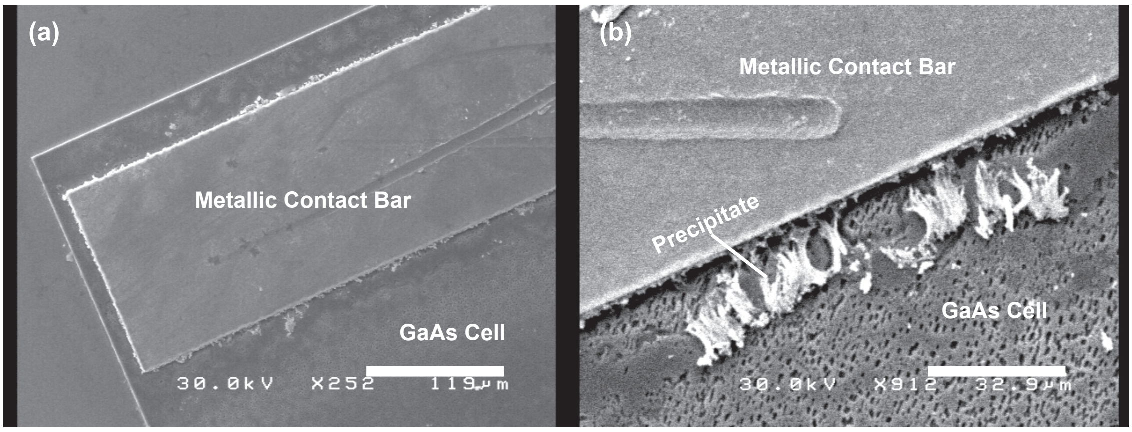

FIGURE 2.1: SEM images of a GaAs solar cell treated with Na_2S. The Na_2S treatment deposits a precipitate around the metallic contact and vigorously etches the top semiconductor layers of the GaAs cell, shown by the porous texture in (b). The scale bars are 199 μm and 32.9 μm for (a) and (b), respectively.

Here, we instead consider trioctylphosphine sulfide ($SP(C_8H_{17})_3$, TOP:S) as an alternative sulfur treatment.[1] A schematic of the compound is shown in Figure 2.2(a) and a schematic of the chemical applied as a sidewall passivant is shown in Figure 2.2(b). Unlike the small molecule treatments, these surfactants contain bulky aliphatic chains that limit surface interaction to a monolayer and therefore should inhibit etching of the surface. Additionally, these molecules are commonly used to passivate colloidal semiconductor nanocrystals, which have a very high surface area to volume ratio [32]. This passivation has yielded extremely high (approaching 100%) photoluminescence quantum yield (PL QY) in such nanocrystals, indicating a quenching of the nonradiative trap states and therefore excellent passivation. In this study, we will treat GaAs wafers and cells to characterize the passivation characteristics of TOP:S.

2.2 Photoluminescence and X-ray Photoelectron Spectroscopy of TOP:S Treated GaAs Wafers

Surface photoluminescence yield is a powerful probe of surface electronic properties. Increased surface passivation will significantly alter the photoemission from a surface

---

[1] TOP:S was synthesized by combining equimolar amounts of sulfur powder (Aldrich, Lot #11325) and Trioctylphosphine (97%, Aldrich, Lot #16496APV) and stirring while applying gentle heat, 50-60°C, for 12-24 hours until the liquid was clear.

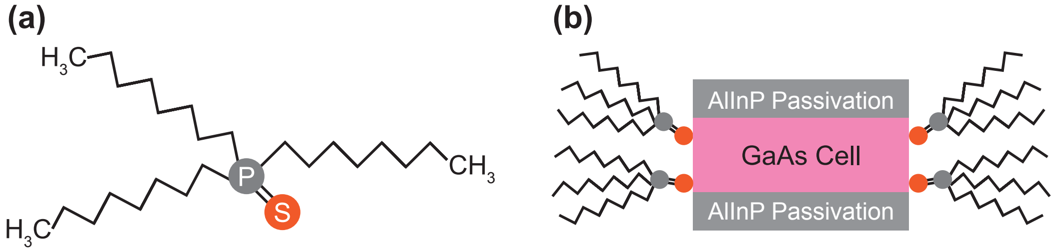

Figure 2.2: (a) Schematic of the trioctylphosphine sulfide (TOP:S) molecule. (b) Schematic of the proposed sidewall passivation on a GaAs cell with front and rear passivation (AlInP). Not to scale.

[33, 34]. (011) facets of undoped GaAs wafers[2] were measured because they correspond to the sidewall facets of cell devices. Measurements were made with 630 nm pulsed diode laser illumination under a 50x objective, and the corresponding photoluminescence spectrum was measured with a CCD coupled with a monochromator.[3] The photoluminescence of an untreated sample is shown in Figure 2.3. The surface photoluminescence is greatly increased after the sample is exposed to TOP:S for 12 hours[4], showing a significant decrease in nonradiative recombination at the surface. The relative enhancement of the integrated photoluminescence is 50%, comparable to some of the previously identified best treatments: Na_2S and N_2H_2 [24, 26, 35]. The secondary peak in the surface photoluminescence near 900 nm corresponds to the lower energy radiative emission from a trap state, such as a vacancy defect or surface bound oxygen [36–38]. We note that after exposure to TOP:S, there was a 10% decrease in the relative emission, indicating a reduction in the defect density through passivation by TOP:S.

A calibration procedure was adapted from Ranganathan and coworkers to convert the observed surface PL signal to an absolute PL quantum efficiency [34]. The raw photoluminescence signal was weighted by the light collected by the objective using a lambertian standard, accounting for the fact that not all of the isotropic emission from the sample would be collected by the aperture of the microscope. This weighted surface photoluminescence signal was then divided by the raw signal of the incident laser light subtracted by the reflection off of the sample. This prevents any antireflection properties the treatment may have from artificially increasing the PL yield. The absolute PL quantum

---

[2] (011) facets were exposed by cleaving GaAs wafers from Freiberger Compound Materials, 4×10^8 Ω cm in the inert (N_2) atmosphere of a glovebox.

[3] The surface PL QE was measured using a Zeiss Axio Observer inverted microscope equipped with a 50x objective and excitation from a 630 nm pulsed diode laser. PL emission was analyzed with a Roper Scientific CCD (Model 7346-0001) passed through a Princeton Instruments Acton SP2150 monochromator.

[4] The sample was soaked in TOP:S for 12 hours in a glovebox and rinsed in toluene to remove the excess TOP:S immediately before the measurement.

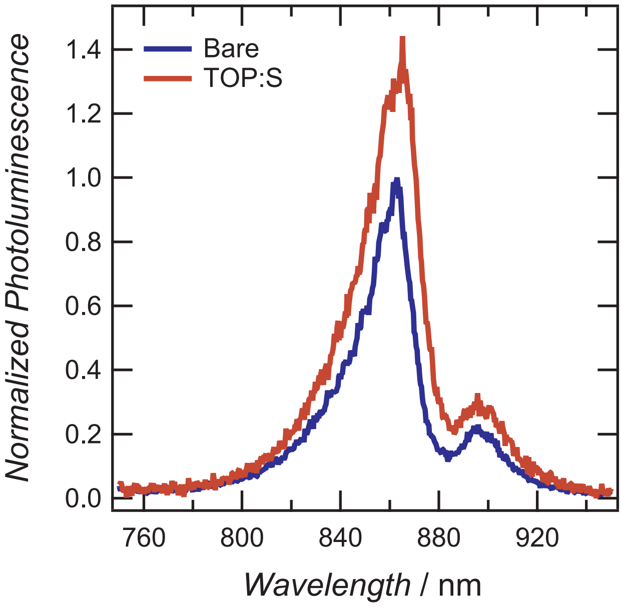

Figure 2.3: Surface photoluminescence of an undoped GaAs (011) facet (blue) shows large enhancement when treated with TOP:S (red), indicating improved surface passivation. The photoluminescence quantum yield of the control versus the treated sample are $0.8 \times 10^{-3}\%$ and $1.2 \times 10^{-3}\%$, respectively.

efficiencies were $0.8 \times 10^{-3}\%$ and $1.2 \times 10^{-3}\%$ before and after treatment, respectively [34]. The low absolute efficiency resulted from the very low carrier concentration of the intrinsically doped GaAs wafer used in the study [39]. However, a significant PL quantum efficiency increase was still observed by using TOP:S.

X-ray photoelectron spectroscopy of similarly prepared samples was performed to determine the coverage of TOP:S on the GaAs surface.[5] Figure 2.4 shows the high resolution XPS scans of the (a) Ga 2P3/2 peak and the (b) As 3d peak and their corresponding fits before and after treatment with TOP:S. The Ga 2P3/2 signal centered at 1117.5 eV is characteristic of bulk GaAs. The treated sample exhibits an additional peak at 1119.0 eV, indicating 48.5% of the surface Ga is bonded to S. There is also a small peak after treatment in the As 3d peak (44.5 eV) that corresponds to 12.3% of the As atoms binding to sulfur. This indicates that TOP:S provided approximately 30% of a monolayer surface coverage, primarily through bonding to surface gallium sites. This observation is consistent with previous reports of GaAs surface chemistry [24, 26].

---

[5] XPS data was captured using the Surface Science Instruments M-Probe system in the Beckman Institute with a monochromatic x-ray source (1486.6 eV Al Kα line), controlled by ESCA25 Capture software. The pressure was maintained below 5×10^{-9} Torr, and peaks were fitted using the ESCA25 Analysis Application (V5.01.04).

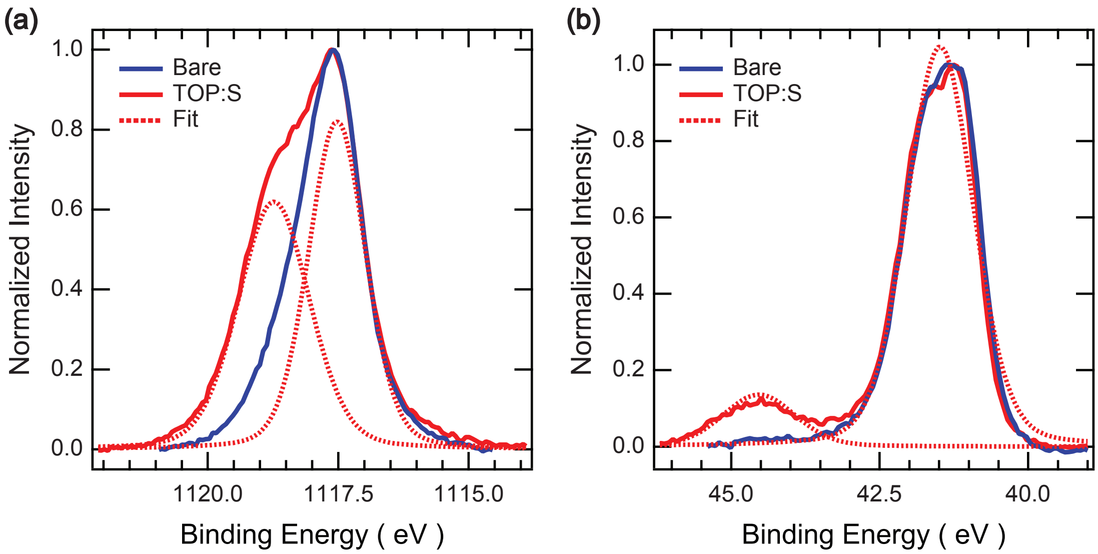

FIGURE 2.4: High resolution X-ray photoelectron spectrographs (XPS) of an undoped GaAs (011) facet cleaved under N2 (blue) and after treatment with TOP:S (solid red) with fits (dotted red). (a) The Ga 2P 3/2 signal centered at 1117.5 eV is characteristic of bulk GaAs. The treated sample exhibits an additional peak at 1119.0 eV, indicating 48.5% of the surface Ga is bonded to S. (b) Comparison of the As 3d signals shows 12.3% of the surface As species was also affected by treatment.

2.3 Light and Dark I-V Characteristics of TOP:S Treated GaAs Solar Cells

Because surface chemistry and bonding kinetics are strongly affected by doping type and concentration, we sought conclusive evidence that passivation with TOP:S could provide efficiency gains in fabricated GaAs solar cells. Thin film GaAs cells without antireflection coatings were provided by Alta Devices. Each sample contained mesa-etched cells with active area sizes of 1 cm^2, 2 mm^2, and 1 mm^2 that were fabricated identically. Treated cells were submerged in pure TOP:S for 12 hours in a glovebox and measured under solution. The light and dark current-voltage response of the cells was measured under 100 mW cm^{-2} of simulated AM1.5G illumination using a Keithley 238 high current source measure unit. Here we discuss the light and dark current-voltage (I-V) characteristics of the cells before and after treatment and show how surface passivation can reduce the nonradiative recombination at the perimeter and increase the efficiency of small (mm^2) devices.

2.3.1 Improved Efficiency of Small GaAs Cells with TOP:S

The effect of sidewall recombination on unpassivated, small (mm^2) GaAs solar cells is shown in Figure 2.5 by the blue markers. There is a large size-dependent trend in efficiency for untreated devices because a smaller cell will more strongly experience the detrimental recombination at the sidewalls. There is a 5% absolute reduction in efficiency for shrinking the active area of the cell from 1 cm^2 to 1 mm^2 for unpassivated devices. A similar trend indicative of sidewall recombination was observed for the short-circuit current density (J_{SC}) and the open-circuit voltage (V_{OC}), (Table 2.1).

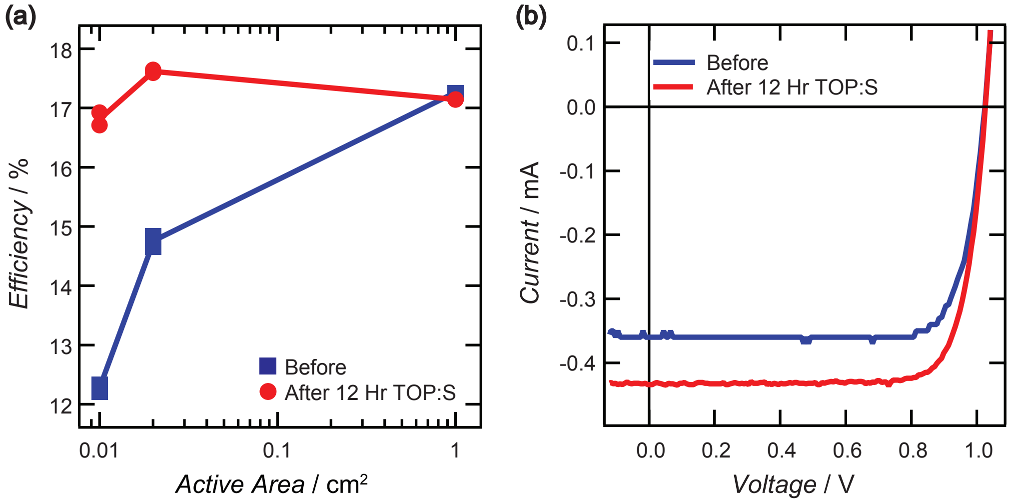

FIGURE 2.5: Size-dependent response of GaAs devices under illumination before (blue) and after (red) treatment with TOP:S. (a) Size-dependent trend in efficiency. The solid lines are a guide for the eye. (b) Representative current-voltage response of a 0.02 cm^2 device.

The light I-V response of the cells after submersion in TOP:S for 12 hours is shown in red in Figure 2.5 and in Table 2.1. Treatment by TOP:S has almost eliminated the size-dependent trend on efficiency, as shown by the strong increases in efficiency for the 1 mm^2 and 2 mm^2 cells. The TOP:S treatment did not increase the efficiency of each cell size by the same amount, which is strong evidence that this improvement is due to decreased sidewall recombination and is not due to an optical effect. As shown in Table 2.1, the TOP:S treatment primarily increased the J_{SC} and provided a small but measurable increase of the V_{OC}. Because the samples were measured while submerged in TOP:S (approximately 1 mm), some of this increase in J_{SC} is due to antireflection. The refractive index of TOP:S (n = 1.47) is between that of GaAs (n = 3.6) and air (n = 1). The magnitude of the antireflective effect expected for a GaAs cell immersed in TOP:S is consistent with the increase in J_{SC} we observed for the 1 cm^2 cell [40, 41]. The

Table 2.1: Average parameters from size series of GaAs solar cells under AM1.5G illumination before and after treatment with TOP:S.

	Efficiency (%)		J_{SC} (mA cm^{-2})		V_{OC} (mV)		Fill Factor (%)	
Cell Size (cm^2)	Before	After	Before	After	Before	After	Before	After
1	17.25	17.2	19.09	20.82	1085.2	1082.8	83.27	74
0.02	14.8	17.82	17.9	21.88	1021.8	1026	81	79.4
0.01	12.3	16.82	14.3	20.52	1007	1013	85	80.9

increase of J_{SC} due to an AR coating will affect equally any size solar cell. Therefore the larger increases in J_{SC} for the smaller cells are due to reducing the recombination current, which we corroborate in the next study.

2.3.2 Reduced Dark Current from TOP:S Observed From Dark I-V Measurements

We then studied the dark I-V characteristics of the cell. It is important to note that the antireflection properties of TOP:S do not affect the measurements here and so any improvement must come from electronic interactions at the surface. Under no illumination, the I-V response of high quality GaAs cells can be described by a conventional double diode model as illustrated in Figure 2.6. The cell current density, J, is approximated by the two diodes in parallel according to

$$J = J_{o1}\left(e^{\frac{qV}{kT}} - 1\right) + J_{o2}\left(e^{\frac{qV}{n_2 kT}} - 1\right) \tag{2.1}$$

where J_{o1} corresponds to the “high voltage” saturation current density, J_{o2} corresponds to the “low voltage” saturation current density, n_2 is a quality factor, V is the operation voltage, q is the charge of an electron, k is Boltzmann’s constant, and T is the operation temperature (assumed 300K). J_{o1} corresponds to the dark current of the device near the V_{OC} of the irradiated cell; J_{o2} describes the dark current response for lower applied biases. The data is valid when the fitted quality factor, n_2, is equal to 2 [42, 43]. Figure 2.6 shows the least squares fit of this double diode model to a 1 cm^2 device after treatment with TOP:S. The model fits the data well across five orders of magnitude of current; the slight deviation at higher applied voltages is indicative of some parasitic series resistance. For this device, the fit to Equation 2.1 gives $n_2 = 2.01$, $J_{o1} = 9\times10^{-21}$ A cm^{-2}, and $J_{o2} = 1\times10^{-11}$ A cm^{-2} which is within the expected parameters for a high quality GaAs cell [14].

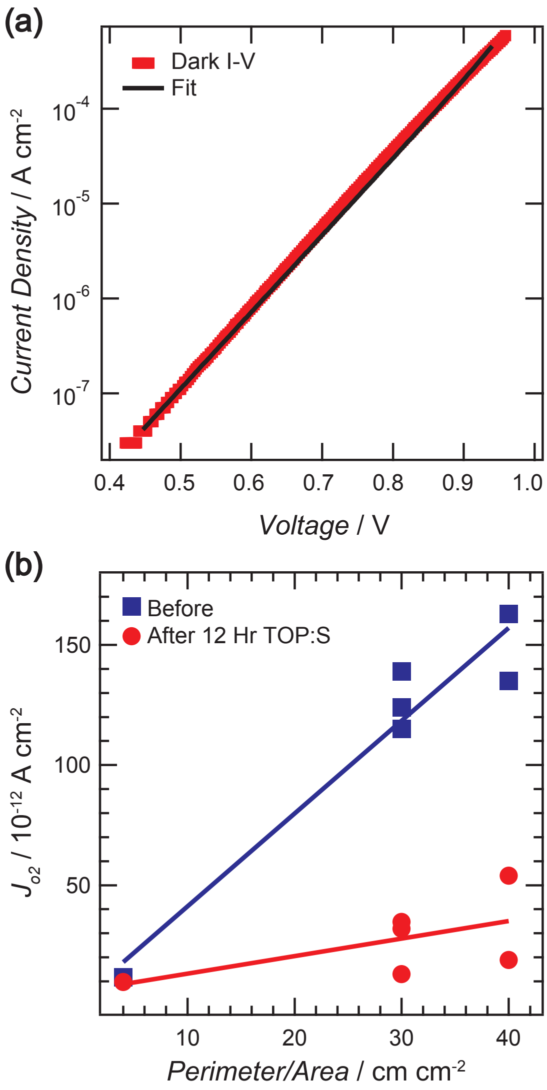

Figure 2.6: (a) The dark current response of a 1 cm^2 device after treatment with TOP:S (red) corresponds well with a double exponential model (black) of Equation 2.1. The fit gives $n_2 = 2.01$, $J_{o1} = 9 \times 10^{-21}$ A cm^{-2}, and $J_{o2} = 1 \times 10^{-11}$ A cm^{-2}. (b) The extracted J_{o2} components across devices before (blue squares) and after treatment with TOP:S (red circles) are plotted versus the sidewall perimeter-to-active area ratio. The fits to Equation 2.3 (solid lines) indicate an 80% decrease in the surface recombination current at the junction perimeter after treatment.

The "high voltage" J_{o1} saturation current density is well correlated to the recombination of minority carriers near the depletion region [42]. A GaAs cell made with high internal radiative efficiency, denoting minimal recombination sites in the bulk, reduces this current and increases the V_{OC} through the following imperical relation:

$$V_{OC} \approx \frac{kT}{q} \ln\left(\frac{J_{SC}}{J_{o1}}\right) \tag{2.2}$$

For each cell size, we fit very low values of J_{o1}, showing the high quality of the bulk GaAs in the device. These fits corroborate well to similarly fabricated devices [14]. We also observed no significant change in the fitted J_{o1} values as a function of cell area, either before or after the TOP:S surface treatment. Because this parameter describes recombination in the bulk material, we do not expect any change in J_{o1} with different cell areas or with the inclusion of a surface treatment. We also note that the increase in V_{OC} we measured after treatment with TOP:S (Table 2.1) is due to an increase in J_{SC} rather than a decrease in J_{o1} (Equation 2.2).

However, the "low voltage" J_{o2} saturation current density can be correlated to the recombination at the perimeter of the device [42, 43]. Decomposition of the "low voltage" saturation current, I_{o2}, gives the following:

$$I_{o2} = J_{o2B}A + J_{o2P}P \text{ where } J_{o2} = {}^{I_{o2}}/_{A} \tag{2.3}$$

Here, A is the active area and P is the perimeter of the cell. The J_{o2B} (A cm^{-2}) saturation current corresponds to recombination in the bulk space charge region of the cell, while the J_{o2P} (A cm^{-1}) saturation current describes recombination within the space charge region exposed to the sidewall of the device. Therefore, a plot of the fitted J_{o2} terms extracted from Equation 2.1 versus the perimeter-to-active area ratio (P/A) for a size-series of devices will yield the J_{o2P} (slope) and J_{o2B} (y-intercept) for the devices before and after treatment. This is shown in Figure 2.6(b). As expected, there is a strong size trend for J_{o2} before treatment due to the increased perimeter recombination for small (P/A $\geq$30) cells [43, 44]. Before treatment, the "low voltage" saturation current was dominated by the perimeter recombination current (3.5×10^{-12} A cm^{-1}) with minimal contribution from the bulk recombination (2.6×10^{-12} A cm^{-2}). However, the perimeter recombination was greatly reduced after treatment by TOP:S (red trace, Figure 2.6(b)) owing to the reduction of recombination at the perimeter of the device. After 12 hours in TOP:S, we observed an 80% decrease of the perimeter recombination current, fitting $J_{o2P} = 0.7 \times 10^{-12}$ A cm^{-1}.

Additionally, the J_{o2P} perimeter current density can be expressed as

$$J_{o2P} = qn_i \Big(S_{SCR} L_s \Big) \tag{2.4}$$

where q is electronic charge, n_i is the temperature-dependent intrinsic carrier density, S_{SCR} is the surface recombination velocity, and L_s is the surface diffusion length along the outside perimeter of the space charge region [42, 43, 45]. Therefore, this indicates that TOP:S lowered the $S_{SCR}L_s$ product of the sidewalls by 80%. Because this measurement was performed in the absence of any illumination, it is clear that treatment by TOP:S decreased carrier recombination at the sidewalls and therefore improved the performance of the solar cells. We then confirmed this by studying extracting the surface recombination velocity through the LBIC study described in the next section.

2.4 Light Beam Induced Current Measurements of Fractured GaAs Solar Cells

The final study used light beam induced current (LBIC) measurements to directly extract the surface recombination velocity of the TOP:S treatment. To create a clean edge, an untreated cell was cleaved by bending it over the edge of a glass slide until a crack parallel to the sidewall facet transected the entire cell. The edge of the cell defined via mesa etching was unsuitable to use because the etching rate of each cell layer was not uniform and therefore the edge could not be easily determined. Using a confocal microscope[6], a 488 nm laser scanned the surface of the device near the crack while a homebuilt transimpedance amplifier detected the photocurrent at each position. Figure 2.7 shows an example LBIC scan with the reflection image (gray scale) overlayed with the LBIC signal. The green color denotes where the sample is generating current.

Four averaged line scans near the edge were compared to four averaged line scans of the same sample after treatment by TOP:S. Here, the solar cell was soaked in TOP:S for 12 hours and subsequently rinsed with toluene to remove all but several monolayers of TOP:S to avoid the anti-reflective effects. The line scans are displayed in Figure

---

[6] Zeiss SM 710. The measurement was performed at 20x to achieve the resolution necessary (step size $\sim$ 200 nm)

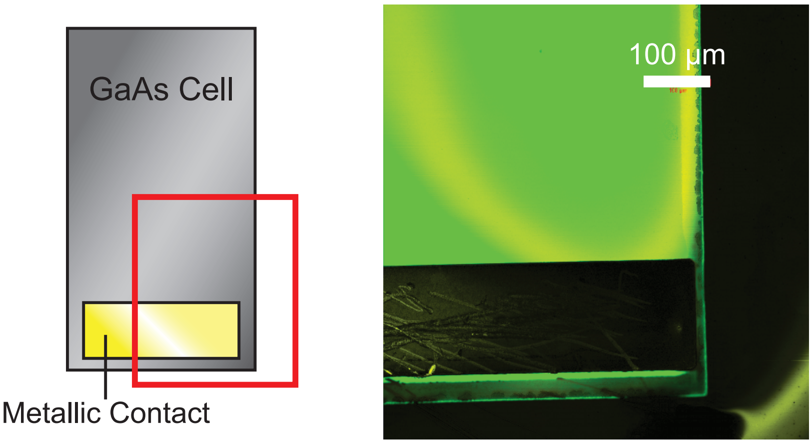

FIGURE 2.7: Example LBIC scan (20x magnification) of a GaAs cell with the reflection image (gray scale) overlayed with the LBIC signal (green scale). The LBIC signal (green) is uniform over the entire bulk of the cell and decreases near the edges of the device. Some difference in reflection (gray scale) results from curvature of the thin film device.

2.8. These data were normalized so that the span of photocurrent corresponds to the signal from the bulk of the device up to the fracture edge. We consistently measured a significant increase in collected photocurrent near the crack after the TOP:S treatment, showing that TOP:S reduced carrier recombination at the fracture edge. We can quantify the surface recombination velocity before and after treatment through the following model.

2.4.1 Derivation of the LBIC Photocurrent Model

Based on models for recombination at silicon grain boundaries, a simplified expression was developed to quantitatively extract the change in surface recombination velocity from the LBIC measurements [46–48]. The derivation of this model closely follows Sze's approach to solving the carrier density profile by the continuity equation [49]. The model is based on the minority carrier excitation in the presence of a generation source (x=0) which is some distance, d, from the edge, as shown by the schematic in Figure 2.9.

Here, $c'(x)$ represents the minority carrier density profile, D represents the diffusivity of the minority carriers in the cell absorbing layer, τ represents the lifetime of the excited minority carriers, and S_{SCR} represents the surface recombination velocity at the exposed sidewall edge. The continuity equation is simplified by the following assumptions:

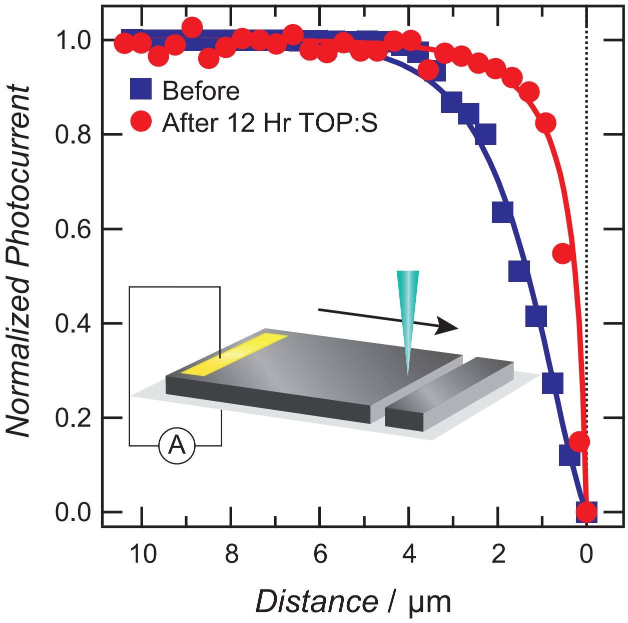

FIGURE 2.8: Light beam induced current (LBIC) profile approaching an induced fracture before (blue squares) and after treatment with TOP:S (red circles). The fits to Equation 2.14 (solid lines) indicate that the increase in collected photocurrent near the fracture results from a decrease in the surface recombination velocity by 94% from 8500 cm s^{-1} to 510 cm s^{-1} after treatment with TOP:S. (inset) schematic of experimental setup.

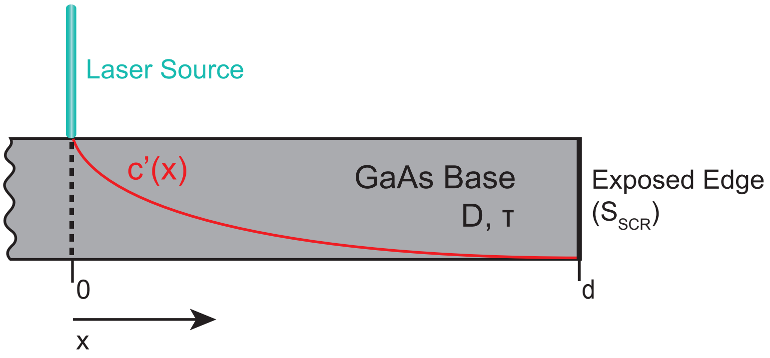

FIGURE 2.9: Schematic of the simplified GaAs cell for the LBIC photocurrent model. Minority carriers are excited by a laser source (x=0) and recombine at a rate dictated by the surface recombination velocity, S_{SCR}, of the exposed edge (x=d).

- Carriers are only generated in the base (the emitter thickness is much smaller than the base)
- All carriers that travel vertically (perpendicular to x) are collected (base thickness $<$ diffusion length), simplifying to a 1D system
- Low level injection
- Steady-state
- Operation at short-circuit

This reduces the continuity equation to:

$$D\frac{\partial^2 c'}{\partial x^2} = \frac{c'}{\tau} \tag{2.5}$$

Additionally, D and τ can be combined through the definition of the minority diffusion length, $L = \sqrt{D\tau}$

$$\frac{\partial^2 c'}{\partial x^2} = \frac{c'}{L^2} \tag{2.6}$$

The first boundary condition describes the generation of excess minority carriers by the laser, which is assumed to be a delta function that produces some number of carriers, c'_{gen}.

$$c'(x = 0) = c'_{gen} \tag{2.7}$$

The second boundary condition describes the balance of the flux of excess carriers at the edge ($x = d$). The recombination current is equal to the number of carriers at the edge multiplied by charge and the surface recombination velocity at the edge.

$$\left.\frac{\partial c'}{\partial x}\right|_{x=d} = \frac{\tau S_{SCR}}{L^2} c'(x = d) \tag{2.8}$$

The differential equation is solved with the given boundary conditions to yield:

$$c'(x) = \frac{c'_{gen}\Big(L\cosh\left(\frac{d-x}{L}\right) + S_{SCR}\tau\sinh\left(\frac{d-x}{L}\right)\Big)}{L\cosh\left(\frac{d}{L}\right) + S_{SCR}\tau\sinh\left(\frac{d}{L}\right)} \tag{2.9}$$

We then solve for the diffusion current.

$$J = -qD\frac{\partial c'}{\partial x} \tag{2.10}$$

Since we are assuming a near perfect sample, the photocurrent observed by LBIC measurements will simply be the difference of the recombination current (J_{rec}) at the edge from the total possible current generated by the laser spot (J_{laser}). We normalize by the current generated by the laser spot ($\bar{J}_{photo} = J_{photo}/J_{laser}$).

$$\bar{J}_{photo} = 1 - \frac{J_{rec}}{J_{laser}} \tag{2.11}$$

where J_{rec} and J_{laser} are given by the following:

$$J_{rec} = -qD\frac{\partial c'}{\partial x}\Big|_{x=d} = \frac{qDc'_{gen}S_{SCR}\tau}{L\Big(L\cosh\left(\frac{d}{L}\right) + S_{SCR}\tau\sinh\left(\frac{d}{L}\right)\Big)} \tag{2.12}$$

$$J_{laser} = -qD\frac{\partial c'}{\partial x}\Big|_{x=0} = \frac{qDc'_{gen}\Big(S_{SCR}\tau\cosh\left(\frac{d}{L}\right) + L\sinh\left(\frac{d}{L}\right)\Big)}{L\Big(L\cosh\left(\frac{d}{L}\right) + S_{SCR}\tau\sinh\left(\frac{d}{L}\right)\Big)} \tag{2.13}$$

This yields the final equation:

$$\bar{J}_{photo} = 1 - \left(1 - \frac{S_{SCR}\ \tau}{S_{SCR}\ \tau\cosh\left(\frac{d}{L}\right) + L\sinh\left(\frac{d}{L}\right)}\right) \tag{2.14}$$

The normalized photocurrent for this system is plotted for different values of surface recombination velocity, S_{SCR}, as a function of distance, d, from the edge of the sample in Figure 2.10. Higher surface recombination velocities correspond to a higher rate of recombination at the surface, and therefore the current is reduced approaching this surface. Additionally, the current decrease from carrier recombination penetrates further into the sample for high values of S_{SCR}, which will more strongly affect small cells.

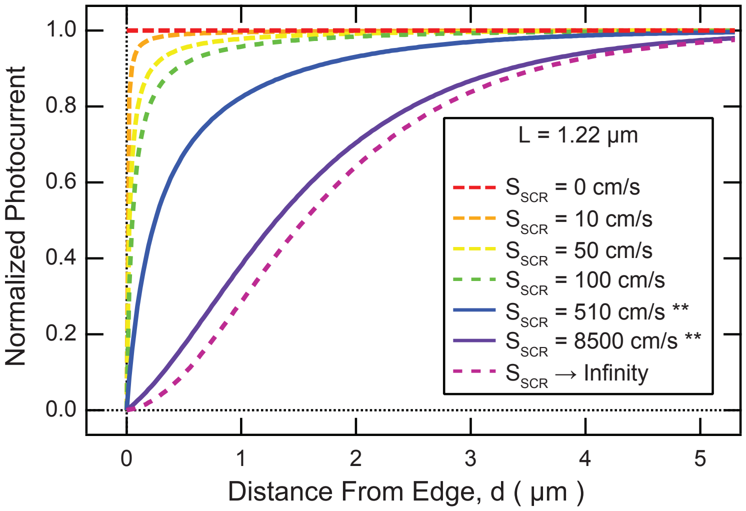

FIGURE 2.10: Modeled light beam induced current (LBIC) profiles approaching an exposed edge. The dotted lines show profiles for some example surface recombination velocities, and the solid lines show the profiles for the surface recombination velocities obtained from the data in the following section.

2.4.2 Analysis of the LBIC Photocurrent Data

Using the simple model derived, we can fit the surface recombination velocities and diffusion length for the sample before and after treatment. We determined that the diffusion length, L, of the minority carrier devices was 1.22 μm. This number is slightly lower than expected for cells of similar quality, but we note that local environment can significantly affect the lifetime and therefore we believe that we reduced the local lifetime by inducing the fracture [50].

We determined the surface recombination velocities to be 8500 cm s^{-1} before treatment, a typical value for a bare or oxidized GaAs surface, and 510 cm s^{-1} after treatment with TOP:S. This represents a 94% decrease in surface recombination velocity, which matches well to the predicted decrease from the dark current study. We also note that the surface recombination velocity of the TOP:S treated surface is comparable to the surface recombination velocity of some epitaxially grown III-V layers, which is impressive for a simple chemical treatment. Once again, we have shown strong evidence that TOP:S improved the solar cell performance by passivating the edges of the device.

2.5 Conclusion and Outlook

Our results show that TOP:S can improve the device performance of small (mm^2) GaAs solar cells by reducing the carrier recombination of exposed sidewall facets. We believe that these results are extremely exciting for enabling high efficiency devices where small cells can reduce the overall footprint and cost module. In the next two chapters, we will discuss a solar cell module design where small cells are attractive in designing and prototyping an ultrahigh-efficiency, spectrum-splitting structure. Additionally, this passivation study could theoretically be extended to self-healing structures. One could imagine an architecture where this passivation liquid is released upon response to cell damage in order to mitigate carrier recombination losses induced from the fracturing sites.

We note that further development of this class of surfactants could lead to even better passivation of III-V semiconductor solar cells. The lengths of the aliphatic chains could be studied to determine if there is an optimal value that maximizes surface coverage while preventing further oxidation of the surface. Additionally, the functional group could be altered — previous literature has indicated that other chalcogenides, such as Se and Te, can passivate GaAs surfaces even better than S [51].

Chapter 3

Design of Spectrum-Splitting Optics for Ultrahigh Efficiency Multijunction Cells (>50%)

The clearest route to ultrahigh (>50%) solar cell efficiencies is through multijunction cells that divide the incident spectrum into different frequency bands for conversion by subcells best tuned to those bands. These cells are capable of efficiencies far exceeding 50% because the thermalization of carriers and lack of absorption of low energy photons are the largest mechanisms in the detailed balance limit of solar conversion [52–54]. However, the best fabricated multijunction cell has only achieved a maximum of 46.0% efficiency, limited in materials combinations and therefore limited in number of bandgaps. Further, once these cells are integrated into a field-ready module with concentrating optics and an electronic power conditioning system, this efficiency drops to a maximum of 38.9% [8]. An example of such a structure, a *tandem* device, is shown in Figure 3.1. In a tandem multijunction cell, each subcell is grown epitaxially on top of one another, which allows for division of the incident spectrum through sequential absorption through each subcell layer. While this is an elegant solution for dividing the incident spectrum, the layers are required to be almost perfectly lattice-matched to one another to prevent defect incorporation during growth, limiting materials choices. Additionally, the subcells are now electronically in-series, which limits the maximum efficiency and severely limits the maximum annual energy production [4].

Because of the constraints of a traditional multijunction geometry, our efforts have focused on *spectrum-splitting* geometries that avoid the constraints of traditional tandem

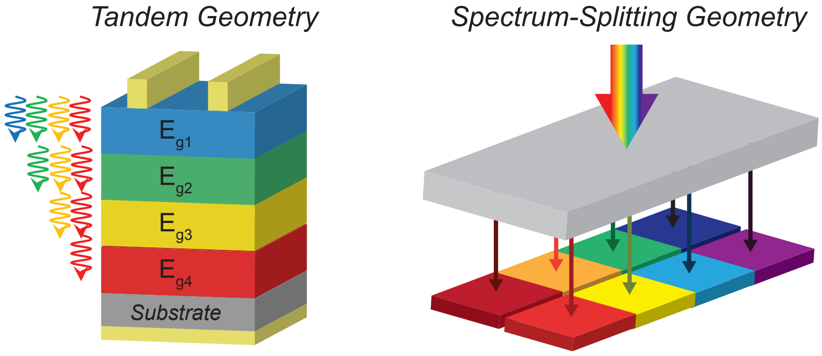

FIGURE 3.1: Schematics of a tandem and a spectrum-splitting multijunction geometry. Spectrum-splitting geometry adapted from [9].

geometries and therefore should be able to achieve ultrahigh efficiencies. As shown in Figure 3.1, spectrum-splitting architectures employ an external optical element to divide the incident solar spectrum onto lateral subcells [55]. These subcells can be grown with any material without constraints on the electrical architecture, which allows for the inclusion of many more bandgaps and thus very high efficiencies [56–61]. However, these designs often have a higher degree of complexity owing to the design of the external optic, higher number of subcells, and independent electrical architecture. For example, the Very High Efficiency Solar Cell (VHESC) project led by the University of Delaware proposed a 6 junction design with predicted efficiencies exceeding 50% but prototyped a 4 junction cell with the record spectrum-splitting submodule efficiency (4 terminal measurement) of 38.9% [8, 57]. The difference in their predicted cell efficiency and their realized design shows the importance of developing a model that accounts for all losses. Our team has focused on creating a comprehensive systems-level model that incorporates as many realistic losses as possible to determine the true efficiency limits of our design. This chapter will focus on one optical design, the Polyhedral Specular Reflector, and how optimizing the photon distribution and concentration can make ultrahigh efficiencies possible. Additionally, we will discuss the other models (cell and electrical) and how they affect the ultimate module efficiency.

3.1 Potential Spectrum-Splitting Designs and Systems Level Models

As discussed in Chapter 1, photon management is quickly becoming the focus of developing solar cell efficiencies because cell growth and device design are very well understood.

The key to ultrahigh efficiency is optimization of the spectrum-splitting optics — if we cannot achieve good spectrum-splitting then we will not minimize thermalization and lack of absorption losses. At the inception of this project, our team investigated many methods of spectrum-splitting. A few spectrum-splitting optical architectures are shown in Figure 3.2 and include splitting via dispersion (holograms), randomizing optics (light trapping with omnidirectional filters), and sequential filtering.

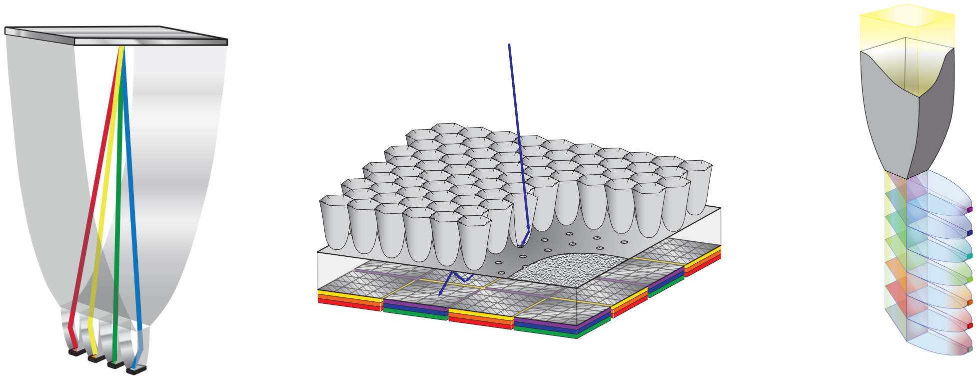

Holographic Spectrum-Splitter

Light Trapping Filtered Concentrator

Polyhedral Specular Reflector

FIGURE 3.2: Schematics of spectrum-splitting photovoltaic modules designed by the Atwater Group. We investigated using a holographic element (Holographic Spectrum-Splitter [61]), randomizing optics (Light Trapping Filtered Concentrator [60]), and sequential reflecting optics (Polyhedral Specular Reflector, this work).

Each of these designs are based on optical elements that can theoretically achieve high performance (i.e., high dispersion, high reflectivity). However, there are many challenges associated with solar conversion: the source is broadband (near UV to infrared), the cells will require some concentration to meet ultrahigh efficiencies which can alter the optical performance, and any photon that is misallocated is a significant loss [62]. Furthermore, cell design must be optimized to best absorb and convert photons from a given frequency band, and a more complex electrical architecture is required to convert the electrical signal from many independent subcells into a standard, two-terminal output. Often these challenges are interrelated, and therefore our team developed a broad systems level model to capture as many realistic effects as possible. Figure 3.3 shows a schematic detailing the systems level model. First, determining the bandgaps of the subcells will determine the materials and corresponding cell performances as well as the spectrum-splitting required from the optical elements. Then, determining the photon allocation through designing an optical architecture with spectrum-splitting and concentration can be used along with cell models to determine the expected conversion efficiency before electrical losses. This process can be iterated for various optical optimizations, and when a suitably high efficiency design is available, an electrical efficiency can be determined for the structure that determines the contact geometry for the subcells, interconnection losses, and DC-to-DC conversion circuit efficiency for a two-terminal output.

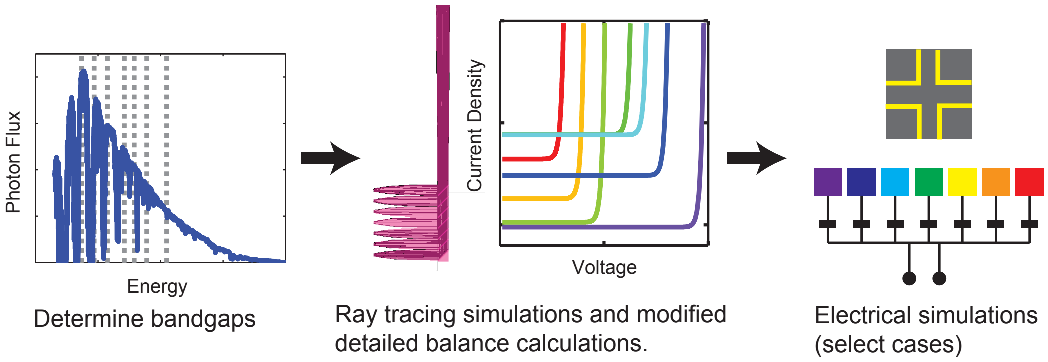

FIGURE 3.3: Schematic showing the systems level modeling for determining module efficiency of a spectrum-splitting module.

This effort was first spearheaded by Dr. Emily Warmann, who determined the broad qualities needed for ultrahigh spectrum-splitting photovoltaics. She optimized the ideal bandgaps using modified detailed balance calculations under systems with different cell, optical, and electrical qualities to determine a realistic set of parameters for ultrahigh efficiency [4]. She showed that a structure with seven subcells made from high quality materials (comparable to III-V single junction subcells), high concentration (100-500x), high spectrum-splitting efficiency (90% of photons per band are correctly allocated), and an efficient external electrical circuit (95%) could achieve record, ultrahigh efficiency module devices [4]. The inclusion of the spectrum-splitting optics and the high number of subcells represent a large departure from the current multijunction cell state-of-the-art. This model was then refined for each optical design to determine the specifications for a realistic module. This chapter details the comprehensive modeling of one of these optical designs, the polyhedral specular reflector (PSR), which was the only design of the original three proposed to meet the qualities determined by Dr. Warmann's models and therefore show >50% module efficiencies. We first discuss the design of the structure, using Dr. Warmann's detailed balance optimizations to guide the choices of the subcell materials and spectrum-splitting method. Then we show the optimization of this design through ray tracing simulations of the spectrum-splitting optics integrated with modified detailed balance calculations to account for nonideal device physics of the subcells. The optical geometries were optimized for both ultra-high efficiencies and alternative cost effective designs. Finally, we incorporate additional electrical losses to determine the module efficiencies of a few interesting cases and provide additional commentary about improvements that could be made for lower cost structures.

3.2 Polyhedral Specular Reflector Design

The polyhedral specular reflector is based off a specular reflecting optics geometry where light is sequentially filtered into seven different bands by passing through a series of filters. This can be done using shortpass (shorter wavelengths transmit, longer wavelengths reflect) or longpass filters (longer wavelengths transmit, shorter wavelengths reflect). The type of filter chosen, as shown in Figure 3.4, determines the geometry of the spectrum-splitting. With shortpass filters, the simplest geometry is to arrange the filters in a 45° parallelepiped shape where photons from highest to lowest energy are sequentially transmitted to subcells for conversion. With longpass filters, the simplest geometry is the arrange the filters at 45° in a vertical stack where photons from highest to lowest energy are sequentially reflected to subcells for conversion. Additionally, one needs to consider how to add concentration to a spectrum-splitting scheme and how that will affect the specular, spectrum-splitting path. As we will show in the following discussion, it is more practical to use longpass filters because they have a higher spectrum-splitting efficiency and because the mechanical assembly for adding concentration is greatly simplified.

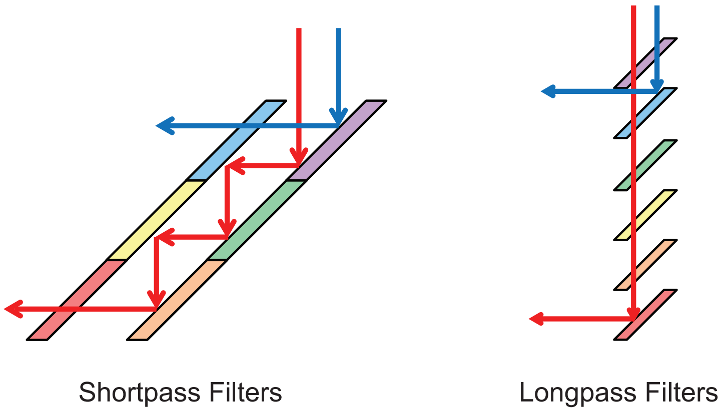

Figure 3.4: Geometries of spectrum-splitting structures using specular reflection off of filters. The light paths of two frequencies are shown. Shortpass filters can be used in a 45° parallelepiped geometry and longpass filters can be used in a vertical stack.

3.2.1 Previous Evolutions of the Polyhedral Specular Reflector Design

The first two years of this project were dedicated solely to design of spectrum-splitting optical elements, and during this time, the design evolved iteratively to realistically achieve >50% efficiency. Figure 3.5 shows the evolution of the PSR design, which started with a shortpass filter arrangement with only one stage of concentration and eventually evolved into a longpass filter arrangement with two stages of concentration. Each design step represented a response to some fundamental limit in efficiency, which we discuss here.

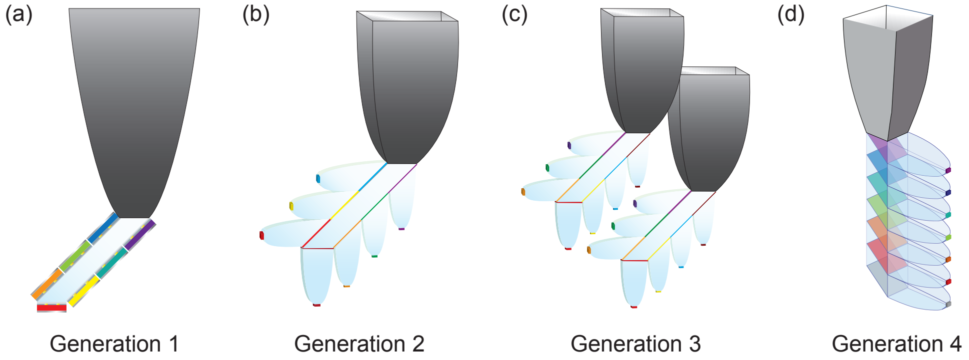

Figure 3.5: Evolution of the polyhedral specular reflector design. Earlier generations used shortpass filters while the final design uses longpass filters, driven by the need for better spectrum-splitting efficiency.

The original design, the PSR Generation 1 (Figure 3.5(a)), was inspired by a patent filed by Edmund Ellion in 1987 [63]. In the patent, subcells are arranged around a 45° parallelepiped and, much like a traditional multijunction cell, the spectrum is split via absorption within the subcells themselves. Lower energy light is specularly reflected off of a subcell's back reflector toward the remaining subcells. While this is elegant in its simplicity, the design was adjusted to meet our stringent requirements for high efficiency. First, shortpass filters were added in front of every subcell. While ideal cells may not absorb any photons below the bandgap of the absorber, realistic subcells have some small parasitic absorption of lower energy photons from highly doped layers and metallic back reflectors [40]. While this number is very small ($\sim 2\%$) for high quality cells, it is a significant parasitic loss for seven subcells, preventing >50% efficiency [64]. Additionally, a hollow, mirrored primary concentrator was added to the front aperture of the prism to increase the concentration necessary for high efficiency. However, concentration increases the angular spread entering the 45° parallelepiped, reducing the efficiency by (1) disrupting the designed specular reflecting path and (2) reducing the splitting efficiency of the filters, which are sensitive to incident angle. The parallelepiped was reimagined as a solid, higher index material that could reduce the angular spread through refraction. However, geometric calculations predicted that a design with even a very high index material (n=3.5) and perfectly omnidirectional filters could not reduce the misallocation enough to achieve 50% efficiency.

The second generation design (Figure 3.5(b)) responded to the challenges of incorporating concentration by dividing the concentration into two stages. Some of the concentration would occur after the spectrum had been split, lessening the angular spread in the parallelepiped and on the filters, allowing for a high overall concentration with better spectrum-splitting. However, it was difficult to design shortpass filters for such a broadband range of wavelengths without misallocating the high energy photons from secondary harmonic reflections. Therefore this misallocation of photons again prevented this design from achieving ultrahigh efficiencies.

The third generation design (Figure 3.5(c)) both improved the quality of the filters and reduced the angular spread of the primary concentrator. First, the filter order was rearranged such that a longpass filter for the lowest bandgap subcell was placed first, thereby removing the longest wavelength light from the spectrum first. This made the design of the remaining shortpass filters significantly easier, which had a narrower band to reflect over and fewer secondary harmonics within the bands of interest. Then, vertical packing was introduced as a way to minimize the concentration, and therefore the angular spread in the prism and on the filters. If individual PSR units could vertically pack instead of occupying the same horizontal plane, then there is no minimum required primary concentration and the angular spread can be greatly reduced. While this design was very close to achieving ultrahigh efficiencies, ultimately the shortpass filters were not reflective enough, misallocating some of the lower energy photons in subcells that could not convert them and reducing the maximum efficiency possible.

Finally, the fourth and final generation design (Figure 3.5(d)) keeps the two concentration stages and the vertical packing from the previous generations, but instead uses a longpass filter structure. The filters are imbedded in a solid optic to reduce the angular spread from the first concentration stage and make it is easier to achieve good transmission rather than good reflection. Therefore longpass filters are the most efficient at dividing the incident solar spectrum because the number of low energy photons misallocated to a high bandgap subcell is significantly reduced. The longpass transparencies that can be achieved in this environment (>99%) are capable of a 50% efficiency spectrum-splitting module. Additionally, this design greatly simplifies the fabrication by having all of the secondary concentrators and cells on one side.

3.2.2 Final Polyhedral Specular Reflector Design

Figure 3.6(a) shows a detailed schematic of the final PSR design. Incident light enters the primary concentrator, a hollow, mirrored compound parabolic concentrator (CPC). The output of the primary concentrator feeds directly into a solid glass prism with seven longpass filters. The filters are oriented at 45° and ordered to sequentially reflect away the highest energy photons. As a result, the incident spectrum is divided into seven bands with the highest energy photons at the top and the lowest energy photons at the bottom of the prism. Each band is then further concentrated by a solid glass secondary CPC before it is converted by one of the seven subcells. Depending on the relative sizes of the primary and secondary concentrators, these individual units can pack horizontally, as in Figure 3.6(b), or vertically, as in Figure 3.6(c) [58, 61]. The optimization of this design will focus on maximizing the correct photon allocation while still maintaining the high (100-500x) overall concentration necessary for ultrahigh efficiency cells.

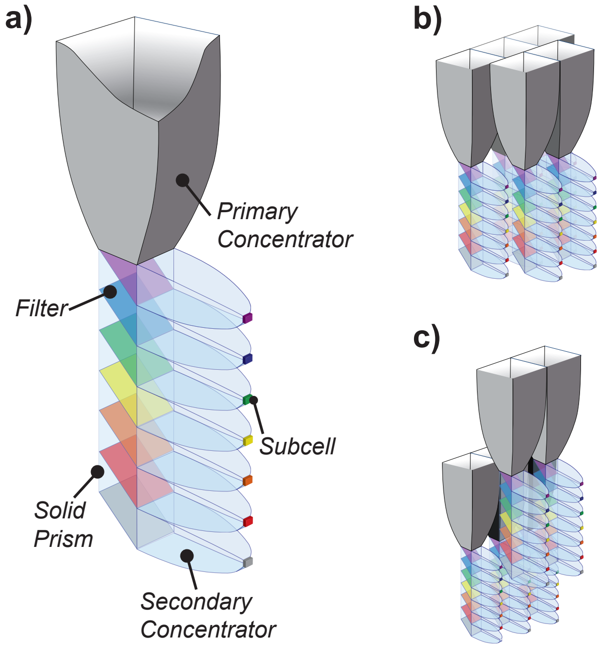

Figure 3.6: (a) Schematic of the polyhedral specular reflector (PSR) submodule. Incident light is divided through reflection and transmission by a series of filters imbedded in a solid glass prism. Concentration is achieved in two stages. (b) Horizontal packing of PSR submodules. (c) Vertical packing of PSR submodules.

Table 3.1: The seven optimized bandgaps for the spectrum-splitting structure with suggested III-V alloys. Modeled EREs assume lattice-matched growth to a common wafer (e.g., GaAs), lifted off subcells, and high quality back reflectors.

E_g (eV)	III-V Alloy	Growth Wafer	External Radiative Efficiency (%)
2.13	$Al_{0.20}Ga_{0.32}In_{0.48}P$	GaAs	0.19%
1.78	$Ga_{0.37}In_{0.63}P$	GaAs	8% [65]
1.58	$Al_{0.10}Ga_{0.90}As$	GaAs	3%
1.42	GaAs	GaAs	22.5% [14]
1.15	$In_{0.87}Ga_{0.13}As_{0.28}P_{0.72}$	InP	1.2%
0.94	$In_{0.71}Ga_{0.29}As_{0.62}P_{0.38}$	GaAs	1.6%
0.74	$In_{0.53}Ga_{0.47}As$	InP	11%

3.2.3 Subcell Design in the PSR

The seven optimized bandgaps from the earlier detailed balance optimization study are shown in Table 3.1 [4, 62]. We then chose corresponding III-V alloys to represent each bandgap because these semiconductors provide many benefits for our design. Devices made from these materials can be epitaxially lifted off from the growth substrate and placed on a high quality back reflector, further increasing the voltage from each subcell [11]. Additionally, all record efficiency solar cells are composed of III-V alloys [8]. We note that the bandgaps are slightly modified from the optimum bandgap combination outlined in [4] such that these III-V alloys that are lattice-matched to InP or GaAs for higher quality growth. This modification had an insignificant effect on the efficiency.

To quickly and accurately estimate subcell performance under different optical structures, we determined the fraction of ideal short circuit current (f_{Jsc}) and the external radiative efficiency (ERE) as inputs to a simple detailed balance calculation. This calculation is significantly faster than modeling the cell characteristics through device physics simulations but can still capture the relevant physics for high efficiency designs [4, 62]. Nonideal current collection and incomplete absorption was accounted for by the fraction of ideal short circuit current. The fraction of ideal J_{sc} was calculated to be 92% using external quantum efficiency (EQE) data from a high efficiency GaAs solar cell and assuming 2.8% contact shadowing, which is typical in high concentration designs [14]. We note that the shadowing losses from the contacts will depend on the concentration and geometry of the design and we adjust for this later when calculating the full module efficiency. Material quality was defined by the external radiative efficiency

(ERE) [10] and was estimated from actual solar cell devices and 1-D device physics simulations [14, 62, 65]. Assuming realistic subcell properties and 300 suns concentration, the efficiency expected from these subcells is 57%. Therefore >50% module efficiency cells should be possible with high quality optics and a high efficiency power conditioning system.

3.2.4 Designing the Spectrum-Splitting Components

Knowing the bandgaps, the filters can be designed to appropriately divide the incident spectrum. As we learned from the evolution of the PSR design, the design of the optical splitting structure is incredibly important because effective division of the solar spectrum is required to prevent the misallocation of photons. We designed seven aperiodic dielectric filters using alternating layers of SiO_2 and TiO_2 that provide a high index contrast and therefore a high reflectivity. These filters function based on the interference of light reflecting through the SiO_2 and TiO_2 layers, similar to a Bragg mirror or an oil slick. The number and thicknesses of these layers were optimized in OpenFilters to maximize reflection of photons with energies above the bandgap of the corresponding subcell and minimize reflection of photons with energies below the bandgap [66]. Typically these filters had a few hundred layers and a total thickness of 20-35 μm (Appendix A). An example filter index profile is shown in Figure 3.7.

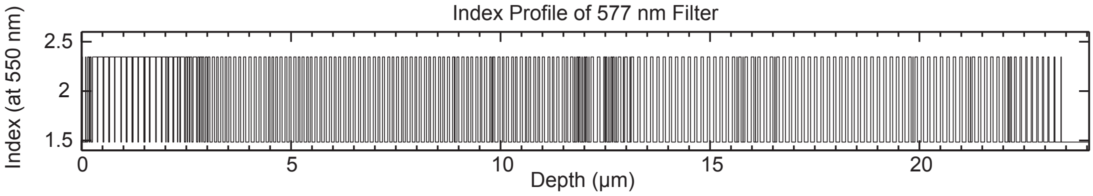

FIGURE 3.7: Refractive index profile (at 500 nm) of a PSR filter. This filter is a 577 nm longpass and comprises of alternating layers of SiO_2 and TiO_2. More filter indices are given in Appendix A.

The simulated spectrum-splitting from the filter reflections at 45° angle of incidence are shown in Figure 3.8. Each filter shows high reflectivity for most photons with energies greater than the corresponding subcell bandgap and almost no reflectivity for lower energy photons. The reflectivity decreases near the bandgap as a result of s- and p-polarization splitting but the cutoff always occurs for an energy higher than the bandgap. This ensures that no low energy photons are misallocated to a subcell that cannot convert it, but some high energy photons will be distributed to lower energy subcells and converted at a lower voltage. The spectrum-splitting achieved from these filters should result in >50% efficiency with some concentration (>100x).

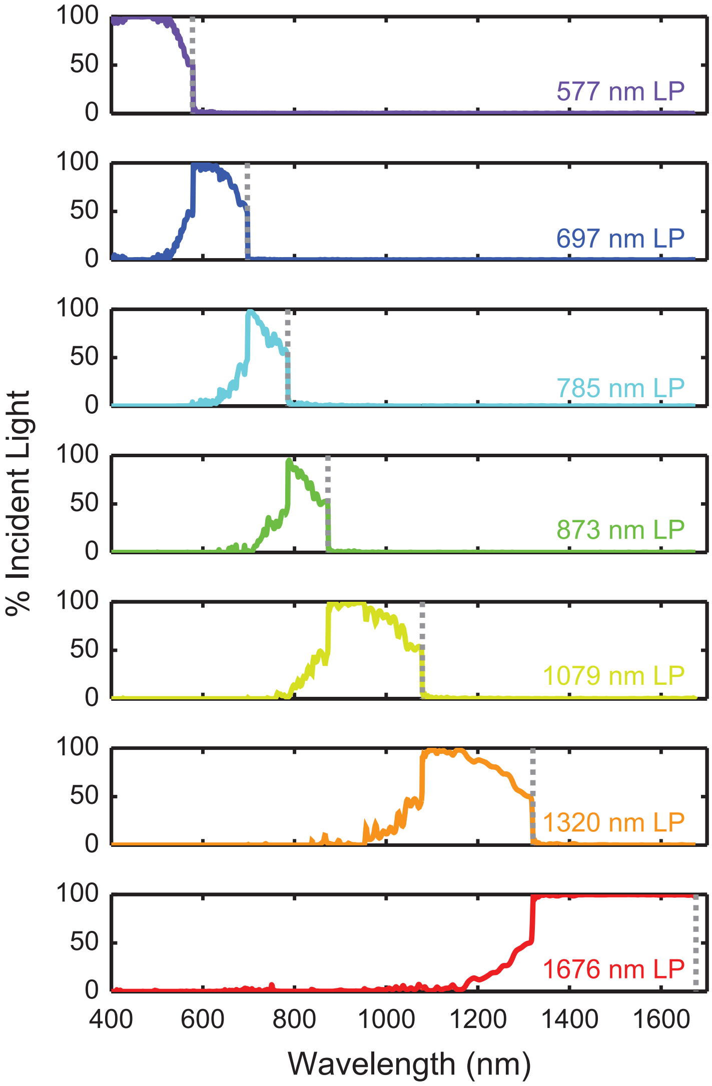

FIGURE 3.8: Spectrum-splitting calculated from the filter reflections for the PSR design. These filters were designed using alternating layers of SiO_2 and TiO_2.

While many options for concentrators exist, we ultimately chose compound parabolic concentrators (CPCs) for both the primary and secondary concentrators in Figure 3.6 [67]. These concentrators are nonimaging concentrators: the total power transfer of light is optimized instead of imaging the source. Further, a CPC is the only optical concentrator that achieves the maximum limit of étendue and therefore the maximum concentration possible for a given acceptance angle. This is particularly attractive for our design because this also provides the smallest angular spread of any comparable concentrator and therefore the highest splitting efficiency. This relationship between acceptance and output angle is the primary design trade-off in this optical spectrum splitting architecture. First, our module must accept all photons from the sun. We defined our acceptance angle of the primary concentrator to be 1.8°. This is larger than the disc of the sun because we wanted to allow for circumsolar radiation and possible tracking error. Second, the output angle of the primary concentrator will affect the spectrum-splitting efficiency. The aperiodic dielectric filters are sensitive to incident angle, and an increase in the primary concentration, which increases the output angle of the primary concentrator, alters the filter properties and decreases the spectrum-splitting efficiency. Finally, the efficiency will decrease if the acceptance angle of the secondary concentrator is smaller than the output angle of the primary concentrator because light will be rejected by the secondary concentrators. The geometries of the primary and secondary concentrators must be optimized together to maximize transfer of incident sunlight to the correct subcells.

3.3 Optimizing the Polyhedral Specular Reflector Geometry

We implemented ray tracing simulations to determine the photon flux to each subcell under different concentration geometries. An example ray tracing model is shown in Figure B.1. The details from the ray tracing simulations (LightTools) and the MATLAB functions that modify and run the simulations are given in Appendix B. We modeled the entire PSR structure, including realistic antireflection coatings, mirror surfaces, and filter properties, under a broadband illumination source with 1.5° divergence to account for circumsolar radiation. One example of these coatings, the air-glass antireflection coating, is shown Figure 3.10. The antireflection coating is composed of MgF_2, SiO_2, and very thin layers of TiO_2 and was optimized to maximize transmission for the wavelengths of interest (300-1700 nm). The mirror coating of the primary concentrator is assumed to be 300 nm of silver coated with 31 nm of SiO_2 to increase the broadband reflectivity and prevent oxidation. We assumed that all solid elements were made from fused silica ($n = 1.46$ at 500 nm). Finally, the cell antireflection coatings were single and dual layer structures of some combination of SiN, TiO_2, and Ta_2O_5 optimized for their designed frequency band. The reflectivities of the remaining coatings are shown in Appendix A. The size of the optical splitting prism was fixed with a 1 cm x 1 cm opening, allowing the primary concentrator input size and secondary concentrator output size to vary. This size was chosen for a future prototyping effort (Chapter 4) but the effects discussed here should scale for a macro-optical sizes ($> 100\mu$m).

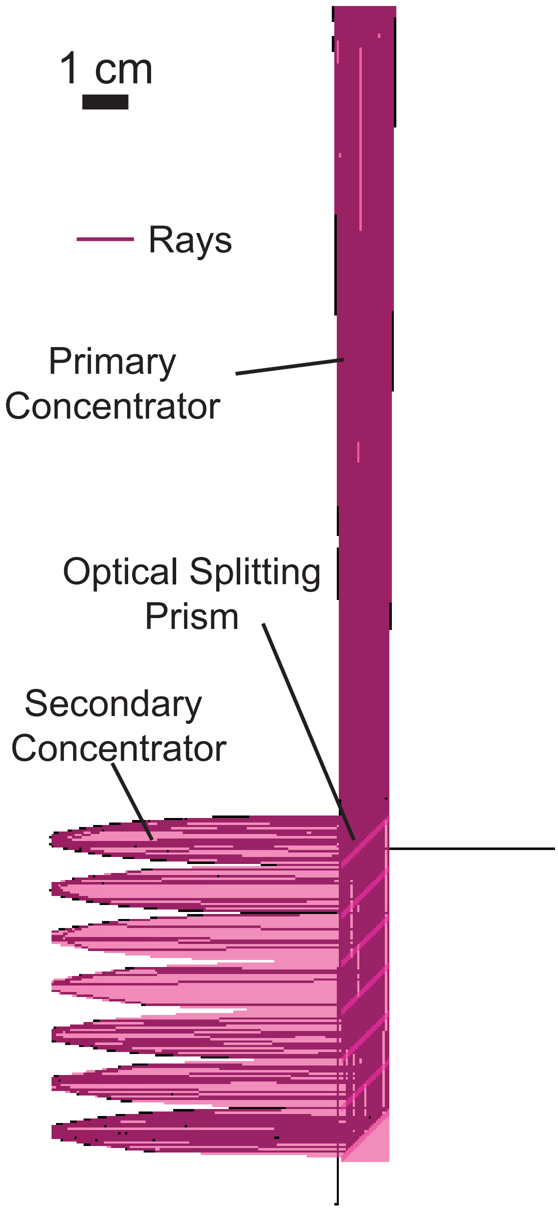

Figure 3.9: Screencapture of a ray tracing simulation. The burgandy lines represent individual rays propagating through the polyhedral specular reflector.

After each simulation, the extracted photon flux to each subcell was input to the modified detailed balance calculations to determine the overall conversion efficiency of each simulated structure. Since optimizing the contact geometry of each design is computationally intensive, we calculated the contactless device efficiency instead of the full module efficiency. The contactless device efficiency includes optical and cell losses but

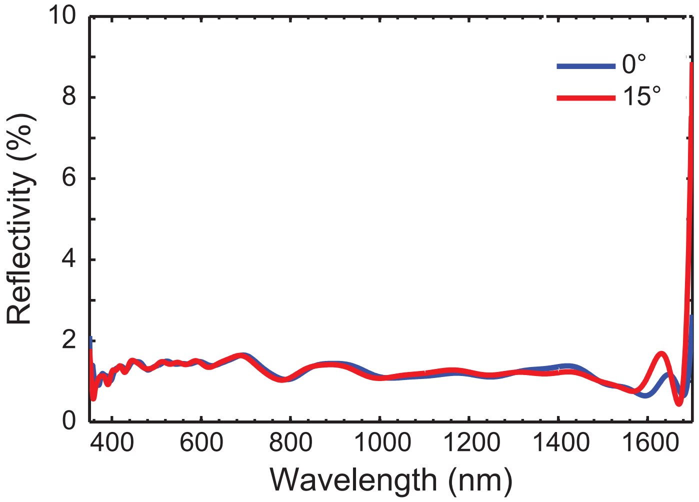

Figure 3.10: Modeled reflectivity of the top air-glass antireflection coating created for the PSR design. There is minimal change in the reflectivity across different angles of incidence.

excludes electrical losses. Losses due to contact resistance, power conditioning, and DC-to-DC conversion will be determined for individual cases of interest in a following section. Based on previous simulations, we expect the efficiency of the electronics to be 95-98%, so contactless device efficiencies exceeding 52% should be able to achieve >50% module efficiencies [68].

3.3.1 Untrimmed Concentrator Geometries

First we considered untrimmed concentrator geometries which will yield the maximum concentration, and therefore the maximum length, for a given combination of CPC input angle and output angle. Figure 3.11 shows the contactless device efficiency of the PSR as a function of secondary concentration (x-axis) and primary concentration (colored series). The output angles in air for each primary concentration are given in the legend for reference. Ultrahigh efficiency (>50%) designs are possible with this architecture, with the highest efficiency designs incorporating low primary concentration and high secondary concentration. A higher primary concentration corresponds to a higher output angle, which increases the angular distribution on the aperiodic dielectric filters and reduces the optical splitting efficiency. A higher secondary concentration does not affect the performance of the filters, so in general, increasing the secondary concentration increases the efficiency. However, there is a critical secondary concentration for each primary concentration series that corresponds to the acceptance angle of the secondary concentrator being too small for the corresponding output angle of the primary concentrator, as shown by the turnover in efficiency for high values of secondary concentration. Therefore it is intuitive that a lower primary concentration and higher secondary concentration would lead to the highest contactless device efficiencies. It is also important to note that designs with higher primary concentration (>36x) are capable of record module efficiency designs (>40%), which are attractive as possible lower cost alternatives that reduce the amount of filters and secondary optics per module.

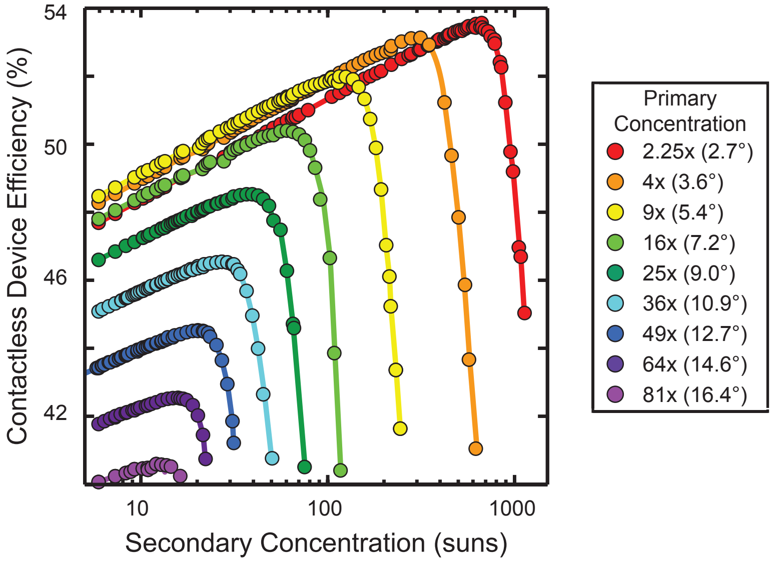

FIGURE 3.11: Contactless device efficiency as a function of secondary concentration for different primary concentration values. Each point represents an individual ray tracing simulation. The lines are guides for the eye. The output angle in air of the primary concentrator is in the parentheses. Contactless device efficiency generally increases with decreasing primary concentration and increasing secondary concentration.

3.3.2 Trimmed Concentrator Geometries

Although the PSR architecture has many designs capable of >50% efficiency, not all of them are attractive for fabrication. The optimum design with 53.6% contactless device efficiency (2.25 suns primary concentration and 664 suns secondary concentration) has a hollow primary concentrator that is 398 mm tall and solid secondary concentrators that are 595 mm in length. The secondary concentrators are far too large for fabrication, and vertical packing is difficult when the module is wider than it is tall. Therefore, we investigated trimming the primary and secondary concentrators to maintain high efficiency designs with shorter concentrators. We trimmed these concentrators by removing length where the CPC is mostly straight, near the input side of the compound parabolic concentrator. This resulted in reduced concentration. For the primary concentrator, the input aperture is decreased with increased trimming for the same output angle. For the secondary concentrator, the CPC must be scaled up after trimming to fit onto the solid prism containing the filters, which therefore increases the output aperture and reduces the concentration. We repeated the optimization of the concentrators to achieve high efficiency designs with smaller concentrators (<60 mm). We also investigated lower cost alternatives (primary concentration >40x) with shorter, cheaper optics.

Figure 3.12 shows the contactless device efficiencies of trimmed structures based on a low (2.25x) primary concentration (Figure 3.12(a)) and a high (81x) primary concentration (Figure 3.12(b)). In these structures the output angle of the primary concentrator is fixed at the value corresponding to the untrimmed CPC (2.7° for the 2.25x case and 16.4° for the 81x case), and the different concentration values correspond to different trimmed CPC lengths. We observe the same trend in primary concentration length for both concentration regimes: a longer primary concentrator, and therefore a higher primary concentration, results in a higher efficiency. This may seem counterintuitive given the trends in Figure 3.11, but the primary concentrators in each trimmed study have the same output angle and therefore the optical splitting efficiency is not reduced at higher concentrations. Thus efficiency increases with increasing primary concentrator length for both studies in Figure 3.12.

However we observe a significantly different trend with trimmed secondary concentration length between the two size studies. In Figure 3.12(a), efficiency intuitively increases with secondary concentration length for structures based on low (2.25x) primary concentration designs. The trimmed designs approach the maximum contactless device efficiency case from Figure 3.11 as the secondary concentrators approach the original lengths. We note that >52% contactless device efficiencies, which could possibly achieve >50% module efficiencies, are still possible with concentrators that are significantly shorter ($\leq$60 mm). By contrast, for the structures based on the 81x primary concentration design, efficiency does not increase monotonically with increasing secondary concentrator length. The new maximum efficiency occurs at a much shorter concentrator length than it does for the untrimmed structure. Additionally, the efficiency for the trimmed structures is unexpectedly higher than the corresponding untrimmed structures by as much as 3% absolute. This is a result of the geometry of the trimmed CPCs, which if trimmed enough can resemble a light pipe with straight sidewalls, as shown in Figure 3.12(c). Interestingly, structures based off of a sufficiently large primary concentration,

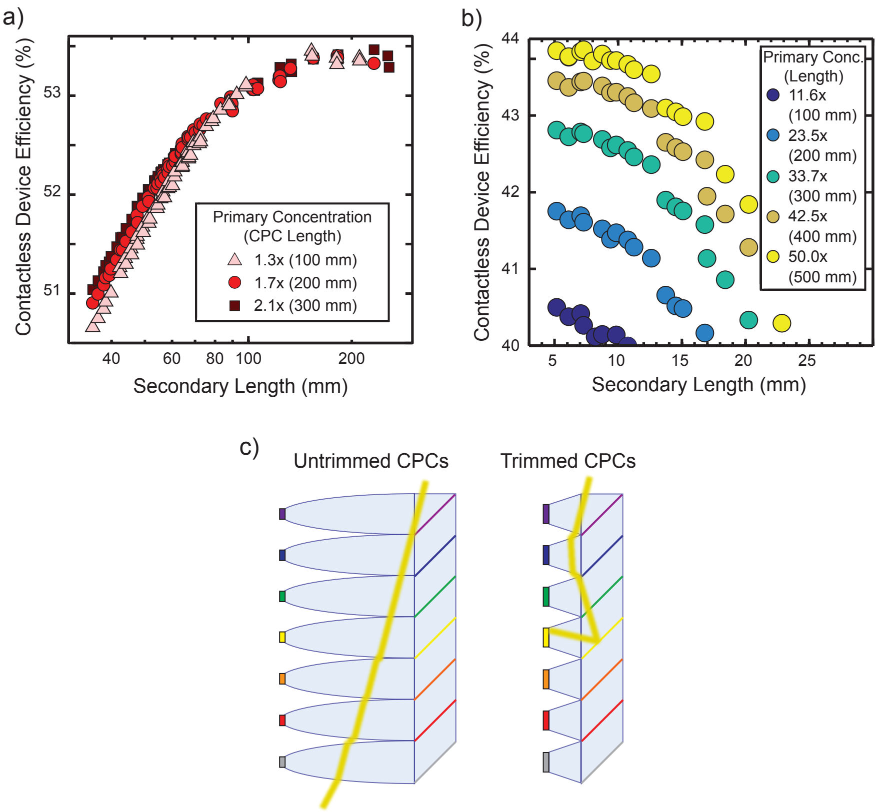

FIGURE 3.12: Contactless device efficiencies versus secondary concentrator lengths for trimmed PSR structures. Each point represents an individual ray tracing simulation. a) Efficiencies for a trimmed PSR structure based on the original 2.25x primary concentrator structure. Longer concentrators approach the efficiencies of the untrimmed structure. b) Efficiencies for a trimmed structure based on the original 81x primary concentrator structure. Significantly shorter secondary concentrators are able to exceed the efficiencies of the untrimmed structure. c) Schematic of PSR with high primary concentration output angles for untrimmed (left) and trimmed (right) secondary concentrators. Light is able to refract back into the PSR for trimmed concentrators.

and therefore a large primary output angle, can direct light to the first secondary concentrator, bypassing the train of filters. This is detrimental for untrimmed structures as the light couples effectively out of the PSR through the mostly straight regions of the secondary concentrators without being converted (left side of Figure 3.12(c)). For the trimmed structures, light can refract back into the structure (right side of Figure 3.12(c)) because of the higher probability of accessing wider angled surfaces, and light is recovered in the lower bandgap subcells. This effect was seen for designs based off a primary concentration of 36x or higher. While none of the trimmed structures based on high primary concentration (>36x) designs achieve >50% contactless device efficiency, it is important to note that these designs can achieve record module efficiencies that are higher than their untrimmed counterparts.

3.4 Calculating Module Efficiency of Selected PSR Designs

We modeled the electrical circuits to determine module efficiencies for five cases of interest. We investigated two regimes: (1) ultrahigh efficiency (>50% contactless device efficiency) designs and (2) high primary concentration ($\geq$50x) designs that could be lower cost alternatives. Table 3.2 shows the optimized geometries for these designs and optical efficiencies. The optical efficiency is defined here as the ratio of the contactless device efficiency generated from the simulation to a contactless device efficiency assuming perfect spectrum-splitting for the same concentration. Cases 1 and 1a are representative cases of regime 1, where Case 1 is an ultrahigh efficiency design for prototyping and Case 1a is the maximum efficiency design for comparison (Figure 3.11). Cases 2, 2a, and 2b correspond to regime 2 and we note that these can potentially achieve record module efficiencies. Case 2 is an optimized trimmed design based on the 81x primary concentrator structure (Figure 3.12). Case 2 is compared to Case 2a, the highest efficiency design for the untrimmed 81x primary concentration series, and Case 2b, the optimum design from the untrimmed 49x primary concentration series. We note that Cases 2 and 2b have very similar contactless device efficiencies, 43.9% and 44.5%, respectively. Even though Case 2b has higher secondary concentration and a smaller primary concentrator output angle, Case 2 approaches the efficiency of the Case 2b geometry because trimmed secondary concentrators facilitate recapture of useful conversion of photons that would otherwise be outcoupled in high primary concentration designs. While the untrimmed designs have much higher concentrations, Cases 1 and 2 approach the efficiencies of the high efficiency, untrimmed comparisons (1a and 2b, respectively) because their optical efficiencies are higher than their untrimmed counterparts, showing that a high optical efficiency is very important for high efficiency.

Cris Flowers then calculated the electrical losses for each design by (1) optimizing the contact geometry for each subcell using a three dimensional distributed circuit model, (2) calculating the resistive interconnection losses, and (3) determining the circuit combination losses from a commercially available power conditioning circuit. The program HSPICE was used to optimize the density of metal fingers in the contact for each subcell by balancing the resistive losses from lateral conduction in the semiconductor layers with the absorption losses from optical shading of the subcell. The process is described in detail in Steiner et al., 2011 [69]. The contact designs were constrained to inverted square geometries and the features were square-cross sections ranging in size from 1-5

Table 3.2: The geometries, contactless device efficiencies, optical efficiencies, and module efficiencies (3μm sized contact features) of the 5 case study designs for determining an overall module efficiency. Cases 1 and 1a represent ultrahigh efficiency (>50%) designs while Cases 2, 2a, and 2b represent high primary concentration ($\geq$50 suns) for lower cost applications.

	Case 1 High η	Case 2 High Conc.	Case 1a	Case 2a	Case 2b
Contactless Device Efficiency (%)	52.4%	43.9%	53.6%	40.8%	44.5%
Optical Efficiency (%)	90.8%	77.8%	90.1%	68.9%	75.6%
Module Efficiency (%)	50.2%	41.9%	50.0%	37.4%	41.1%
Primary Conc. (length)	1.73x (200 mm)	50x (500 mm)	2.25x (398 mm)	81x (1591 mm)	49x (1273 mm)
Secondary Conc. (length)	224x (64 mm)	3x (7 mm)	664x (595 mm)	12x (52 mm)	20x (70 mm)
Overall Conc.	386x	155x	1495x	974x	985x
Cell Size	0.67 mm	5.69 mm	0.39 mm	2.88 mm	2.23 mm

μm wide [70]. Because the fraction of reduced current from contact shadowing varied for different cases and contact geometries, the modified detailed balance calculations and contact optimization were iterated until the calculated shadowed fractions were equal. The resistive interconnection losses were assumed to be 0.03% for all cases, which can be achieved by varying the wire gauges for each case as needed. Finally, calculations of the correct series and parallel connections of subcells within a larger circuit consisting of many PSR modules were optimized to meet the requirements of state-of-the-art DC power optimizers [68, 71]. This process was outlined in [68] and assumed to be have an efficiency of 98.8% for all cases.

Figure 3.13 shows the module efficiency for the five cases as a function of contact geometry. The module efficiency for each case increases with decreasing contact size. The smaller contact sizes are able to achieve a denser array, and therefore reduced lateral resistance, for a smaller overall shadowing fraction. Typically, contacts for concentrating photovoltaics range from 3-10 μm, but even smaller contacts are possible with photolithography [69, 72–74]. For some of the smaller contact geometries (1-2 μm), these module efficiencies actually approach the contactless device efficiencies in Table 3.2, motivating the use of smaller scale contacts. We also note that our two trimmed designs,

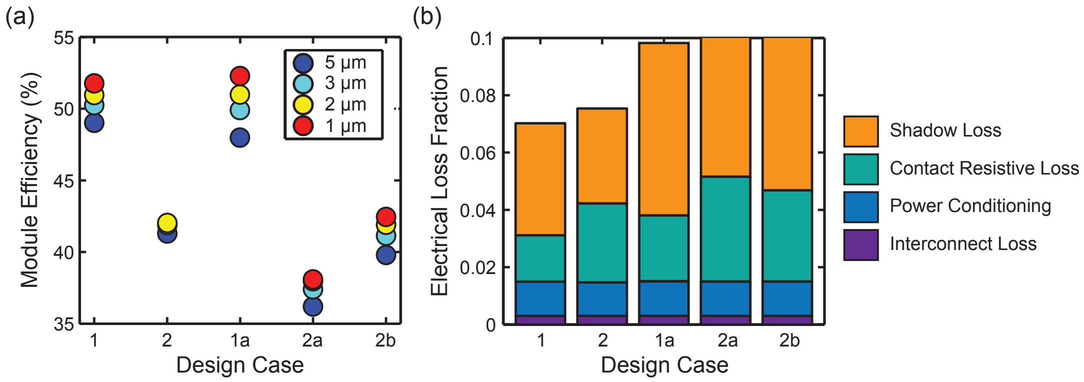

FIGURE 3.13: Module efficiency accounting for optical and electrical losses for the design cases discussed in Table 3.2. (a) Module efficiency for each case with varying contact feature sizes (1-5 μm). (b) Fractional power loss for each case assuming a contact feature size of 3 μm. Electrical simulations performed by Cris Flowers.

Case 1 and Case 2, yield higher efficiencies than their untrimmed counterparts for certain contact geometry sizes. Both of these designs have a lower concentration than their untrimmed counterparts (Case 1a for 1, Cases 2a and 2b for 2) and therefore have lower currents, reducing the number of contact features and shadowing losses and reducing the lateral contact resistance ($P = I^2R$). These concepts are reflected in Figure 3.13(b), which shows a breakdown of the major electrical losses for each case with a contact width of 3 μm. The reduced contact sensitivity and therefore higher electrical efficiencies are shown by the contact resistive losses and shadowing losses being lower for Cases 1 and 2 relative to their untrimmed comparisons. Because we have coupled the losses from each tier (cell, optics, and electronics), we have gained a greater understanding of how to design very high efficiency spectrum-splitting multijunction cells. By properly balancing the design, both ultrahigh (>50%) and record, high primary concentration (>40%, $\geq$50x) efficiencies are possible

3.5 Pathways for Lower LCOE PSR Designs

The PSR design was also further refined and studied for future tech-to-market deployment. Both Kelsey Whitesell-Horowitz and Sunita Darbe have developed cost models of this design to identify cost projections and motivate necessary design changes for deployment. While we have identified many record module efficiency cases (>40%) with relatively high primary concentrations ($\geq$50x), initial cost modeling has shown that the complexity of assembly and the cost of the thick, aperiodic dielectric stack filters could be too expensive to compete with current photovoltaic technologies. Therefore, we have begun investigating two strategies to reduce the cost: (1) high contrast gratings, which can be manufactured through a simple stamping process, as filter alternatives and (2) returning to the 'Generation 1' PSR design as a way to reduce complexity at the cost of efficiency. While these research areas are still young, they have already led to great insight on manufacturing a spectrum-splitting module for commercial applications.

3.5.1 High Contrast Gratings as Filter Alternatives

Although they yield incredibly high spectrum-splitting efficiencies, the multilayer dielectric stacks would be very expensive because each one is produced by vacuum sputtering of hundreds of dielectric layers for a total thickness of 15-20 μm. Recently, high contrast gratings (HCGs) have gained significant attention because of their potential for extraordinary, omnidirectional reflectivity bands using only a nanopatterned metallic or dielectric surface. HCGs comprise of a periodic pattern of subwavelength, high refractive index shapes (i.e., gratings, pillars, etc.) [75–77]. These subwavelength structures support both diffraction modes and waveguide modes propagating through the high index shapes and these modes can interact to generate nearly unity reflectivity over a designed range of wavelengths [78, 79]. These structures can be manufactured through nanoimprint lithography, in which a master stamp is used to pattern these 2-D surfaces in a photoresist. After curing, the patterned surface can be processed with traditional lithography and etching. This process has also been shown to be high-throughput [80].

Sunita Darbe has led the effort on investigating high contrast grating designs that can replace the expensive multilayer, dielectric stacks. She has shown great progress in developing highly reflective structures made from hexagonally packed Si nanopillars [81]. However, some of them are not broad enough reflecting bands for our current design. Broader reflectivities could be achieved by stacking some of the high contrast gratings, much like a chirped filter stack, but this would lead to multiple reflection losses at each layer, reducing the transmission of out-of-band photons and greatly reducing the efficiency [82]. I have attempted to extend this study by investigating structures that overlay two hexagonally packed Si nanopillar arrays that each have a different radius within the same plane, as shown in Figure 3.14. By including two lattices, we expect to constructively interfere for a broader range of wavelengths than with a single radii lattice.

These structures were simulated using the rigorous coupled-wave analysis software RSoft DiffractMod with 12 spatial harmonics [81]. The radius of the smaller nanopillar array,

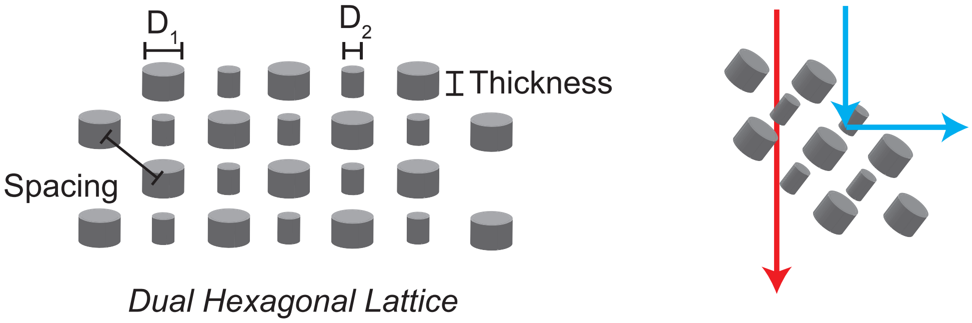

FIGURE 3.14: Schematic of the high contrast grating structure modeled as an alternative filter for the PSR. A dual hexagonal lattice of Si nanopillars with diameters D_1 and D_2 is used to create a broadband, highly reflective structure.

the nanopillar spacing, and the nanopillar thickness was varied to optimize the filter performance. Figure 3.15 shows the reflectivity of the 0th order mode for a single radii lattice and a dual radii lattice for different angles of incidence. The single radii lattice modeled by Sunita Darbe has Si nanopillars with a radius of 150 nm and a spacing of 600 nm with an optimized thickness of 175 nm. The dual radii lattice has Si nanopillars with radii of 175 nm and 10 nm, a spacing of 600 nm, and an optimized thickness (equal for both structures) of 250 nm. The single radii lattice yields a reflecting band with a bandwidth of approximately 200 nm, and as expected, adding in a secondary lattice with a different radii nearly doubles this bandwidth. However, for these current parameters we observe a sharp dip near 950 nm which corresponds to a strong electric field enhancement between the small and large radii nanopillars and reduces the reflectivity from 800-950 nm (see Appendix C). Additionally, there is a strong dependence of average reflectivity on incident angle, with reduced reflectivities occurring for higher angles of incidence. Further optimization is required to fully explore the design space of these structures.

The average transmission of lower energy photons are above 95% for shallow angles (0-30°) and 90% for the original design angle (45°). This has strong implications for the efficiencies possible because misallocation of low energy photons greatly affects the total efficiency of the device. In Figure 3.16, we show the maximum efficiencies possible of a structure using average filter properties for the multilayer dielectric stack (MDS) filters (99% average transmission of lower energy photons, 95% average reflection of in-band photons), a high efficiency HCG (95% transmission, 90% reflection), and a lower efficiency HCG (90% transmission, 70% reflection). The transmission of the high and low efficiency HCGs are the averages of the transmission below the cutoff for 30° and 45°, respectively. The reflection of the high efficiency HCG is the average reflectivity of the

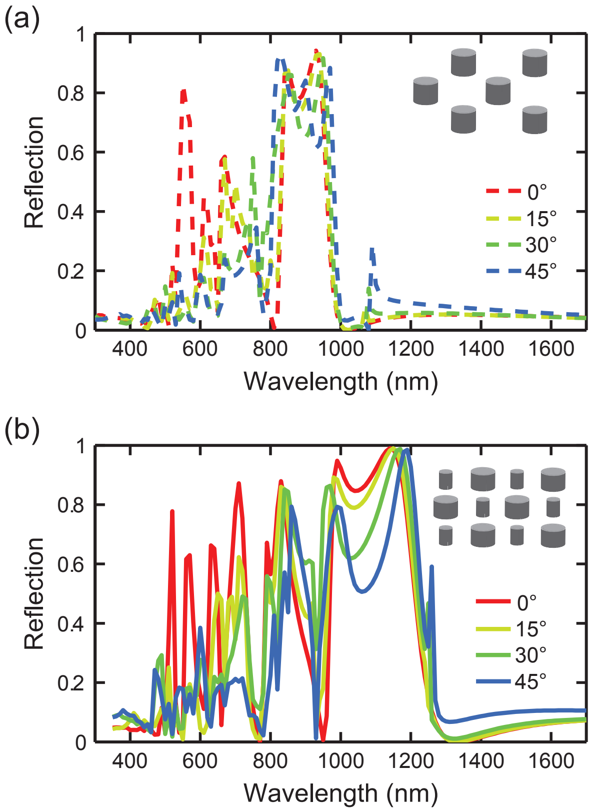

Figure 3.15: Example reflectivities of designed high contrast grating filters for the PSR. (a) A single radii Si nanopillar lattice with a radii of 150 nm, a spacing of 600 nm, and an optimized thickness of 175 nm. Simulations performed by Sunita Darbe [81]. (b) A dual radii Si nanopillar lattice with radii of 175 nm and 50 nm, a spacing of 600 nm, and an optimized thickness of 250 nm.

filters from 1000-1200 nm while the reflection of the low efficiency HCG is the average reflectivity from 800-1200 nm, including the large dip near 950 nm. The reflectivity and transmission for the high efficiency HCG may be possible through further optimization of the design and by changing the geometry of the PSR to incorporate filters oriented at a shallower angle. We performed these detailed balance calculations as a function of number of subcells, using the optimized bandgaps from [4], and assumed a concentration of 100x, a 95% electrical efficiency, and an ERE of 3% and a fraction of ideal J_{sc} of 90% for all subcells. Note that the electrical efficiency and fraction of ideal J_{sc} are reduced compared to the previous study to account for a wider contact geometry, which will have a higher shadow fraction but will be less expensive to implement. Also, these calculations do not account for concentrator losses, which can be taken into account by future ray tracing simulations. Currently, the transmission of lower energy photons is strongly limiting the maximum efficiency of the device, and unlike the dielectric stack filters, the

HCG devices cannot achieve efficiencies beyond 45%. The low efficiency HCG cannot achieve record efficiencies, necessitating further refinement of the design. Additionally, these designs experience a maximum efficiency for a smaller number of subcells because of this misallocation of light, both HCG filters are most efficient for 7 cells. Despite these limitations, these HCGs show the potential for record efficiency (>40%) solar cell modules using filters that can be made via a simple stamping process. Therefore, such structures should be further optimized and quantified to determine their potential for low cost spectrum-splitting solar cells.

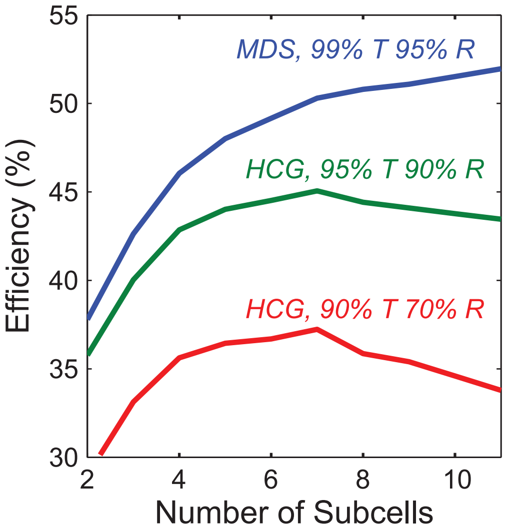

Figure 3.16: Predicted efficiencies from average high contrast grating (HCG) and multilayer dielectric stack (MDS) performances using modified detailed balance calculations. Calculations assume the optimized bandgaps from [4], a concentration of 100x, a 95% electrical efficiency, and an ERE of 3% and a fraction of ideal J_{sc} of 90% for all subcells.

3.5.2 Simplified PSR Design for Very Low LCOE

We also investigated a design that minimizes the number of optical components to reduce the complexity and cost of assembly. This design, shown in Figure 3.17, looks very similar to the PSR Generation 1 design discussed earlier. Here, incident light is concentrated by a solid trimmed compound parabolic concentrator (CPC) before entering a 45° solid parallelepiped flanked by subcells. Motivated by initial cost analyses performed by Sunita Darbe, the design only uses four subcells to minimize the amount of costly III-V material per aperture [83]. This design does not use filters, which significantly reduces the cost by eliminating additional alignment and assembly steps. Like a traditional multijunction cell, the light is split by the absorption in the subcells themselves, and therefore a small loss (2%) will occur at each subcell reflection due to parasitic absorption in the highly doped layers and back reflectors [64].

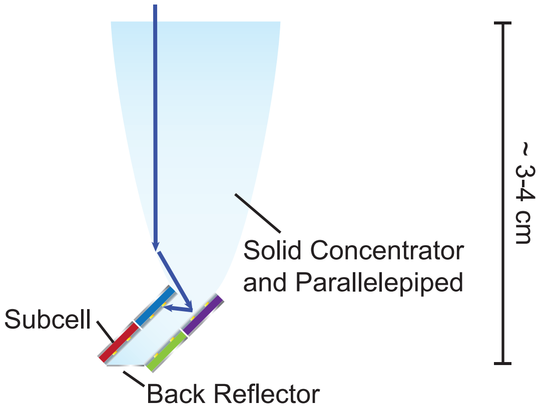

Figure 3.17: Schematic of the low LCOE PSR design. Four subcells are arranged around a 45° solid parallelepiped with a solid primary concentrator. A back reflector is deposited at the bottom of the parallelepiped.

We then performed some ray tracing simulations of this design coupled with modified detailed balance calculations to determine the efficiency as a function of different concentrator sizes (Figure 3.18). The concentration height was varied but limited to 4 cm to maintain a compact, light module. Here we assumed the solid material to be made of a non-absorbing glass with the same antireflection coating used in the previous high efficiency study. We assumed that the subcells had bandgaps of 0.74 eV, 1.15 eV, 1.58 eV, and 2.13 eV and had the same EREs as the previous study.[1] We derated the fraction of ideal J_{sc} and the electrical efficiency to 90% and 95%, respectively, to account for a wider contact geometry, which will have a higher shadow fraction but will be less expensive to implement. Finally, we assumed that 1% of the in-band photons would be downshifted to the next subcell due to reflections off of the contact grid and that 2% of all lower energy photons would be parasitically absorbed at each subcell.

As expected from the previous high efficiency study, there is an optimum concentration that balances the increased subcell voltage with the decreased optical splitting efficiency, and this occurs around 65 suns. However, we note that modules with concentrations >100x can achieve efficiencies approaching 40%, and these are significantly less expensive than lower concentration design points. Higher efficiencies are possible with taller concentrators, but we restricted the study to 4 cm total height to reduce the cost. The cost could be further reduced by molding the parallelepiped-concentrator optic from

---

[1] These are not the ideal bandgaps for 4 subcells, and a small (<1%) efficiency gain can possibly be made by improving these bandgaps.

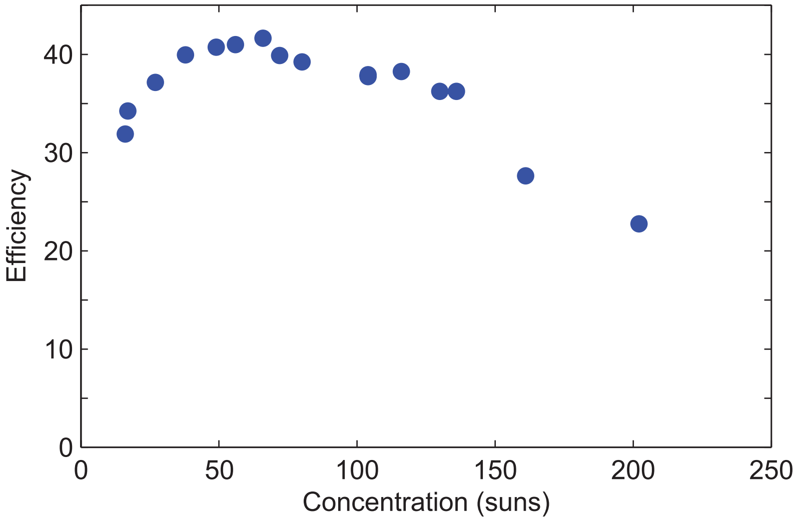

FIGURE 3.18: Efficiency as a function of concentration for the low LCOE design. Efficiencies were determined from ray tracing simulations for structures 3-4 cm in height.

PDMS, which will result in a small reduction in efficiency for some absorption in the PDMS. For example, a design with 116x concentration would achieve a module efficiency of 37%, which is 1.5% lower than a module made of non-absorbing glass. While this efficiency number is very close to record multijunction module efficiencies (38.9% [8]), we note that this design would have a significantly higher annual energy production because the independent connections of these subcells makes the module insensitive to spectral changes [4]. Therefore, further studies of this design could enable a spectrum-splitting design with efficiencies comparable to current multijunction modules but with an improved annual energy yield and therefore a significantly lower cost.

3.6 Conclusion and Outlook

Although spectrum-splitting photovoltaics have been mostly considered an esoteric technology, our work demonstrates the immense potential for these architectures. Here we have designed a spectrum-splitting structure, the polyhedral specular reflector, and modeled its potential module efficiencies from a systems level perspective. We have accounted for the realistic losses in a photovoltaic module by integrating detailed balance calculations, wave optics simulations, ray tracing simulations, and 3D circuit modeling. From these models, we have shown that record efficiencies and even ultrahigh efficiencies (>50%) are possible using cell, optical, and electrical technologies already available to us. Additionally, we have identified various strategies for record module efficiency designs (∼40%) that have the potential to be a low cost, commercial module. Through this study, we hope to inspire new and disruptive multijunction cell architectures that push the limits of photovoltaic module efficiency. In the next chapter, we will attempt to prototype the optics for the polyhedral specular reflector to realize a high efficiency, spectrum-splitting design.

Chapter 4

Optical Prototyping for an Ultrahigh Efficiency Spectrum-Splitting Module

In the previous chapter, we have shown a design, the polyhedral specular reflector (PSR), that has the potential to achieve an ultrahigh solar cell module efficiency (>50%). The analysis included realistic losses for the subcells, optics, and electrical architecture that compose the integrated module. This chapter will describe the efforts toward prototyping the optics for such a module. While fabrication of the subcells and electrical architecture will be crucial for high efficiency, it is necessary to demonstrate that high performance spectrum-splitting optics can be fabricated to prove the potential of spectrum-splitting over traditional tandem multijunction designs. These optics control the photon flux to each subcell and therefore are directly responsible for addressing the largest thermodynamic loss in solar conversion: thermalization and lack of absorption.

First, this chapter will describe the characterization methods for the optical components. Proper analysis of the data will allow us to compare directly to the ray tracing models in the previous chapter and also predict module efficiency and annual energy production. Then, two fully integrated optical prototypes are discussed, showing refinement of the design in response to the quality of the fabricated components. These adjustments allow the second optical prototype to have the potential for a >40% efficiency module. Finally, we will give an outlook on spectrum-splitting multijunction solar modules from our experiences.

4.1 Characterization of the Optics and Predictions for Module Efficiency

4.1.1 Characterization Setup

It is important to both spatially and spectrally characterize each optical component to determine the ultimate predicted efficiency. Thus we have developed a custom characterization setup, as shown in Figure 4.1, to test each component. We used a 1W Fianium supercontinuum fiber laser to provide broadband illumination from 400-1700 nm. We coupled this source to a monochromator, which has a resolution of <2 nm, providing accurate spectral information. Light exiting the monochromator was first split by a tilted glass slide to reflect approximately half of the incident signal to a reference Si diode. This diode helped to monitor any anomalous changes in the incident spectrum from 400-1100 nm, but we note that these changes were small and the signal is incredibly stable after 45 minutes of warming up. Incident light transmitted through the glass slide was then expanded from ~ 3 mm to nearly ~ 2 cm in diameter through a reflective optical beam expander. Depending on the optical component being characterized, the full beam size can be used to illuminate the structure (concentrators, integrated optics) or a reduced beam size using an aperture (diameter $\sim$ 5-8 mm) can be used (filters). The optical component was mounted to a stage with rotational and translational capabilities to center and align the optics to the incident beam. The optics were aligned by directing the reflected beam from the optic through the center of the incident beam.

The reflection or transmission of the optic was measured by both a Si and a Ge photodetectors to cover the range of wavelengths interested. These photodetectors were mounted on translational stages which can spatially characterize the optical splitting prism. First the photodetector was mounted directly in front of the measured optic to characterize the incident beam. Then the photodetector was placed at the output of the optical component to characterize the reflection or transmission. The measured spectra were normalized to the incident beam and the data from the two photodetectors were stitched together to generate transmission spectra as a function of wavelength and position. These spectra were then be processed to compare to the ray tracing simulations and predict module efficiency.

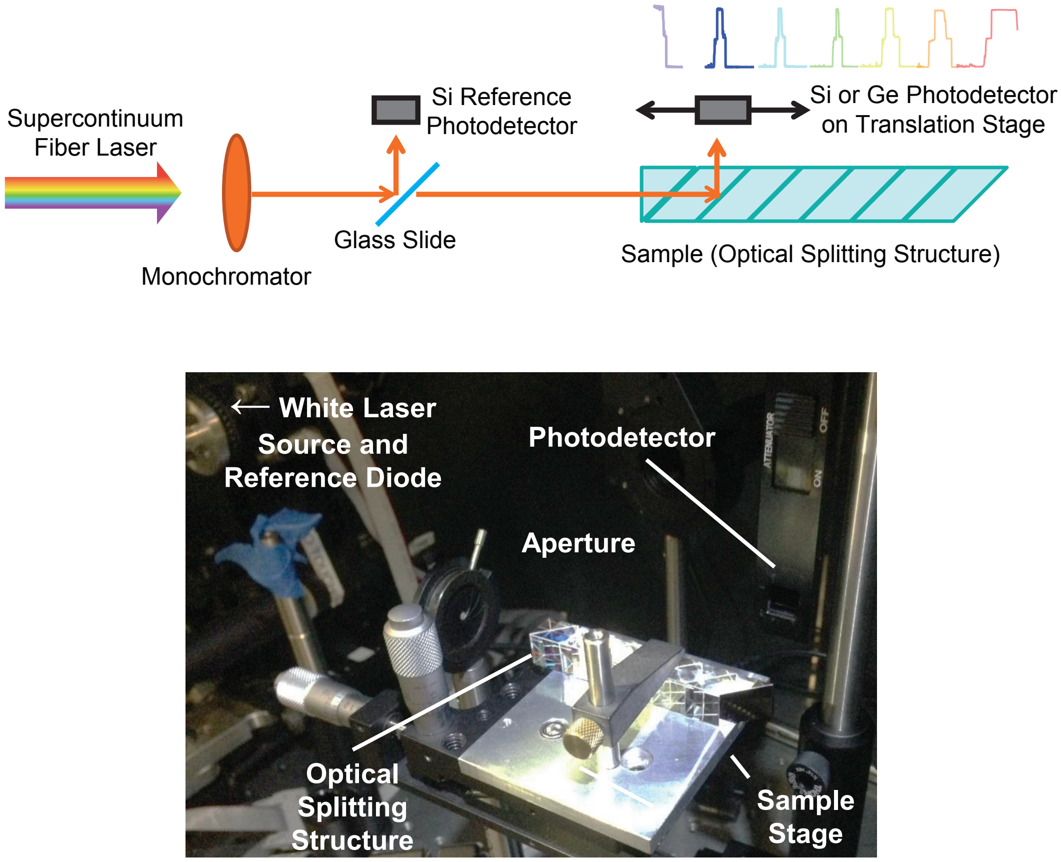

FIGURE 4.1: Schematic and photograph of the setup for characterizing spectrum-splitting optics. Light from a Fianium supercontinuum fiber laser coupled to a monochromator provides illumination for the spectrum-splitting optics. Exiting light is detected by silicon and germanium photodetectors and a silicon reference photodetector is used to detect changes in the incident spectrum during measurement.

4.1.2 Useful Parameters to Calculate from Measured Spectra

Because the previous measurement allowed us to characterize the optical components spatially and spectrally, we can easily calculate different efficiencies and predict the performance of the module using these optics. Similar to predicting the efficiency from the ray tracing simulations discussed in the previous chapter, the measured transmission spectra can be weighted by the AM1.5D spectrum and input to the detailed balance calculations using the same external radiative efficiencies (EREs) and electric simulations to yield a *predicted module efficiency*. This provides a good figure of merit for a fully integrated optical prototype. The MATLAB code that extracts the raw data and determines these efficiencies is in Appendix D. For individual optical components, we can also calculate the optical efficiency. The *optical efficiency* is defined as the detailed balance efficiency using the spectra from the measured optics divided by the detailed balance efficiency assuming perfect optics. This efficiency is more useful for individual optics: a predicted module efficiency would be artificially high for an individual optic because it does not combine the effect of the spectrum-splitting and concentration together. Additionally, the optical efficiency is more useful than an average transmission efficiency because it weights the photons by power in the AM1.5D spectrum. As a reference, the optical efficiency of our ray tracing model is 90.6% so each optical component needs to be fabricated with extremely high fidelity to approach a high performance.

The annual energy production for a fully integrated optical prototype can also be predicted and provide an excellent comparison to currently deployed solar cell modules in the field. Similar to predicting a module efficiency, the *predicted annual energy production* is calculated by weighting the measured transmission spectra by a year's worth of generated spectra for a given location, provided by [4], and using the same detailed balance calculation and electrical efficiency as before to determine the cumulative energy generated. Here, we have chosen Phoenix, Arizona because it has a high percentage of direct sunlight (74%) and has a concentrating multijunction cell plant for comparison (Amonix 3J module, 37% efficiency, 500-600 kWhr/m^2) [84].

4.2 Prototyping a Polyhedral Specular Reflector with Compound Parabolic Concentrators

First we attempted prototyping a PSR optical module using compound parabolic concentrators (CPCs) as was detailed in the original design. This design has a primary concentration of 1.73x and a secondary concentration of 194x, yielding an overall concentration of 336x, and this design corresponds to a 50% efficiency module (90.6% optical efficiency). The fabrication process is shown in Figure 4.2. The prototype was fabricated in the following order: (1) assembling the optical splitting prism, (2) attaching the solid secondary compound parabolic concentrators with a transparent adhesive, and (3) aligning and attaching the primary compound parabolic concentrator with a mechanical support. In the following sections, we discuss each fabrication step and conclude with the predicted efficiencies.

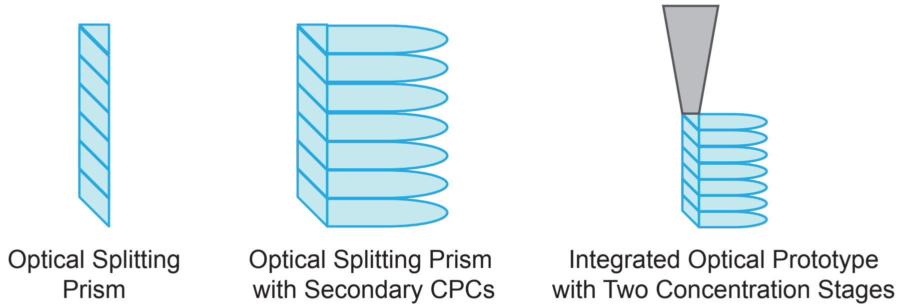

Optical Splitting Prism

Optical Splitting Prism with Secondary CPCs

Integrated Optical Prototype with Two Concentration Stages

FIGURE 4.2: Schematic of the fabrication process for the polyhedral specular reflector optical prototype with compound parabolic concentrators (CPCs). First the optical splitting prism is fabricated, then the solid secondary CPCs are attached to the optical splitting prism, and finally the hollow primary concentrator is aligned to the front of the optical splitting prism.

4.2.1 Optical Splitting Prism

The first challenge for realizing this prototype was fabricating the optical splitting prism, which has seven filters imbedded in a glass prism. To create this structure, seven small glass prisms (triangular and parallelepiped shapes of Corning UVFS 7980) were fabricated as substrates for the filters which could then be glued together to create a monolithic structure. The substrates included bevels on all corners to prevent chipping, which reduced the maximum optical efficiency by 1%. The seven longpass filters were deposited by reactive DC sputtering by Chroma Technology with alternating layers of silica (SiO_2) and either tantalate (Ta_2O_5) or niobate (Nb_2O_5). Tantalate and niobate were chosen as alternatives to titania (TiO_2), which is difficult to deposit as a single phase material. Although these filters use a different material for the high index layers and have a slightly different spectrum-splitting profile (Figure 4.3), they have a nearly identical splitting efficiency (92% as compared to 93% in Chapter 3).

We decided on polydimethylsiloxane (PDMS)[1] as an adhesive because it is transparent (transparency >>99% for a thickness <1 mm), index-matched to glass, and can strongly adhere two glass substrates together after curing. We had previously explored a traditional optical glue, Norland Optical Adhesive 85, but found it to be a weak adhesive for glass components and incredibly sensitive to routine cleaning procedures with acetone and isopropyl alcohol. The adhesion process for the individual filters is shown in Figure 4.4. First, the outside faces of each glass prism filter were covered in either dry erase marker or kapton tape to prevent any leaked adhesive from depositing on the

---

[1] Sylgard 184 2:1 base to curing agent by weight. Small batches (6 g) were mixed for 2 minutes and defoamed for 2 minutes.

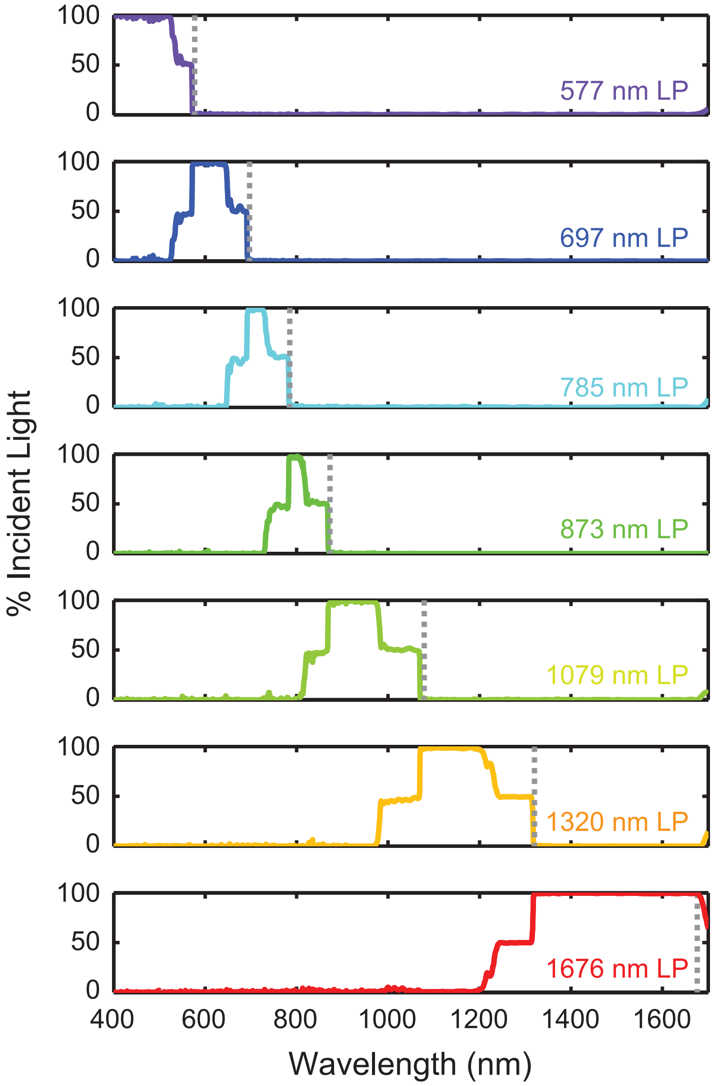

Figure 4.3: Spectrum-splitting calculated from the filter reflections for the PSR prototype. These filters were designed using alternating layers of SiO_2 and either Ta_2O_5 or Nb_2O_5 by Chroma Technology.

non-bonded surfaces. The first glass prism filter (1675 longpass) was placed on a 45° mounting block and approximately 5 μL of PDMS was pipetted on the surface. Then, the next glass prism filter (1320 longpass) was placed on top, contacting the bottom filter of the 1320 longpass to the bare glass face of 1675 longpass glass substrate. The 45° mounting block helped align and support the pieces and additional kapton tape was used as needed to hold the pieces in place. The adhered structure was degassed in a dessicator for approximately 15 minutes to remove any bubbles between the glass substrates. Then, the structure was baked at 80°C for 40 minutes to cure the PDMS. This process was repeated, adding a single glass prism filter at a time, until the entire structure was fabricated. Once the structure was completed, the dry erase marker or kapton tape was removed by gentle scrubbing with optical grade cloth swabs and acetone and IPA. Both the dry erase marker and kapton tape were successful in preventing any excess PDMS from adhering to the outside faces of the optical splitting prism and no delamination of the PDMS bond between the prism filters occurred.

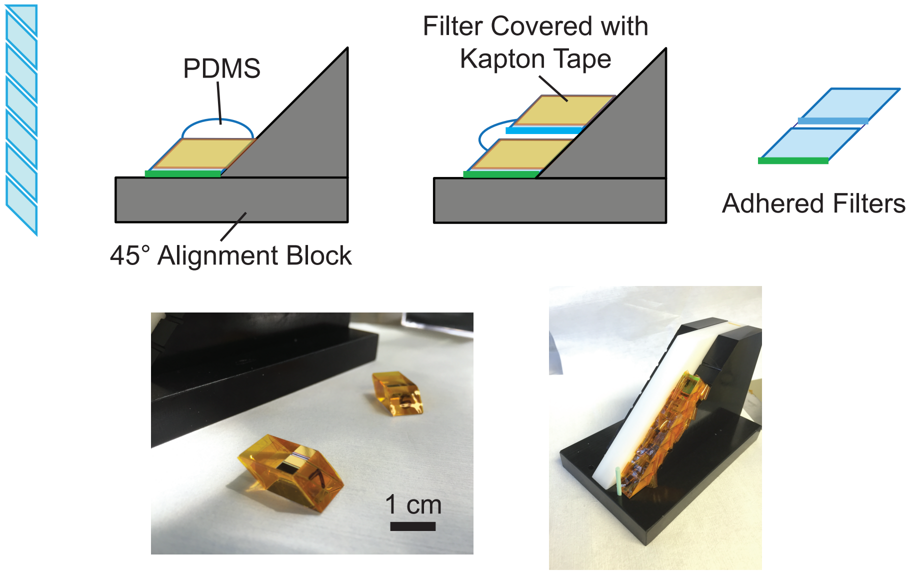

Figure 4.4: Schematic of the fabrication process for the optical splitting prism. The individual glass filter prisms were adhered together using a 45° mounting block for alignment and PDMS to adhere the prisms together.

Figure 4.5 shows the first completed optical splitting prism. The completed structure has uniform and transparent interfaces and clean outside surfaces. Additionally, spectrum-splitting is observed from the blue light reflected from the first filter and orange light reflected from the second filter position - additional colors are not seen since the remaining filters reflect mostly infrared photons. We note that there are some small dust and fiber incorporations within the bonded PDMS layers which resulted from using a dry erase marker and from not working in a clean room. These small defects will cause scattering sites which can reduce the optical efficiency, so the next fabrication was performed with only kapton tape and within a clean room.

The optical splitting prism was measured under an apertured illumination (diameter $\sim$ 3 mm). It is difficult to characterize the optical splitting prism under full illumination because the detector size is exactly the size of the exit face of each filter prism (1 cm by 1 cm) and any misalignment would result in inaccurate characterization. Instead, the incident beam was apertured to a small size and multiple spots were tested to determine

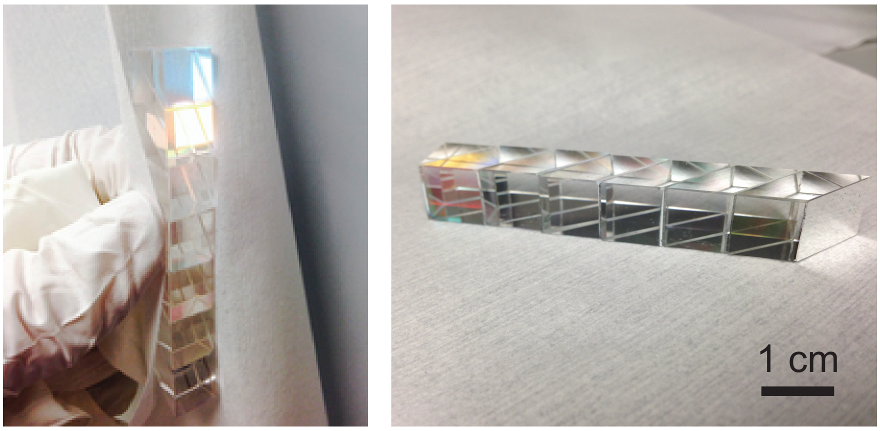

FIGURE 4.5: Images of the first assembled optical splitting prism. Filters grown on glass prisms by Chroma Technology and adhered together using PDMS.

the uniformity. The characterization of the optical splitting prism is shown in Figure 4.6 where the spectrum for each subcell is represented by a different colored line. The Fresnel reflections from the air-glass interfaces at the front and exiting faces of the prism have been corrected for in this plot. We note high reflection of in-band light to each subcell position and minimal reflection of out-of-band light (sub-bandgap photons), which denotes excellent spectrum-splitting. There is a dip near 1400 nm due to glass absorption, but this will not negatively affect the efficiency because this is the same O-H stretch absorption in the AM1.5D spectrum. The calculated optical splitting efficiency for this structure is 90.1% ± 0.2% for the 5 surveyed positions when corrections for the Fresnel losses at each face are made. This is incredibly close to the theoretical 92% optical efficiency. The difference is mostly due to the small misallocation of photons near 650 nm to the first subcell position caused by imperfect deposition of some of the filter layers. These photons have too low an energy to be converted by this subcell and should have been directed to the second and third subcells. Despite this small loss, spectrum-splitting optics can be made with extremely high fidelity.

4.2.2 Optical Splitting Prism and Secondary Compound Parabolic Concentrators (CPCs)

Next the secondary concentrators were adhered to the optical splitting prism. Because of their complex curved faces and the need for optical quality surfaces, these could

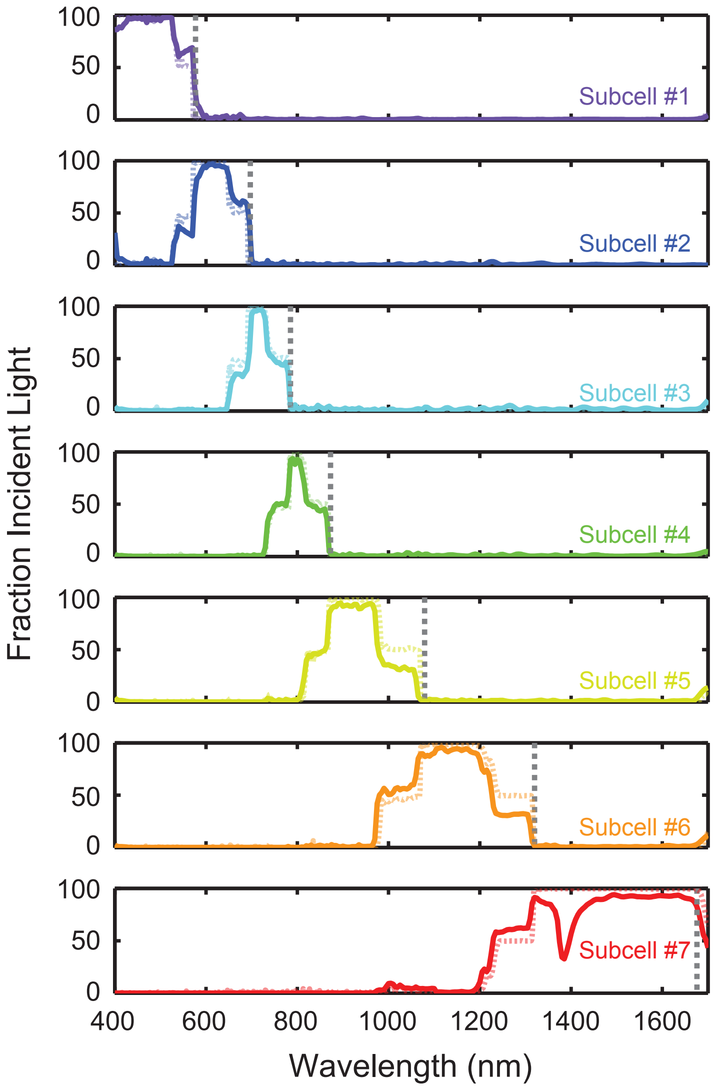

FIGURE 4.6: Characterization of the first assembled optical splitting prism showing the fraction of incident light collected at each subcell position as a function of wavelength (solid). This plot has corrected for the Fresnel reflections at the front and exiting air-glass interfaces. The theoretical filter spectrum-splitting from Figure 4.3 is shown for comparison (pale, dotted).

not be feasibly manufactured from glass at a small, prototyping scale.[2] Instead, these 194x concentrators were molded using PDMS in a process optimized by Sunita Darbe, Michelle Dee, and Dr. Emily Warmann. First, a polished nickel positive mold was created from diamond turning to be the shape of the secondary CPC. The Ni mold was used to generate a low Young's modulus PDMS (Sylgard 184, 10:1 base to curing

---

[2] Injection molding of these concentrators could be an economically feasible way to create high quality optics on the scale of ≥100,000 parts.

agent) negative mold[3] which could then be used to cast higher Young's modulus PDMS (Sylgard 184, 2:1 base to curing agent) concentrators. Excess PDMS was removed from the top of the concentrators through careful slicing with a razor blade. However, the flexibility of the PDMS led to deformation of the concentrator during trimming so many of the concentrators had a slightly angled input face relative to the output face.

Seven of these PDMS CPCs were then adhered to the optical splitting prism with PDMS, as shown in Figure 4.7. Similar to the fabrication of the optical splitting prism, all outside faces of the CPCs and prism were covered in kapton tape to prevent excess PDMS from depositing to the outside of the concentrators and prism. Each CPC was prepared by using scotch tape to remove dust. Then approximately 5 μL of PDMS was pipetted onto one of the filter pieces of the optical splitting prism and degassed for 3 minutes. During this step, an additional 10 μL of PDMS was pipetted onto the input face of the CPC. Although the overall thickness of the PDMS bond should be similar to the bonds between the glass prisms, the CPCs often had some roughness from trimming away the excess material so it was important to infill with PDMS to prevent bubbles from forming and becoming trapped in these textured areas. Then the CPC was carefully placed onto the optical splitting prism and held in position with kapton tape. The structure was then degassed for 30 minutes and baked at 80°C for 40 minutes. The assembly process was repeated until all CPCs were adhered to the prism. The kapton tape was removed and the PDMS surfaces were cleaned with additional scotch tape and the glass surfaces were cleaned with acetone and IPA.

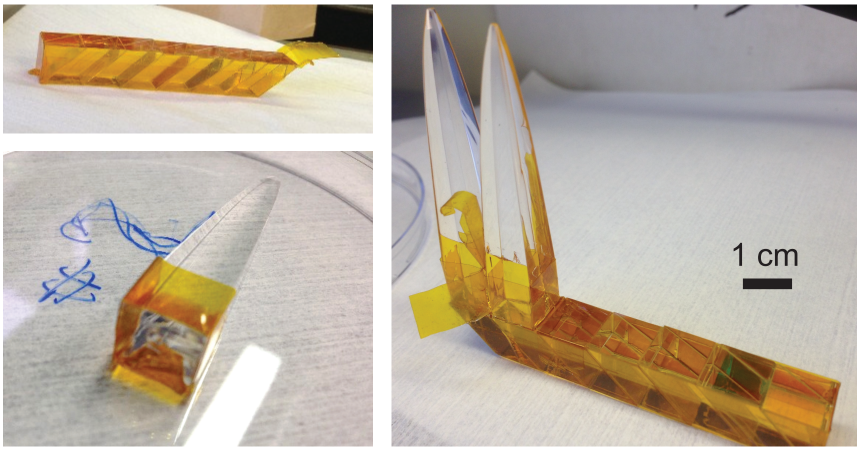

FIGURE 4.7: Images of the adhesion of the secondary CPCs to the optical splitting prism.

---

[3] Longer times were required for degassing (40 minutes) and curing (>40 minutes) the CPCs because of the larger amount of PDMS.

Figure 4.8 shows images of the integrated optical splitting prism and secondary concentrators. Spectrum-splitting and concentration is observed by the collection of different colored light at the tips of the first three concentrators, showing good bonding of the CPCs to the optical splitting prism. However, there is some misalignment of the CPCs from the angled cuts during CPC fabrication which will reduce the optical efficiency.

For characterization, the full area of illumination (1 x 1 cm) was used. Also, the secondary CPCs were placed in direct contact with the photodetectors to ensure good coupling of light. If this had not been done, a significant portion of the light would have been totally internally reflected and the measured spectra would be artificially low. The coupling of the PDMS to the Si and Ge photodetectors was accounted for by normalizing the measured spectra to the signal from the photodetector covered in a thin piece of PDMS. Additionally, the photodetectors were apertured to <1 x 1 mm to prevent collection of scattered light out of the CPC that would not be collected in a subcell.

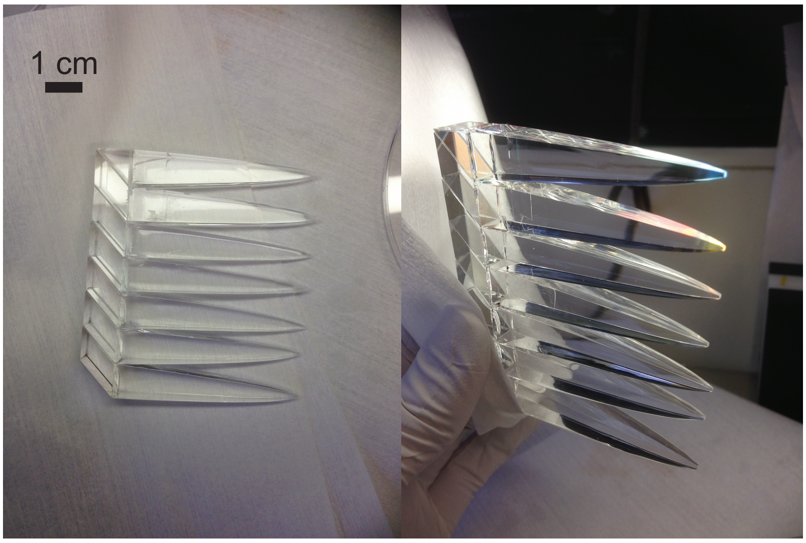

Figure 4.8: Images of the integrated optical splitting prism and secondary PDMS compound parabolic concentrators. The image on the right shows optical splitting and concentration when the prototype is illuminated.

Figure 4.9 shows the spectra for the integrated optics as well as the optical splitting prism alone (dashed) for reference. We observe a significant decrease in collected photons relative to the optical splitting prism alone because of (1) absorption in the PDMS, (2) misalignment of the compound parabolic concentrators (CPCs), and (3) scattering in the CPC surfaces. While PDMS is very transparent for small thicknesses ($\leq$1 cm), there is significant absorption in our CPCs that have a total length of 5.6 cm. At this thickness, PDMS absorbs at least 10% of incident photons in the ultraviolet and visible and as much as 100% for select bands in the infrared. Some of these absorption bands correspond to absorption bands present in the AM1.5D spectrum (e.g., 900, 1200, and 1400 nm), but there is a severe broadband absorption in the infrared that will negatively affect the optical efficiency. Additionally, there are some scattering losses from the CPCs as light is can be seen escaping near the bottom of the CPCs before the output face. Therefore, this structure corresponded to an optical efficiency of 68%, about 20% lower than the original model.

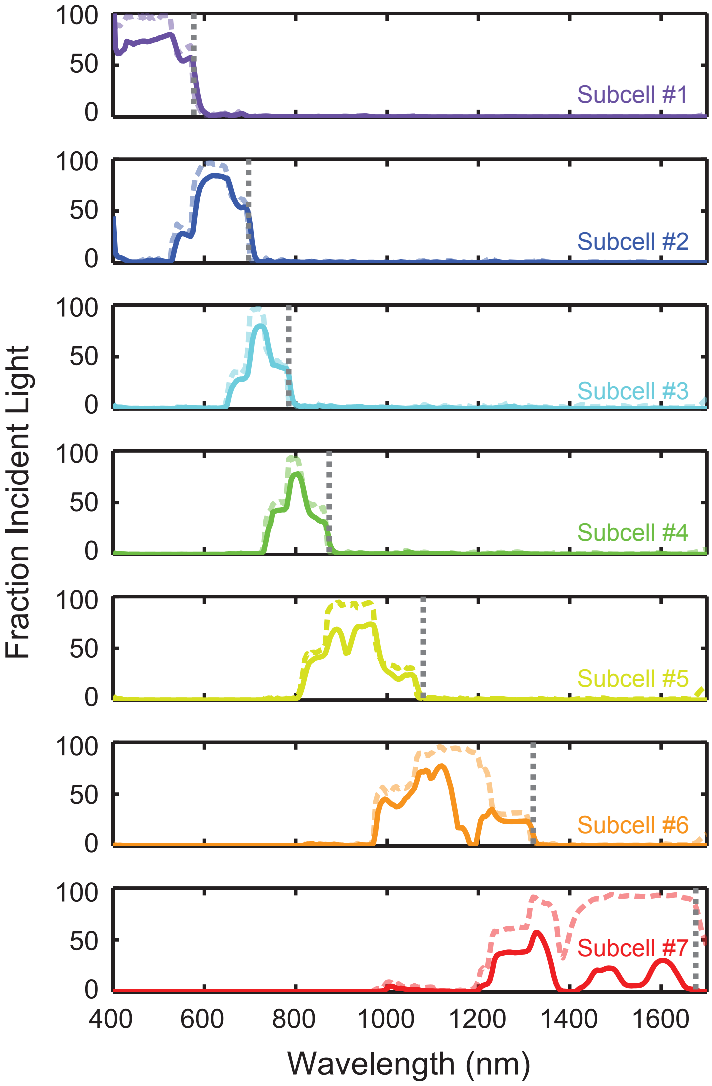

Figure 4.9: Characterization of the integrated optical splitting prism and secondary PDMS compound parabolic concentrators. The fraction of incident light for each subcell position is plotted as a function of wavelength (solid). The characterization of the Fresnel-corrected optical splitting prism alone (pale, dashed lines) is shown for comparison.

4.2.3 Integrated Optical Prototype with Optical Splitting Prism and Two Stages of Concentration

Finally, the hollow primary CPC was fabricated and attached to the optical splitting prism to complete the optical prototype. Because it is a trimmed version of a very low concentration CPC, the sidewalls can be well approximated by a straight line instead of a curve, which significantly simplifies fabrication. The primary CPC fabrication procedure was designed by Dr. Emily Warmann and Cris Flowers and executed by Cris Flowers. The four surfaces of the concentrator were made from 2 mm thick glass with the reflector layers (300 nm Ag and 31 nm SiO_2) deposited on top. The faces were arranged and held in place around a mandrel designed for the concentration level of 1.73x. Adhesive epoxy was carefully applied around the outside edges and after curing for 24 hours, the mandrel was removed. Figure 4.10 shows images of the final primary CPC and the transmission characteristics through the concentrator. Because the input face of the primary concentrator (1.3 x 1.3 cm) was greater than the photodetector size (1 x 1 cm), multiple input spectra were taken and averaged to sample the entire input area. Overall, the CPC shows excellent transmission, maintaining >97% transmission of incident photons for most wavelengths. There are a few dips in transmission near 500, 750, and 1400 nm which we believe are due to a plasmonic absorption at the Ag-glass interface and bulk glass absorption. This structure has an optical efficiency of 96%, which is extremely close to its theoretical optical efficiency of 98%.

The primary CPC was then attached through a mechanical support jig designed by Dirk-Jan Spaanderman. A photograph of this support is shown in Figure 4.11. The optical splitting prism and secondary CPCs are held by the foam spacers where the bevels on the glass prism are. Then the primary concentrator is held by the plastic collar and aligned by adjusting the position of the collar up or down relative to the optical splitting prism. Figure 4.11 also shows the final integrated optical prototype with the primary concentrator aligned and attached to the optical splitting prism and secondary PDMS CPCs.

Figure 4.12 shows the measured spectra for the fully integrated optical prototype (bold, solid lines) alongside the spectra of the optical splitting prism alone (pale, dashed lines) and the optical splitting prism with secondary CPCs (pale, solid lines) for comparison. We observed another significant decrease in the fraction of incident light collected from integrating the primary CPC. This led to an ultimate optical efficiency of 56%. Each subcell position receives about 10% absolute less light as compared to the optical splitting

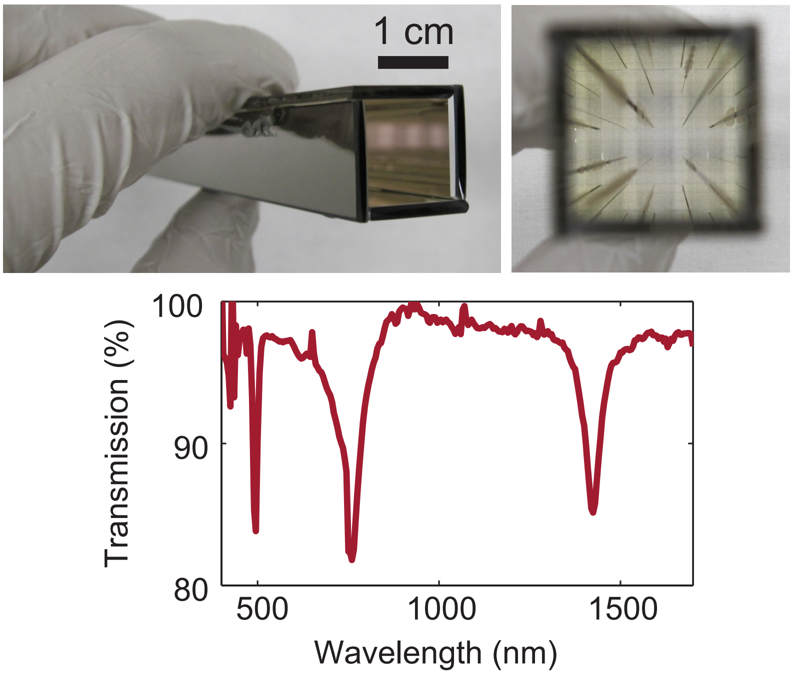

FIGURE 4.10: Images of the fabricated hollow, mirrored primary concentrator. The image on the right is looking down the aperture of the concentrator. The concentrator was assembled by Cris Flowers. (Below) Transmission of the top CPC.

prism and secondary CPCs alone, a much higher loss than expected given the high optical efficiency of the primary CPC. Therefore, we believe this loss is mostly due to the misalignment of the primary CPC, which only had one degree of freedom. The optical efficiency could probably be increased if tilt for both angles were included as a parameter to improve alignment of the primary CPC to the optical splitting prism.

4.2.4 Efficiency and Annual Energy Production

Using the same EREs as in Chapter 3 and assuming the determined electrical efficiency of 97.5% for this design, this optical prototype should correspond to a predicted maximum module efficiency of 30.2%. This is significantly lower than the current module record of 38.9% and a typical deployed Amonix module of 37% — both of which use far fewer subcells (3-4 junctions) and therefore should be less efficient [8, 84]. The annual energy calculated from our prototype corresponds to 670 kWhr/m^2, higher than the 500-600 kWhr/m^2 prediced for the Amonix module [4]. This may seem counterintuitive, but the Amonix module is not always operating at the 37% nameplate efficiency. Because the incident spectrum changes significantly over a year, the average efficiency (annual energy

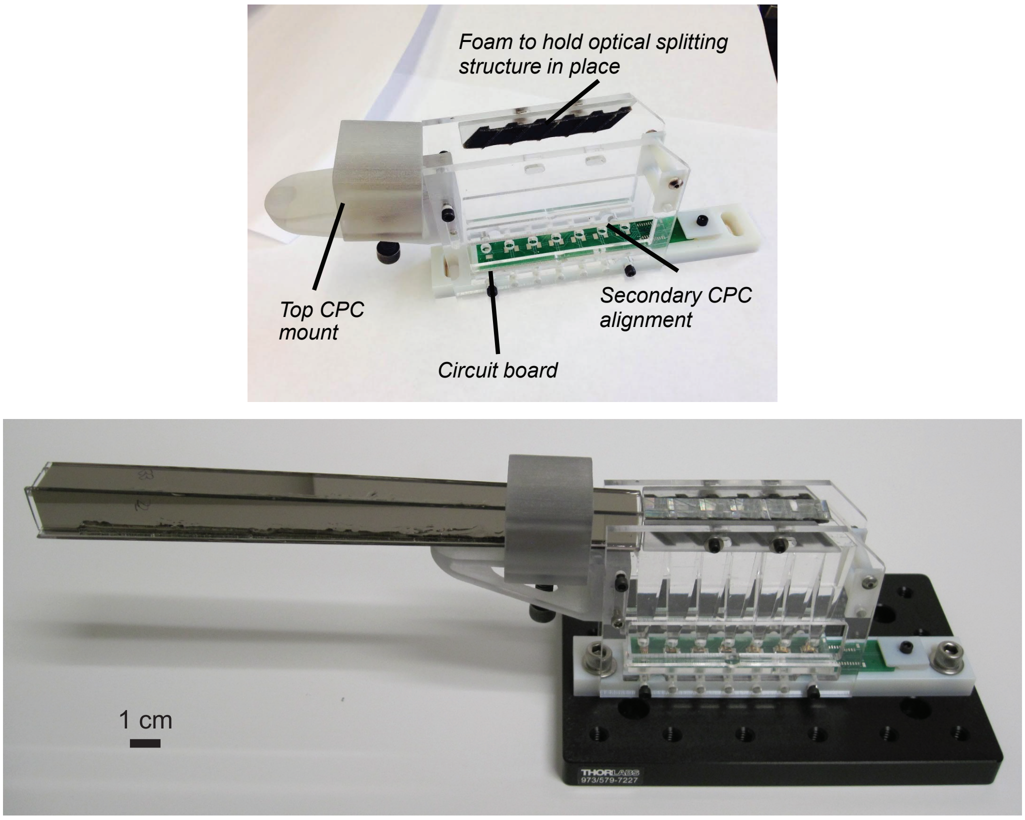

FIGURE 4.11: Images of the mechanical support jig (top) and the final integrated optical prototype with PDMS CPCs (bottom). The mechanical support jig was designed to hold and align the primary concentrator to the optical splitting prism and secondary CPCs. This component was designed by Dirk-Jan Spaanderman.

produced divided by total energy incident) is lower (average efficiency $\sim$ 20%) for the Amonix module because the subcells are connected in series. The PSR has independently connected subcells and therefore operates closer to its nameplate efficiency for most of the time, yielding a higher annual energy production. However, much higher annual energy production and efficiencies should be possible with a spectrum-splitting prototype. Thus future prototyping efforts were devoted to reducing the absorption and alignment losses by investigating more transparent concentrators.

4.3 Prototyping a Polyhedral Specular Reflector with Light-pipe Concentrators

Because of the absorption losses in the secondary CPCs, we directed our efforts toward concentrators that could be fabricated to a high fidelity from low absorbing glass. Thus

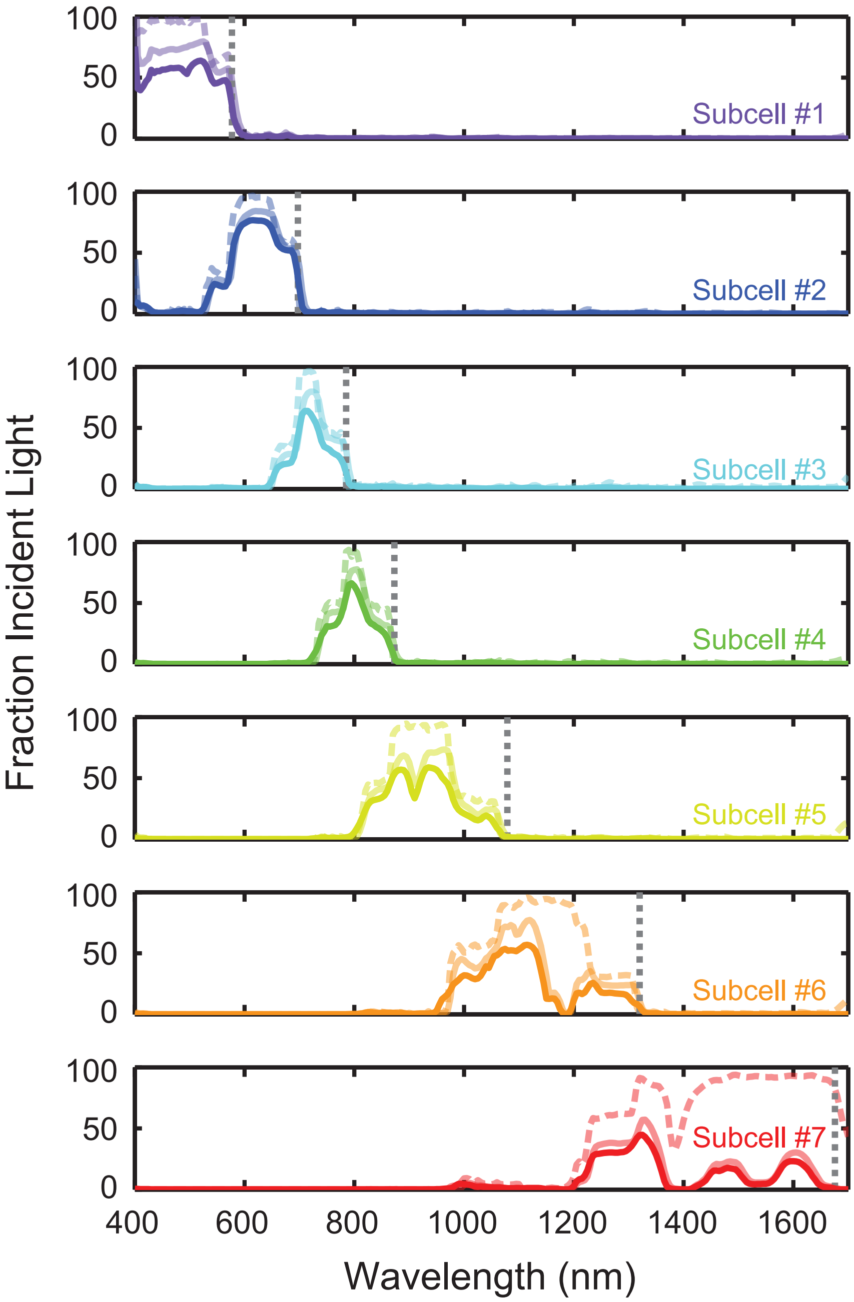

FIGURE 4.12: Characterization of the first fully integrated optical prototype using PDMS secondary concentrators. The fraction of incident light for each subcell position is plotted as a function of wavelength (dark, solid lines). The characterization of the Fresnel-corrected optical splitting prism alone (pale, dashed lines) and the characterization of the optical splitting prism integrated with just the secondary CPCs (pale, solid lines) is shown for comparison.

we adjusted the PSR design to include lightpipe secondary concentrators instead of compound parabolic concentrators (see Figure 4.13). Unlike CPCs, lightpipes have straight sidewalls and look like an inverted, truncated pyramid. This shape is less ideal for concentrator than a CPC. The two intersecting parabolas that create a CPC are designed to ensure the maximum transfer of input photons to the output face with minimal reflections on the surface. By contrast, photons transmitting though a lightpipe will experience many more reflections off of the sidewall because the sidewall curvature is constant, leading to some rejection of incident photons. However, our initial modeling comparing a PDMS CPC with a glass lightpipe shows that this ray rejection is minimal and significantly smaller than the absorption losses (<2%, Figure 4.13).

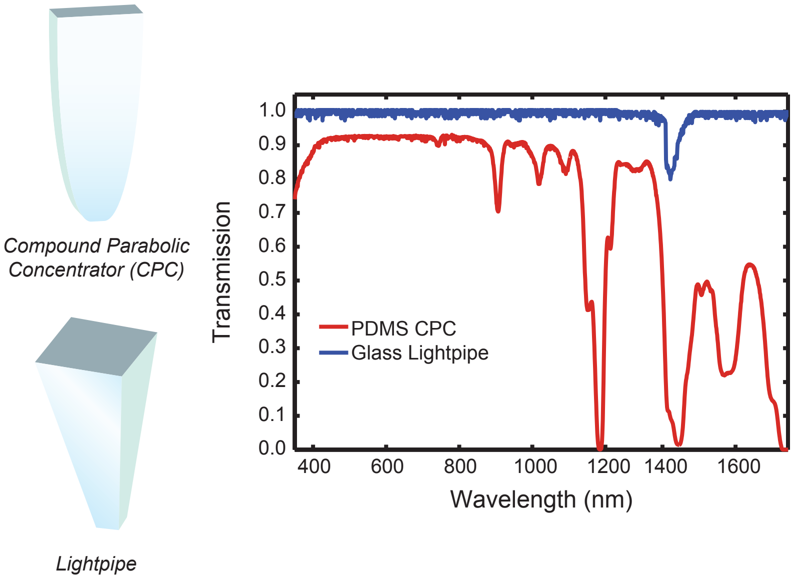

FIGURE 4.13: Schematics and ray tracing transmission of a PDMS compound parabolic concentrator and a glass lightpipe. Material absorption is accounted for but surface scattering is not accounted for. While there is a small amount of ray rejection in the lightpipe, the glass lightpipes will replace the CPCs which are significantly more absorbing.

Here we perform a similar analysis as the previous chapter by optimizing the geometry of the lightpipes to maximize efficiency of the prototype. Figure 4.14 shows the contactless device efficiency, or efficiency without electrical losses, as a function of lightpipe length (x-axis) and lightpipe output size (colored series). The optimized output size is larger for shorter lightpipe lengths and smaller for longer lightpipe lengths. The angle of the lightpipe needs to be shallow otherwise photons will either be rejected from the concentrator or transmitted out of the lightpipe by exceeding the critical total internal reflection angle. Therefore, high concentrations are only available with very long lightpipes (>75 mm). We chose a design with a secondary concentration of 100x (10 cm long lightpipes) and no primary concentration. Because the primary concentrators we had been considering were so small and difficult to align, they would not have a significant benefit for packing and would only decrease the maximum efficiency if not aligned properly. This yielded a design with a 51.5% contactless device efficiency, and, with a 97.5% electrical architecture, a 50% module efficiency (90% optical efficiency).

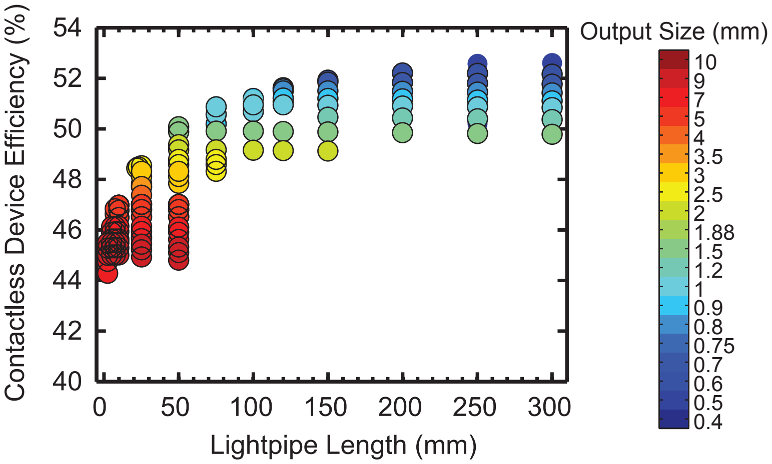

Figure 4.14: Modeled efficiencies of a PSR with glass secondary lightpipe concentrators as a function of lightpipe size. The optimum output size decreases with increasing lightpipe length so longer lightpipes are necessary for high (>100x) concentration.

4.3.1 Optical Splitting Prism

Another optical splitting prism was fabricated using the same procedure as in the previous prototype. This time, dust incorporation was minimized by using kapton tape instead of dry erase marker and by fabricating the prism in a clean room environment. Also, an antireflection (AR) coating, whose performance is shown in Figure 4.15, was attached to the input face optical splitting prism. This coating was designed to minimize the Fresnel reflection losses at the front air-glass interface and maintains an extremely low reflectivity (R <1.5%) over all the wavelengths of interest. This was coating was designed and deposited on 0.2 mm thick Corning UVFS 7980 glass substrates (1 x 1 cm) by Reynard Corporation. These substrates were then adhered to the input face of the completed optical splitting prism using the same PDMS adhesion outlined earlier. The completed structure is shown in Figure 4.16.

The performance of the optical splitting prism is shown in Figure 4.17. Like the optical splitting prism for the CPC prototype, there is excellent division of the incident light

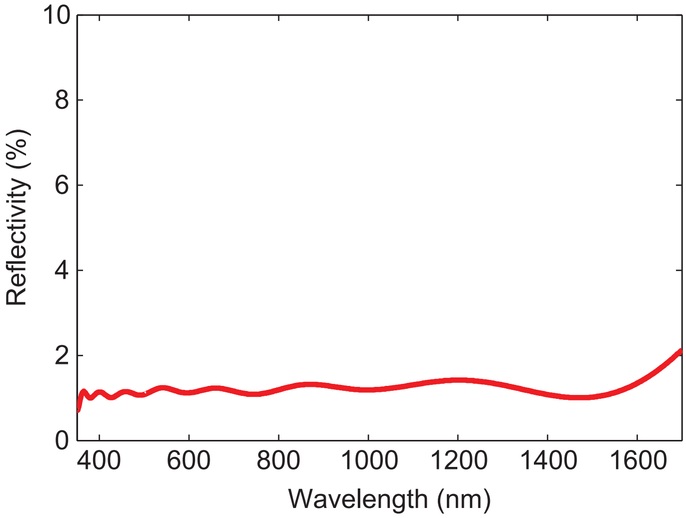

FIGURE 4.15: Modeled reflectivity of the air-glass antireflection coating designed by Reynard Corporation.

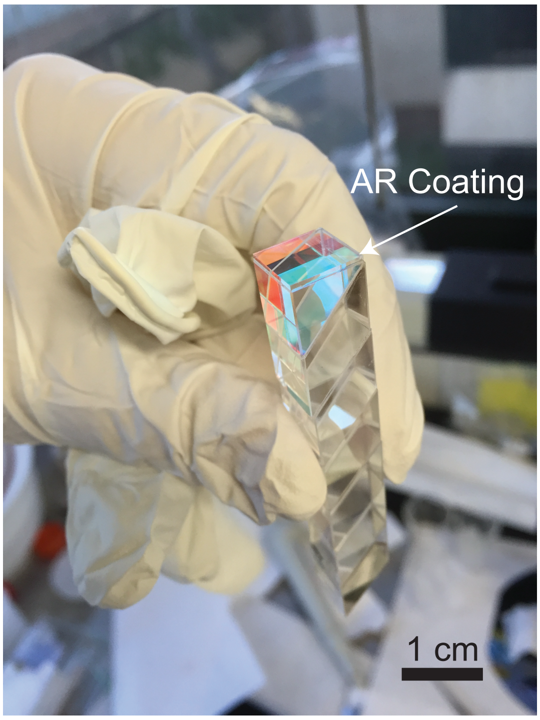

FIGURE 4.16: Image of the second assembled optical splitting prototype with antireflection coating.

and almost all of the photons are distributed to their designated subcell. We again note the absorption dip from the glass substrate at 1400 nm, which will not reduce the optical efficiency because of the lack of photons at that energy in the AM1.5D spectrum. The small reflection by Filter 1 near 650 nm is present again and will reduce the optical efficiency because these photons cannot be converted in the first subcell. Additionally, we observed a new defect near 500 nm: not all of the photons at this energy are reflected to the first subcell. Like the defect at 650 nm, this was most likely caused by imperfect deposition of some of the filter layers. These photons are recovered by the second subcell at a small voltage penalty and should only have a small (<0.5% absolute) effect on optical efficiency. The optical efficiency of this spectrum-splitting structure was calculated to be 89.6%. While this fabrication was fabricated in a clean room environment that reduced dust incorporation, the inclusion of a realistic antireflection coating along with the defects in the first filter caused a slightly lower optical efficiency than the previous round. However, this measured optical efficiency is still very close to the theoretical efficiency (92%) of the model.

4.3.2 Secondary Lightpipe Concentrators

The 10 cm long secondary lightpipe concentrators were fabricated by grinding and polishing fused silica substrates by Izusu glass. A photograph is shown in Figure 4.18. These concentrators appeared very specular when viewed at oblique angles, denoting low surface roughness and low scattering. Concentrators were mounted for characterization using a kinematic rectangular optical mount (Thorlabs KM100C). This mount did slightly obscure the input face, and this was adjusted for in the input signal. The transmission through one of these lightpipes is shown also in Figure 4.18. These lightpipes show very high transmission over all wavelengths of interest (the absorption peak at 1400 nm will not negatively affect the efficiency). The samples measured show an average power weighted transmission of 95%, just slightly lower than the 98% predicted by the initial ray tracing model. This loss is entirely due to surface scattering. When the incident spot size was apertured to <1 mm diameter such that a vast majority of the light would not encounter the surfaces, the transmission of the concentrators increased to 98%. Although the scattering losses may prevent an incorporated module from achieving a >50% efficiency module, they do have the potential for an unprecedented solar cell module efficiency (>40%).

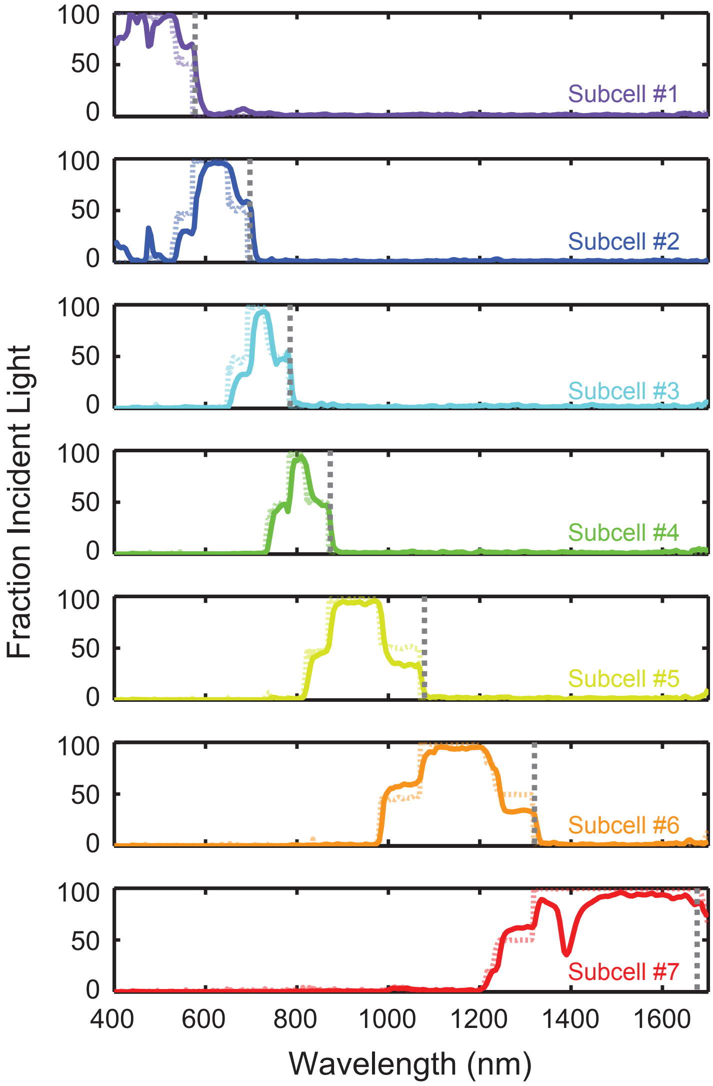

FIGURE 4.17: Characterization of the second assembled optical splitting prism and antireflection coating showing the fraction of incident light collected at each subcell position as a function of wavelength (solid). The theoretical splitting from Figure 4.3 is also plotted (pale, dotted). This plot has corrected for the Fresnel reflections at the exiting air-glass interface.

4.3.3 Integrated Optical Prototype with Optical Splitting Prism and Lightpipe Concentrators

The glass lightpipe concentrators were adhered to the optical splitting prism using the same process outlined in the previous section. The lightpipes were attached sequentially starting at the bottom filter. Again, kapton tape was used to prevent the excess PDMS from depositing outside the glue interface. For better alignment, an alignment jig designed by Annabelle Sibué (Figure 4.19) was used to hold a lightpipe in place on top of

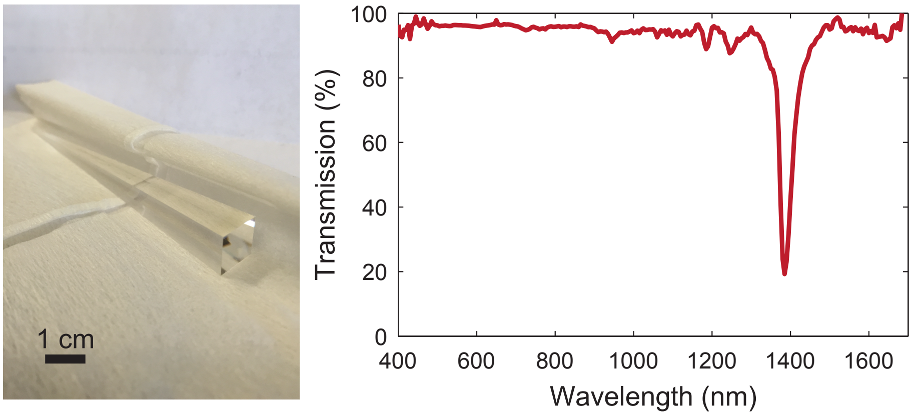

FIGURE 4.18: Image and transmission of a secondary lightpipe glass concentrator. The concentrator is 100 mm long and has a concentration of 100x. The optical efficiency is 95% due to some surface scattering. The absorption band at 1400 nm does not negatively affect the optical efficiency because it corresponds to the same absorption band in the AM1.5D spectrum.

the optical splitting prism during degassing and baking. The clamps on either side of the block firmly held the lightpipe in place, improving the rotational alignment of the lightpipes and preventing movement of the lightpipe during transfer from the dessicator to the oven.

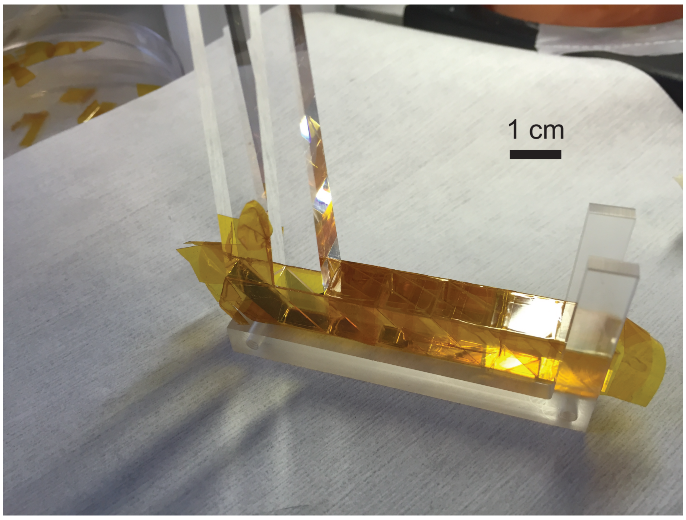

FIGURE 4.19: Image of the in-progress prototype on the alignment jig for the lightpipes. The lightpipe for adhesion is held by the clamps and centered on the optical splitting prism.

The completed integrated optical splitting prism and secondary glass lightpipe concentrators are shown in Figure 4.20(a). Splitting and concentration is shown by the blue, orange, and red light at the tips of the lightpipes. However, the alignment was not perfect, as shown by the images of the final structure in Figure 4.20(b)-(c). The lightpipe for the fourth filter from the top (873 nm longpass) was not perfectly centered on the filter prism and thus not all of the photons for this band will be collected. This misalignment carried through to the remaining filter positions with the first and second filters from the top being the most off-center (Figure 4.20(b)). Also, the lightpipe at the third filter (785 nm longpass) is tilted as a result of the misalignment, which has led to some small bubbles being incorporated that will reduce the transmission through this layer.

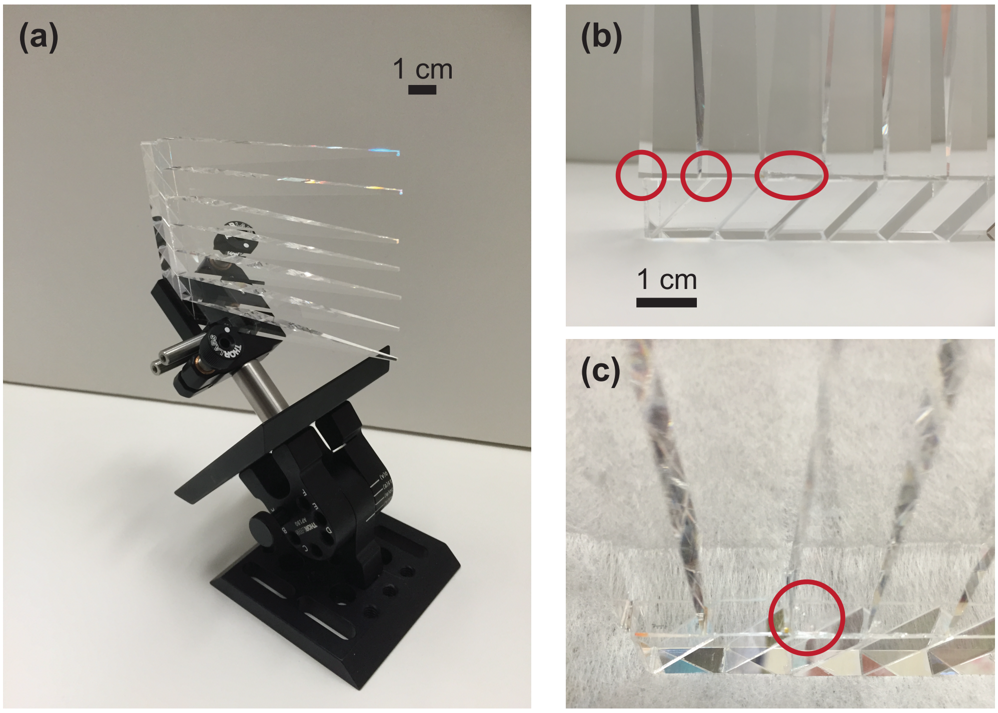

FIGURE 4.20: Images of the (a) completed integrated optical splitting prism and secondary glass lightpipe concentrators and (b)-(c) misalignment details. (b) Red circles denote where the lightpipes are off-centered from the filter prisms. (c) The red circle denotes where some bubbles were incorporated due to the tilt in the lightpipe on the third filter position.

The characterization of the fully integrated lightpipe prototype is shown in Figure 4.21 in comparison the optical splitting prism alone (dashed lines). As expected, there is a decrease in the fraction of collected photons owing to the surface scattering of the lightpipes (all subcell positions) and the misalignment of the lightpipes (subcells 1-4). This misalignment has led to misallocation of some of the photons: both the second and third subcell positions are collecting light designated for the next highest subcell (increase in blue 400-575 nm, increase in cyan 575-650 nm) because the lightpipes are not perfectly centered on these filters. The optical efficiency has reduced to 80%, but is still significantly higher than the PDMS CPC prototype, and therefore capable of much higher module efficiencies.

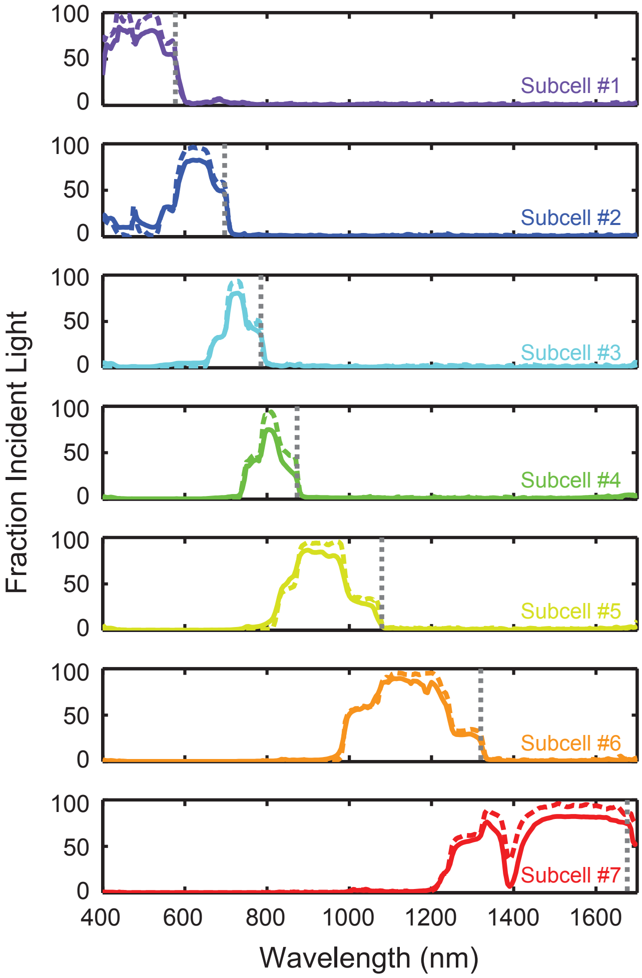

FIGURE 4.21: Characterization of the integrated optical splitting prism and secondary glass lightpipe concentrators. The fraction of incident light for each subcell position is plotted as a function of wavelength (solid). The characterization of the Fresnel-corrected optical splitting prism and antireflection coating alone (dashed lines) is shown for comparison.

4.3.4 Efficiency and Annual Energy Production

Using the same EREs as in Chapter 3 and assuming an electrical efficiency of 97.5%, this optical prototype should correspond to a maximum module efficiency of 42.3%, which would be a significant increase over the current record efficiency [8]. Additionally, this prototype would correspond to an annual energy production of 935 kWhr/m^2 aperture area — besting a typical concentrating photovoltaic plant by more than 300 kWhr/m^2

[84]. Further, a module efficiency of 45% is possible if the alignment of the lightpipes is improved, approaching the efficiencies of current record multijunction cells under artificially perfect concentration conditions [8]. Therefore, these spectrum-splitting prototypes show a high potential for ultrahigh photovoltaic modules.

4.4 Outlook on Spectrum-Splitting Optics

Here we have demonstrated extremely high efficiency spectrum-splitting optics that, with high quality cells and a high efficiency electrical architecture, should achieve record solar cell module efficiencies (>40%) and therefore an unprecedented annual energy production. While this is very exciting, there are still many challenges to address for spectrum-splitting optics. One is the practicality of the modules we have fabricated. These concentrator geometries necessitate vertical packing, the glass components we used for high transparency will add significant weight to the module, and the many optical components increase the cost and complexity of the assembly. Another challenge is the fabrication of high quality optics on a scale large enough for a solar power plant, requiring millions of optical components. However, while our work here may not represent the ultimate design and fabrication process for industrial applications, we believe that our prototyping efforts have demonstrated the potential for spectrum-splitting photovoltaics and will encourage more research toward high efficiency and low cost spectrum-splitting designs.

Chapter 5

Multijunction Solar Cell Efficiencies: Effect of Spectral Window, Optical Environment and Radiative Coupling

The potential for high efficiency devices is due in part to the extremely high external radiative efficiencies (ERE) of III-V solar cells. These high ERE devices are approaching ideal Shockley-Queisser behavior because nonradiative recombination has been largely reduced through advanced growth processes [10, 11]. Additionally, removing the subcell device layers from the substrate via epitaxial liftoff has allowed for elimination of the growth wafer, reducing parasitic absorption losses and increasing the ERE. In the previous chapters of this thesis, we focused on optimizing the input spectra to a set of these high quality, high ERE subcells as a way to achieve ultrahigh efficiencies. However, intelligent design of the radiatively emitted photons in addition to the incident photons can lead to further increases in solar cell efficiency. Here, I will use traditional detailed balance calculations to describe the maximum efficiency limits for novel, spectrum-splitting architectures and show how these architectures can manipulate radiatively emitted photons for higher efficiencies than previously thought attainable.

5.1 Radiatively Emitted Photons in Multijunction Architectures

The optical environment of a cell dictates its overall conversion efficiency. There is a significant entropic loss that arises from the directionality of the incident photons and the isotropic nature of radiatively emitted photons. In the Shockley-Queisser limit for a single junction device, this loss is minimized through the incorporation of a back reflector such that radiative emission can now only exit the front face of the cell, reducing the emission solid angle from 4π to 2π steradians. In a multijunction device, the optical environment is more complex with multiple absorbers, which can lead to interesting possibilities for using this radiative emission. Not only can radiatively emitted photons be trapped within the same subcell in which they were generated, but they can also be directed to and converted in another subcell.

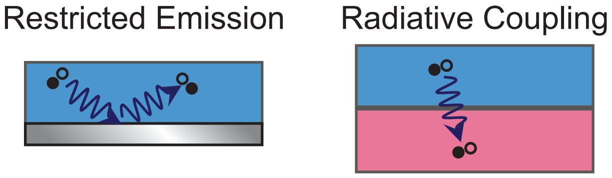

Figure 5.1: Schematic of restricting radiative emission and radiative coupling. Solid and hollow circles represent electrons and holes, respectively. Radiative emission can be trapped in the same subcell it was generated (restricted emission) or directed to and converted in another subcell (radiative coupling).

Figure 5.1 illustrates two possibilities for reconverting radiatively emitted photons in multijunction architectures: (1) restricting emission and (2) radiative coupling. Restricting radiative emission inhibits the radiative emission escaping a subcell in order to reduce the dark current and increase the voltage. This has traditionally been achieved by including a back reflector on a subcell. Recently, more complicated optical structures on the front of the device have been proposed and demonstrated to restrict the radiative emission by reducing the emission solid angle below 2π steradians [12, 13]. By contrast, radiative coupling directs radiative emission between neighboring subcells for reconversion [53, 85]. Cells that have a high degree of radiative coupling have been shown to have higher currents because photons can be redistributed and boost carrier generation in the lower bandgap subcells [54, 86–89].

In the limit of a practical number of subcells in a multijunction geometry (2-20 subcells), radiatively emitted photons would ideally be reabsorbed within the same subcell in which they were generated. Here, the different bandgaps of the subcells are not close enough in energy (difference in bandgaps >0.1 eV) that there is still a measurable thermalization loss in converting a radiatively emitted photon in a lower bandgap subcell. Incorporation of an angle restricting element on the front and a perfect reflector on the back side of each subcell would maximize the radiative emission absorbed in the same subcell. However, fabricating and implementing the angle restriction components described in [13] can be difficult as only very narrow band structures have been experimentally demonstrated. Therefore, it may be interesting to consider multijunction architectures that strongly restrict the radiated emission (i.e., using back reflectors on each subcell) and have some degree of radiative coupling to improve solar cell efficiencies. Until now, optical interactions in multijunction cells have been constrained to tandem geometries, where subcells are directly stacked on top of one another. These geometries are limited in that they can only optimize for strong restricted emission via a reflector for each subcell *or* for strong radiative coupling, but never achieve both simultaneously. However, it is possible that both effects could be optimized for in a spectrum-splitting geometry where the position and orientation of subcells are free parameters.

This chapter investigates how spectrum-splitting architectures can be employed to manipulate radiatively emitted photons for higher efficiencies than previously thought attainable. First, we developed a simple model to understand how radiative coupling between subcells with back reflectors can improve multijunction performance and compare this to the previously assumed maximum efficiency case. Then, for cells that do not utilize radiative coupling, we experimentally verified decreases in subcell voltages and efficiencies for architectures that incorporate back reflectors on all subcells. Finally, we determined the overall ensemble efficiencies for spectrum-splitting architectures and compared these to previously studied tandem structures. We show here that spectrum-splitting geometries have the potential for higher efficiencies than traditionally studied multijunction architectures because spectrum-splitting geometries can both strongly restrict radiative emission (back reflector on every subcell) and recycle the externally radiated photons (radiative coupling).

5.2 Example Multijunction Geometries

5.2.1 Tandem Stack Architectures

We first review the traditionally studied multijunction architectures, tandem stack geometries, that have been studied extensively in the literature [53]. Figure 5.2(a)-(c) show schematics of these geometries: the traditional tandem stack, the air-gap tandem stack, and the selective reflector structure [53]. In all of these structures, subcells are stacked in order of decreasing bandgap such that the incident spectrum is divided by above-bandgap absorption of the subcells [7, 53]. These structures all contain a perfect back reflector for the lowest bandgap subcell (red), but the optical environment between the remaining subcells determines the degree of restricted emission or radiative coupling. The traditional tandem stack geometry in Figure 5.2(a) represents the current technique of growing multijunction cells in which subcells are epitaxially grown on top of one another. All of these subcells are traditionally made of III-V compound semiconductor alloys that have nearly identical indices of refraction, creating a structure where all of the subcells are in intimate optical contact with one another. Therefore, there is almost no restriction of radiative emission within a subcell, with the exception of the bottom subcell, but nearly perfect radiative coupling because of this index matching.

The air-gap tandem structure in Figure 5.2(b) represents a multijunction geometry that restricts some of the radiative emission while maintaining some optical communication between the subcells. Unlike the traditional tandem stack, this structure has an air gap between each subcell that prevents direct emission into the next subcell, increasing the radiative emission trapped within the same subcell and boosting the voltage of that subcell. Also, some of the radiatively emitted photons that escape the subcell can be radiatively coupled as long as they are emitted through the rear face and directed toward a subcell than can convert them. Previous studies have shown that this architecture can achieve the maximum efficiency for multijunction cells in the limit of infinite bandgaps (86.8% for a 6000K blackbody source) because the difference between bandgaps, or spectral window, is small enough that the thermalization losses associated with radiative coupling are minimized. However, this structure is not the most efficient for a finite number of subcells because the combination of restricted emission provided by the refractive index contrast of the air-semiconductor interface and some radiative coupling is not as efficient as the restricted emission provided by a back reflector in this limit [53, 54, 90, 91].

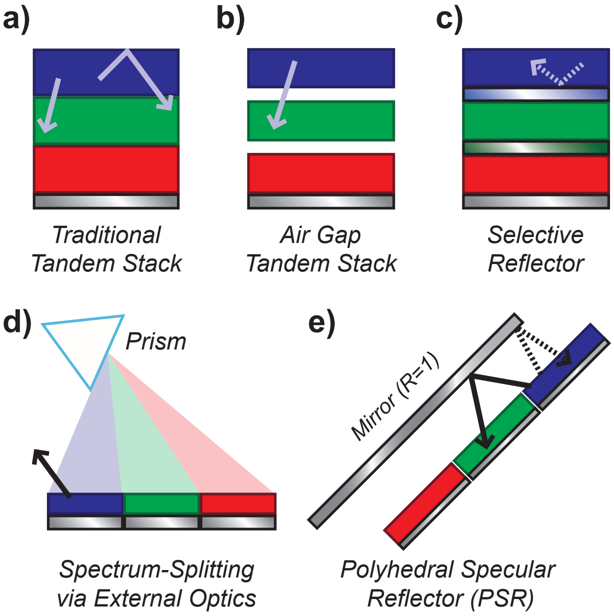

FIGURE 5.2: Schematics of various multijunction cell architectures. Solid arrows denote photons that are radiatively coupled from the blue subcell to the green subcell and dotted arrows denote radiatively emitted photons that are trapped in the same subcell. Structures (a)-(c) represent traditional multijunction architectures that have been studied previously [53]. Structures (d) and (e) represent more novel spectrum-splitting architectures in which subcells are spatially separated from one another. This offers an interesting possibility for radiative coupling between subcells that each have their own back reflectors.

The selective reflector structure (Figure 5.2(c)) includes reflectors on each subcell that prevent radiative emission from the rear face, and thus it does not have any radiative coupling. The selective reflector is defined to be a mirror with unity reflectivity (R = 1) at all photon energies above the energy gap of a given subcell and zero reflectivity (R = 0) for all photon energies below the energy gap [53]. This is different than a back reflector that has unity reflectivity at all photon energies, which would not be compatible in this architecture. The selective reflector has the same benefit as a back reflector for a given subcell but it can also restrict radiative emission for the next subcell if the difference between bandgaps, or spectral window, is small enough to reflect the radiative emission of the next lowest subcell (number of subcells >40). This design has been identified to be the most efficient structure for a discrete number of junctions in the literature [53]. However, these selective reflector designs have not been realized in practice for monolithic multijunction solar cells; it is extremely difficult to create an omnidirectional filter operating underneath a high index layer. We describe through this work that geometries not constrained to a tandem stack can meet and even exceed the efficiency of this design.

5.2.2 Spectrum-Splitting Architectures

As discussed in the previous chapters of this thesis, spectrum-splitting geometries have recently regained popularity as multijunction cells begin incorporating more subcells ($\geq$4). In the architectures studied here, light is split and distributed onto a set of independently grown subcells by either an external optical element or by manipulating the packing of the subcells in the structure. A schematic of the spectrum-splitting structure using an external optical element, such as a prism or hologram, is shown in Figure 5.2(d) [55, 61]. Incident light is divided into different frequency bands by the external optical element and each band is directed toward the subcell best tuned to convert that band. This structure allows for back reflectors on each subcell, which, unlike the selective reflector, have no requirements for transparency below the subcell bandgap and therefore will be easier to design. This design also assumes no radiative coupling between subcells. It will be functionally very similar to the selective reflector structure in the regime where the selective reflector does not restrict radiative emission of the subcells below it (i.e., $\leq$20 subcells).

However, spectrum-splitting structures can also couple radiatively emitted photons from the front surface of a subcell with intelligent design of the architecture. An example of this is shown in Figure 5.2(e) with the simplified polyhedral specular reflector (PSR) design [55, 56, 59, 63]. Here each subcell, complete with its own back reflector, is placed at a 45° angle in order from highest to lowest bandgap opposite a mirror also at 45°. Similar to the multijunction designs in Figure 5.2(a)-(c), incident light is split by above bandgap absorption but in this design, light that is not absorbed is directed to the next subcell via specular reflections off of the back reflector and opposing mirror. The PSR is particularly interesting because light trapping and radiative coupling are inherent in the geometry, shown by the rays in Figure 5.2(e). The solid ray shows a radiatively emitted photon that is downshifted to the next subcell and the dotted ray shows a radiatively emitted photon that is reflected back onto the same subcell. Because this geometry can recycle radiatively emitted photons between subcells that have back reflectors, we show a way to incorporate radiative coupling and strong restricted emission that has not been previously possible.

5.3 Effect of Spectrum-Splitting Optical Environment on Subcell Performance: The Two Subcell Model

Unlike the traditional tandem geometries, a rigorous analysis of the effect of the optical environment from spectrum-splitting architectures has not yet been thoroughly explored. Therefore this section will first explore these effects at the fundamental level of a single subcell within an architecture similar to those described in Figure 5.2(d)-(e). We simplify the analysis of radiative coupling in a spectrum-splitting architecture to a two subcell system in which a higher bandgap subcell radiatively couples to a lower bandgap subcell. Both subcells each have their own back reflector as is enabled by the spatial separation of subcells in spectrum-splitting architectures. A band diagram and schematic of the two subcell model is shown in Figure 5.3(a). Subcell #2, the subcell of interest, has a bandgap of E_g and subcell #1, the source of radiated photons, has a bandgap of $E_g + \Delta$. Both subcells are assumed to be ideal semiconductors that absorb all photons with energies above their respective bandgaps. Subcell #1 receives all photons above its bandgap from the input spectra while subcell #2 is limited to a narrow spectral window, Δ, of the input spectrum. We qualitatively relate Δ to the number of subcells in a hypothetical multijunction cell because adding more subcells to a structure decreases the spectral window on each subcell. For simplicity, we assume that the only radiative coupling mechanism is subcell #2 absorbing photons emitted from subcell #1.

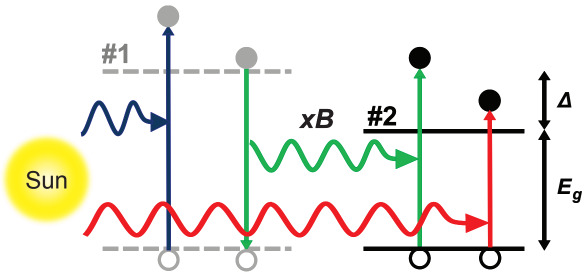

FIGURE 5.3: Band energy diagram and schematic of the two subcell model. Subcell #2 can absorb solar photons from its input spectral window (red) or photons produced via radiative recombination in subcell #1 (green).

We then define a geometric parameter B to describe the radiative coupling from subcell #1 to subcell #2. B represents the fraction of radiatively emitted photons directed from subcell #1 to #2 such that $0 \leq B \leq 1$, analogous to down converting literature, and is determined by the optical architecture of the multijunction cell [92, 93]. $B = 1$

is time-asymmetric because radiative emission is completely downshifted and does not obey absorption-emission symmetry, but we include it in our analysis as an upper limit to this downshifting system [7, 94, 95]. The specific structures we study here have varying degrees of radiative coupling but are still time-symmetric. For example, the traditional tandem stack (Figure 5.2(a)) would have a B of ∼0.93-0.98 because radiatively emitted photons are reflected at the front air-semiconductor interface (large index of refraction contrast) and transmitted through the rear semiconductor-semiconductor interface to the bottom subcell (little to no index contrast) [88]. The air gap tandem stack (Figure 5.2(b)) has a smaller B of 0.5 because there is an air-semiconductor interface on both sides and so radiation is emitted equally out both faces. The generic spectrum-splitting structure of Figure 5.2(d) corresponds to $B = 0$ because its subcells are optically independent. However, not all spectrum-splitting structures are optically isolated. For example, the PSR (Figure 5.2(e)) has some radiative coupling ($B = 0.204$) because some of the radiated photons will reflect off of the mirror and onto the next subcell in line. Although the subcells are not directly in optical contact as in the tandem stack structure, radiatively emitted photons can still be coupled between independently connected subcells.

5.3.1 The Governing Equation of the Two Subcell Model for Radiative Coupling in Spectrum Splitting Architectures

Assuming the subcells in the simplified system are characterized under the 1 Sun AM1.5D spectrum and have a front air interface, we can calculate the power produced in subcell #2 as a function of B and Δ using basic detailed balance principles [5, 96].

First we derive the power produced in subcell #1. Because we are operating under the assumption that the spectral window is large enough that radiative emission from a lower bandgap subcell cannot be converted in a higher bandgap subcell (valid for the regime of subcells we are considering), the power generated in subcell #1 will be the same as a single junction device and therefore have an identical analysis to that described in the Shockley-Quiesser derivation [5].

$$P_2 = V_1 J_1 = V_1 \left[\int_{E_g+\Delta}^{\infty} N_{AM1.5D}(E)dE - \frac{2\pi q}{h^3 c^2} \int_{E_g+\Delta}^{\infty} \frac{E^2 dE}{exp\left(\frac{E - qV_1}{kT_o}\right) - 1} \right] \tag{5.1}$$

where V is the operating voltage of a subcell, J is the current density (A/cm^2) produced in a subcell, $N_{AM1.5D}$ is the photon flux as a function of energy in the 1 sun AM1.5D spectrum, q is the charge of an electron, h is Planck's constant, c is the speed of light, k is Boltzmann's constant, and T_o is the temperature of the subcell (300K). We note that the radiatively emitted photons that contribute to the dark current only occupy the 2π steradian solid angle because each subcell has its own back reflector.

Next, we derive the power produced in subcell #2. This will be similar to the power produced in subcell #1 but will also account for conversion of the radiatively emitted light received from subcell #1, as shown below:

$$\begin{aligned} P_2 =& V_2 J_2 = V_2\Bigg[\int_{E_g}^{E_g+\Delta} N_{AM1.5D}(E)dE \\ &+ \frac{2\pi q}{h^3c^2}\Bigg(B\int_{E_g+\Delta}^{\infty}\frac{E^2dE}{exp\Big(\dfrac{E-qV_1}{kT_o}\Big)-1} - \int_{E_g}^{\infty}\frac{E^2dE}{exp\Big(\dfrac{E-qV_2}{kT_o}\Big)-1}\Bigg)\Bigg] \end{aligned} \tag{5.2}$$

The current in subcell #2 has three important contributions: current produced from the input spectra, current produced from reconverting radiated photons from subcell #1, and the dark current resulting from radiated photons. We note that this subcell also has a reduced angle of emission owing to its back reflector.

5.3.2 Voltage and Power Production in the Two Subcell Model Under Varying Δ and B

We investigate the open-circuit ($V_{oc,2}$) and maximum power voltage ($V_{max,2}$) conditions for subcell #2 to probe the effects of optical environment on subcell performance. Open circuit voltage ($V_{oc,2}$) occurs when the radiative current exactly balances the photogenerated current while the maximum power voltage ($V_{max,2}$) refers to the voltage when power is maximized [97–99]. Under both conditions, voltage increases when the input current for subcell #2 increases. Therefore $V_{oc,2}$ and $V_{max,2}$ increase with increasing Δ. Additionally, for the same value of Δ, a higher B will yield a higher current and therefore a higher voltage. $V_{oc,2}$ and $V_{max,2}$ are plotted in Figure 5.4(a) for an example bandgap of E_g =1.42. Both voltage conditions show a decline with decreasing Δ resulting from subcell #2 receiving fewer photons under the restricted spectrum. This decline is lessened with a higher value of B. The only exception to voltage decreasing with decreasing Δ is when $B = 1$ for $V_{oc,2}$. When $B = 1$, all photons absorbed into subcell #1 are downshifted to subcell #2 and $V_{oc,2}$ equals the V_{oc} of the subcell operating as a single junction, having full access to the entire input spectrum regardless of the value of Δ [5, 99]. We plot these with the voltages for a two subcell selective reflector structure (dotted red) whose derivation can be found elsewhere [53]. Both the $V_{oc,2}$ and the $V_{max,2}$ of a subcell with selective reflectors closely follow the $B = 0$ case for larger values of Δ (Δ >0.6 eV). For smaller values of Δ ($\Delta \leq$0.6 eV), the voltages for a selective reflector case decline much less rapidly, similar to $B > 0$. Until $\Delta \leq$0.6 eV, the spectral window is wide enough that the selective reflector does not restrict any of the radiative emission and so it only acts as a back reflector. Therefore these trends match the voltages of the $B = 0$ case. Only when this curve diverges does the selective reflector subcell have an advantage in voltage over radiative coupling subcells because the spectral window is small enough to incorporate the additional restricted emission of lower bandgap subcells.

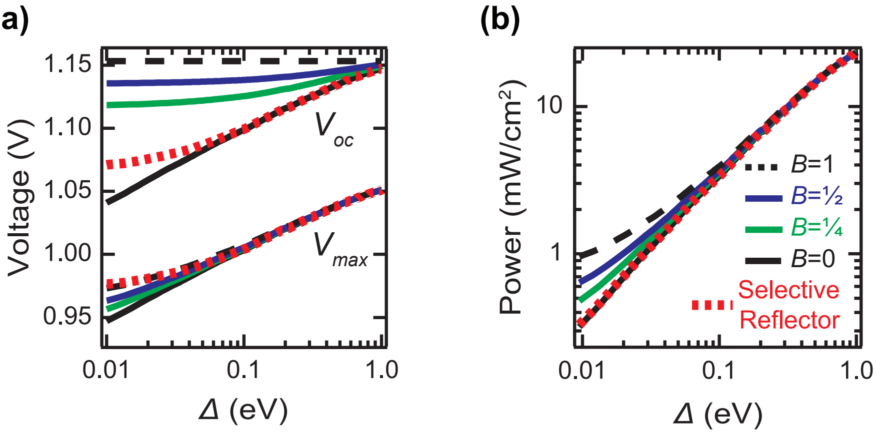

Figure 5.4: Theoretical light I-V subcell characteristics as a function of spectral window, Δ, for a subcell with $E_g = 1.42$ eV (e.g., GaAs) for $B = 0, 1/4, 1/2, 1$. Radiative coupling strongly affects the subcell (a) voltage and (b) power for small values of Δ.

We also study the maximum power (P_2) for subcell #2 in Figure 5.4(b). Similar to the voltage, the maximum power decreases monotonically with Δ because a reduced photon flux will decrease both photocurrent and voltage. This decline is still the most severe for $B = 0$ because there is no radiative coupling to compensate for a smaller spectral window. The inclusion of radiative coupling ($B > 0$) lessens the decline in maximum power due to additional photocurrent. Unlike the previously studied voltage conditions, the power generated in the selective reflector case closely follows the $B = 0$ curve even beyond $\Delta \leq 0.6$ eV. Restricting the emission of a subcell can increase its voltage, but the additional current from radiative coupling in the $B > 0$ cases is more advantageous. However, we recognize that the improvement for the $B > 0$ cases here may be exaggerated due to only studying radiative coupling between two absorbers, and so we study full multijunction ensembles later on to fully elucidate the potential improvements of spectrum-splitting architectures that also include radiative coupling.

5.3.3 Experimental Verification of the Two Subcell Model for $B = 0$

To verify the theory discussed, we measured the light I-V characteristics of a high quality GaAs solar cell in the absence of radiative coupling ($B = 0$) [10, 85]. The cell was an Alta Devices GaAs solar cell which was fabricated via high quality metal-organic chemical vapor deposition (MOCVD) and subsequently removed from the growth substrate by epitaxial liftoff and attached to a flexible substrate with a highly reflective back mirror to prevent radiated photons from exiting the back surface. The current-voltage response of the cell was characterized under a solar simulator under 100 mW cm^{-2} of AM1.5G illumination using a Keithley 238 high current source measure unit. The spectral window was adjusted using longpass filters (cutoffs of 430, 550, 580, 630, 650, 700, and 850 nm)[1] that act as subcell #1 and block photons with wavelengths shorter than the filter cutoff wavelength [100]. Figure 5.5 shows a schematic of the experimental setup.

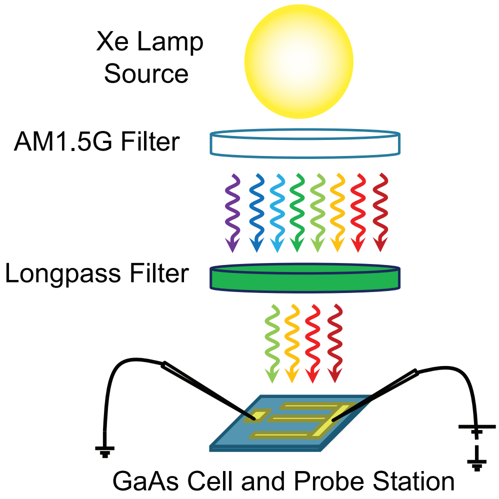

FIGURE 5.5: Schematic of the experimental verification of the two subcell model for $B = 0$. A GaAs solar cell is characterized under the AM1.5G spectrum for different values of Δ which are tuned via longpass filters.

Although this device has significantly reduced nonradiative recombination and therefore approaches ideal material behavior, the original theory proposed in Equation 5.2 had

---

[1] ChromaET430lp, Newport 10LWF-550-B, Chroma HQ580lp, Chroma HQ630lp, Thorlabs FEL650, Thorlabs FEL700, and Thorlabs FEL850.

to be slightly modified to accurately describe the experimental data. First, we included the absorbance of the semiconductor slab ($a(E)$) and a reflection loss due to the lack of an antireflection coating (R). We also added the external radiative efficiency (ERE <1 for a real device) to account for the small nonradiative recombination and parasitic losses in the back reflector [10]. This modified Equation 5.2 for $B = 0$ to the following:

$$\begin{aligned} P_2 = V_2 J_2 = V_2 \Bigg[&(1-R) \int_{E_g}^{E_g+\Delta} a(E) N_{AM1.5G}(E) dE \\ &- \frac{1}{ERE_2} \frac{2\pi q}{h^3 c^2} \left(\int_{E_g}^{\infty} \frac{E^2 dE}{exp\left(\frac{E - qV_2}{kT_o}\right) - 1} \right) \Bigg] \end{aligned} \tag{5.3}$$

This equation was further modified to incorporate the series (R_s) and shunt (R_{sh}) of the actual device following the expressions in [6]. This yielded the following recursive function:

$$\begin{aligned} P_2 = &V_2 J_2 = V_2 \Bigg[(1-R) \int_{E_g}^{E_g+\Delta} a(E) N_{AM1.5G}(E) dE \\ &- \frac{1}{ERE_2} \frac{2\pi q}{h^3 c^2} \left(\int_{E_g}^{\infty} \frac{E^2 dE}{exp\left(\frac{E - q(V_2 + I_2 R_s)}{kT_o}\right) - 1} - \frac{V_2 + I_2 R_s}{R_{sh}} \right) \Bigg] \end{aligned} \tag{5.4}$$

where I_2 is the total current (A). We calculated reflection losses by comparing the measured J_{sc} to the maximum theoretical J_{sc} for a GaAs cell under AM1.5G illumination. This was equal to 35%, which matches the reflection loss between air and a high index semiconductor well. The external radiative efficiency was calculated in a similar way, comparing the actual V_{oc} to the maximum V_{oc} attainable with the realistic J_{sc}. Accounting for the nonradiative losses of the experimental cells corresponds to an ERE of 3.9%, which is comparable to other GaAs solar cells of similar growth quality and back reflector type [10]. Finally, we calculated series and shunt resistances of 2.5 and 2779 Ω/cm^2, respectively, by inspecting the slope of the I-V curve near V_{oc} and J_{sc} as described in [6].

Figure 5.6(d) and (e) shows the dependence of the experimental V_{oc}, V_{max}, and maximum power on the available spectrum in the absence of radiative coupling. We plotted these discrete experimental measurements versus the theoretical dependence of voltage and

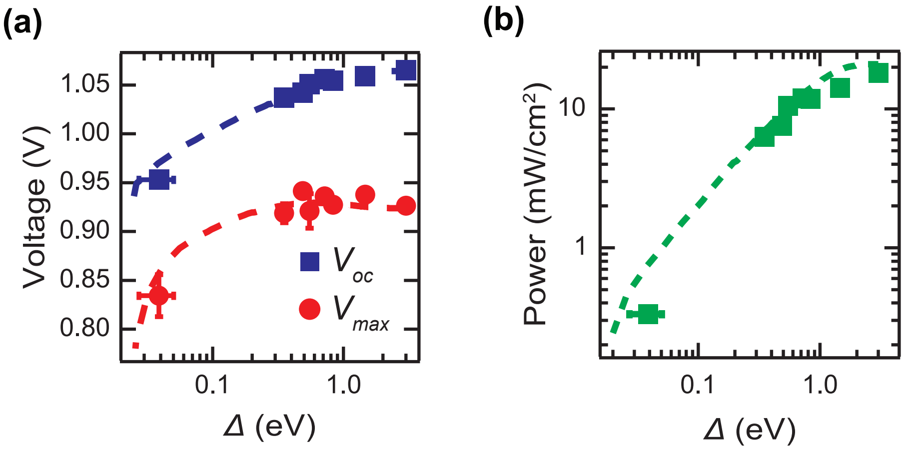

FIGURE 5.6: Experimental verification of the two subcell model for a GaAs subcell with no absorbed radiation from another subcell (i.e., $B = 0$). The (a) measured voltages V_{oc} and V_{max} and the (c) measured subcell power (markers) closely follow the modeled response (dashed lines).

power on Δ in the dashed lines (Equation 5.4). The *ERE* and lack of antireflection coating reduced the predicted voltage and power relative to the original theory (Equation 5.2) while the resistances changed the shape for higher values of Δ. There is excellent correspondence of the data to the our model. All three parameters, V_{oc}, V_{max}, and P_{max} show a significant decline with decreasing spectral windows, which was expected from Figure 5.4.

5.4 Effect of Radiative Coupling and Restricted Emission on Multijunction Cell Efficiencies for 2-20 Subcells

We now extend our analysis of radiative coupling to full multijunction devices. First, the governing equations for each geometry studied will be derived to gain insight on how the optical environment of each geometry affects the subcell radiative emission and use of that emission. Then, we will compare the efficiencies of various tandem and spectrum-splitting geometries for structures with 2-20 subcells and show how spectrum-splitting geometries can meet and even exceed the previously assumed maximum efficiency. Finally, we will conclude with some notes on optimizing spectrum-splitting geometries and how this analysis may be extended to many more subcells.

5.4.1 Governing Equations for the Multijunction Architectures

First we will describe the governing equations for each of the multijunction architectures studied. The MATLAB functions for these equations are given in Appendix E. The power produced in a given subcell, i, for the general spectrum-splitting cases ($P_{i,B}$) is a more general case of Equation 5.2, as shown below:

$$\begin{aligned}P_{i,B} =&V_iJ_i = V_i\Bigg[\int_{E_{g,i}}^{E_{g,i-1}} N_{AM1.5D}(E)dE \\ &+ \frac{2\pi q}{h^3c^2}\Bigg(B\int_{E_{g,i-1}}^{\infty}\frac{E^2dE}{exp\Big(\frac{E-qV_{i-1}}{kT_o}\Big)-1} - \int_{E_{g,i}}^{\infty}\frac{E^2dE}{exp\Big(\frac{E-qV_i}{kT_o}\Big)-1}\Bigg)\Bigg]\end{aligned} \tag{5.5}$$

where i refers to subcell $\#i$ in the structure and $i-1$ represents the subcell with the next highest bandgap. Because we only discuss downshifting structures, we first calculate the power produced in the subcell with the highest bandgap and then continue in order of decreasing bandgap such that the subcell with the lowest bandgap is calculated last. We again note that each subcell has a perfect back reflector as shown by the factor preceding the dark current equaling 2π. This geometry will describe spectrum-splitting via an external optical element when $B = 0$.

The equations for the cases in Figure 5.2 were derived in a similar manner, accounting for the amount of radiated photons leaving a subcell and the fraction of radiative coupling between subcells [53]. The traditional and air-gap tandem stacks are described below by $P_{TS,i}$. Again there are three terms that describe the current generated from the spectral window of the sun, the current generated from radiative coupling with subcell i-1, and the dark current due to radiative emission.

$$\begin{aligned}P_{i,TS} =&V_i\Bigg[\int_{E_{g,i}}^{E_{g,i-1}} N_{AM1.5D}(E)dE \\ &+ \frac{2\pi q}{h^3c^2}(n_{top}^2+n_{bot,i}^2)\Bigg(\frac{n_{bot,i}^2}{n_{top}^2+n_{bot,i}^2}\int_{E_{g,i-1}}^{\infty}\frac{E^2dE}{exp\Big(\frac{E-qV_{i-1}}{kT_o}\Big)-1} \\ &- \int_{E_{g,i}}^{\infty}\frac{E^2dE}{exp\Big(\frac{E-qV_i}{kT_o}\Big)-1}\Bigg)\Bigg]\end{aligned} \tag{5.6}$$

where n_{top} is the index of refraction above the subcell and $n_{bot,i}$ is the index of refraction below the subcell, i. The indices of refraction above and below each of the subcells dictate both the amount of radiative emission leaving the subcell (or, degree of restricted emission) and the fraction of radiative coupling in these tandem stack geometries. The traditional tandem stack has $n_{top} = 1$ and $n_{bot,i} = 3.6$ (the refractive index of a III-V semiconductor) while the air gap tandem stack has $n_{top} = 1$ and $n_{bot,i} = 1$. We note that $n_{bot,i}$ for the last subcell in the stack will be 0 for both architectures because both include a perfect back reflector at the bottom of the stack. Although all subcells i >1 in the traditional tandem stack share a perfectly matched interface with another subcell, we operate in the regime (total subcells ≤20) where the radiative emission from subcell $i + 1$ does not overlap with the bandgap, and absorption profile, of subcell i. Therefore the relevant top interface for every subcell is air ($n_{top} = 1$) in this regime. Additionally, the traditional tandem stack will have a higher degree of radiative coupling and a higher dark current because of the index matching between subcells and high index contrast of the top air interface. The air-gap tandem stack will have less radiative coupling but a lower dark current by comparison.

The power produced in a selective reflector structure is given below by Equation 5.7 [53]. This structure has no radiative coupling and therefore the current is composed only of the generated current from the solar spectral window and the radiative dark current. The radiative emission is completely blocked from the rear surface of each subcell, increasing the maximum subcell voltage beyond that of the previously discussed tandem structures. Additionally, if the subcells' bandgaps are close enough in energy, there is a further restriction on radiative emission, but this effect is negligible in the regime we study (number of subcells ≤20).

$$P_{i,SR} = V_i \left[\int_{E_{g,i}}^{E_{g,i-1}} N_{AM1.5D}(E)dE - \frac{2\pi q}{h^3c^2} \int_{E_{g,i}}^{E_{g,i-1}} \frac{E^2 dE}{exp\left(\frac{E - qV_i}{kT_o}\right) - 1} \right] \tag{5.7}$$

The power produced by the PSR is similar to Equation 5.5 but has two additional terms: (1) C_{geom}, which represents the reduced concentration from placing cells at an angle relative to the input aperture, (2) RB_i, which represents the fraction of photons that are reflected back into the same subcell, reducing the dark current.

$$
\begin{aligned}
P_{i,PSR} =V_i\Bigg[&C_{geom}\int_{E_{g,i}}^{E_{g,i-1}} N_{AM1.5D}(E)dE + \frac{2\pi q}{h^3c^2}\Bigg(B_i\int_{E_{g,i-1}}^{\infty}\frac{E^2dE}{exp\Big(\frac{E-qV_{i-1}}{kT_o}\Big)-1} \\
&-(1-RB_i)\int_{E_{g,i}}^{\infty}\frac{E^2dE}{exp\Big(\frac{E-qV_i}{kT_o}\Big)-1}\Bigg)\Bigg]
\end{aligned}
\tag{5.8}
$$

The angle and position of the mirror determines the deconcentration, fraction of photons downshifted, and fraction of photons reflected into the same subcell, and this is derived for our system in the Appendix F. We only assume radiative coupling between adjacent subcells of the PSR for simplicity. For this geometry, 20.2% of photons are downshifted, 20.7% - 41.4% of photons are reflected back into the same subcell (depending on the subcell position), and that the remaining photons are lost. There is a concentration factor of $1/\sqrt{2}$ owing to the geometry of the structure.

5.4.2 Ensemble Efficiencies for The Multijunction Architectures

We calculated the efficiencies for ideal multijunction cells with 2 to 20 subcells under the 1 sun AM1.5D G173-03 spectrum. The bandgaps for each ensemble were determined by detailed balance optimizations discussed elsewhere [4, 62]. The efficiencies are calculated for the cases illustrated in Figure 5.2 as well as some additional cases from our study ($B = 0, 1/4, 1/2, 1$), as described in the previous section [53]. All cases with radiative coupling assume that absorption of radiatively emitted photons only occurs when the absorbing subcell has a smaller bandgap than the emitting subcell. This assumption is valid for this range of subcells because the vast majority of radiatively emitted photons from a given subcell have too small of an energy to be converted by a subcell with a higher bandgap.

Figure 5.7 shows efficiency as a function of number of subcells for these cases. We show that a traditional tandem stack is less efficient than the air gap structure, as predicted by the previous literature [53]. Although there is a higher radiative coupling for the traditional tandem stack ($B > 0.9$), there is increased light trapping in the air gap structure and so the air gap tandem stack has smaller dark currents and a higher overall efficiency. We also verify previous literature by showing that the selective reflector case is more efficient than the traditional and air gap tandem stack cases because the selective

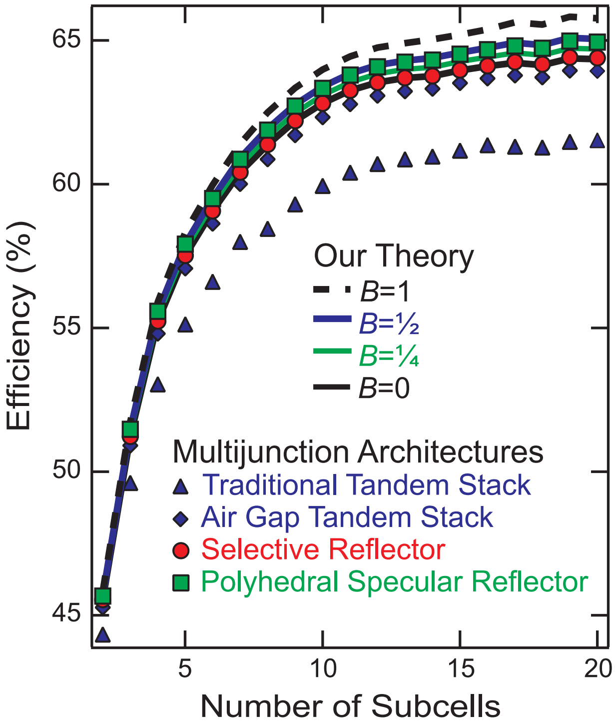

FIGURE 5.7: Theoretical efficiencies for multijunction ensembles as a function of number of subcells. Varying amounts of radiative coupling with back reflectors ($B = 0, {}^1/_4, {}^1/_2, 1$) are compared to the traditional tandem stack (blue triangle), air gap tandem stack (blue diamond), selective reflector (red circle), and polyhedral specular reflector (green square) geometries under the 1 sun AM1.5D spectrum. The polyhedral specular reflector is shown to be more efficient than the previous maximum efficiency case (selective reflector).

reflectors increase light trapping by providing the benefits of a back reflector. In contrast to previous literature, we show that structures can have both radiative coupling and back reflectors ($B > 0$, PSR), and that these are the most efficient for 2-20 subcells. For low numbers of subcells (< 20), the selective reflectors only act as back reflectors and do not restrict emission because the spectral windows encompass the majority of the radiatively emitted photons. Essentially all radiatively emitted photons in the selective reflector case escape the multijunction cell without being recycled and so the dark current is not significantly reduced. This is further corroborated by the fact that the efficiencies for this case are equivalent to our case with no radiative coupling (spectrum-splitting via external optics, $B = 0$), which we have also identified as the worst case in our previous model. By contrast, radiative coupling ($B > 0$) allows these photons to be reconverted, boosting the current in lower bandgap subcells and providing higher efficiencies (up to 1.5% absolute increase) than the selective reflector case, as shown in Figure 5.7. Even the PSR design, which has a concentration <1 because of its geometry, outperforms the selective reflector case because radiatively emitted photons can be recycled within the same subcell and coupled among other subcells. This combined light trapping and radiative coupling also explains why the structure performs closely to the example $B = 1/2$ case even though the equivalent B is less than $1/4$. Thus a spectrum-splitting design that incorporates back reflectors for each subcell with radiative coupling between subcells and/or light trapping could provide a significant increase in efficiency over previous designs [55, 56, 59–61, 101].

5.5 Conclusion and Outlook for Spectrum Splitting Geometries

In this chapter, we investigated how geometry affects the optical environment and therefore the efficiency of multijunction solar cells. We found that spectrum-splitting architectures can have equal or higher efficiencies to traditional designs because they have the capability of excellent radiative emission restriction *and* radiative coupling. Our analysis and experimental results of the two subcell model show the important role of radiative coupling in such a spectrum-splitting structure. If subcells in a spectrum-splitting structure can radiatively couple into other subcells, there is a significant increase in voltage and power. Additionally, we studied maximum efficiencies of multijunction ensembles and have shown that for 2-20 subcells, even higher efficiencies can be obtained than what was previously thought possible by including both radiative coupling between subcells and a back reflector on each subcell, such as through the PSR geometry. This has important implications for multijunction design: although a monolithic tandem design has dominated the multijunction cell design space for many decades, we believe this study could represent a large shift in how we approach the design of multijunction cells. Spectrum-splitting designs that allow for radiative coupling between subcells and have back reflectors on every subcell have the potential to lead the next generations of ultra-high efficiency multijunction cells.

Chapter 6

Conclusion

The research discussed in this thesis are all part of a common theme: achieving higher solar cell efficiencies. If solar cell modules that combine realistic cell, optic, and electrical losses can achieve ultrahigh efficiencies (>50%), the levelized cost of energy (LCOE) will be significantly lowered, enabling widespread deployment of this sustainable technology. Thus, research should focus on reducing the most significant thermodynamic losses in solar conversion as we have attempted in our own pursuit of high solar conversion efficiency.

We first investigated trioctylphosphine sulfide (TOP:S) as a candidate for effective sidewall passivation of small (mm^2), thin film GaAs solar cells in Chapter 2. While small cells are attractive for cheaper and more durable modules, they have a much higher perimeter-to-active area ratio and therefore have reduced efficiencies due to the unpassivated, highly recombination-active sidewalls. By simply soaking GaAs cells in liquid TOP:S overnight, we were able to nearly eliminate this size dependent trend because of the strong passivation effect of TOP:S. We verified the passivation qualities of TOP:S through four independent experimental measurements and showed an order of magnitude decrease in surface recombination velocity. We believe this study could help enable smaller and cheaper modules and also interesting self-healing structures where upon damage, TOP:S could be released and reduce the recombination at the newly exposed edge. However, TOP:S is only one molecule in an entire class of surfactants and therefore we believe that further study of these molecules could lead to an even more optimized passivation treatment.

Then, in Chapters 3 and 4, we attempted to address the largest energetic loss in solar energy conversion by designing and prototyping a multijunction cell that could incorporate seven subcells and realistically achieve >50% efficiency. Unlike traditional multijunction designs, we created an optical architecture, the polyhedral specular reflector, that divided and concentrated the incident solar spectrum onto seven electrically independent subcells for conversion, a significantly higher number than traditional technologies. We combined realistic optical models, which included wave optical simulations of optimized coatings and ray tracing simulations that determined the photon flux to each subcell position, with realistic subcell and electrical calculations to predict the module efficiencies possible with such a device. We showed that ultrahigh efficiencies (>50%) are possible with high quality optics and prototyped a high efficiency optical design that should correspond to a module efficiency of 42%. Additionally, we discussed some routes to slightly lower (>40%) efficiencies with cheaper and fewer optical components to reduce the expected cost. Although we previously identified 50% as the ultimate goal of the study, we note that our spectrum-splitting structures should be able to produce significantly more power each year because the efficiency of electrically independent subcells is insensitive to the constantly changing incident spectrum. Therefore, we believe that future research should focus on designing and prototyping combined spectrum-splitting and concentrating optics that optimize for high efficiency and low cost manufacturing of independently connected subcells.

Finally, in Chapter 5, we investigated how controlling the radiative emission in multijunction geometries, and in particular, spectrum-splitting geometries, can lead to higher efficiencies than previously thought. In this study, we used detailed balance efficiency calculations to describe traditional multijunction geometries as well as spectrum-splitting geometries whose performance depends strongly on the optical environment and therefore the degree of radiative emission trapping and radiative coupling in the cells. We experimentally verified the theory of a spectrum-splitting system where there is no radiative coupling and observed excellent matching of data to theory. Finally, we determined the ensemble multijunction efficiencies using detailed balance calculations for all of the geometries studied. We showed that the optical environment for a spectrum-splitting geometry yields higher maximum efficiencies than the previously thought possible. We are excited by these possibilities and believe that optimization of both the incident photons and also the radiatively emitted photons can yield the next generation of ultrahigh efficiencies.

Appendix A

Optical Properties of the Coatings in the Polyhedral Specular Reflector Model

We designed all of the optical coatings (filters, antireflection coatings, etc) using OpenFilters, an open source software for creating and optimizing multilayer coatings [66]. We exported the reflectivity of each coating as a function of angle to input these as surfaces in the ray tracing simulations. The reflectivity of the filters at 45° is shown in Figure A.1. Here we describe the layer materials and thicknesses for each coating.

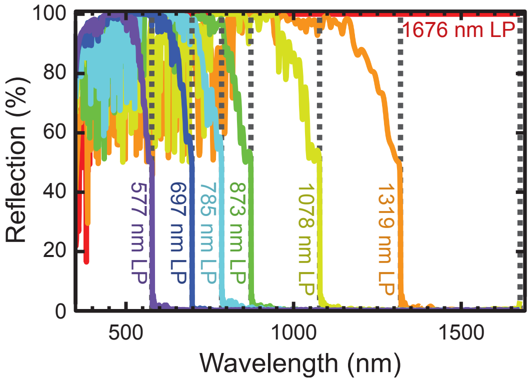

FIGURE A.1: Reflectivities of the longpass filters at 45° for the PSR design. These filters were designed using alternating layers of SiO_2 and TiO_2.

The mirrored surface for the hollow primary concentrator was assumed to have a thick (300 nm) layer of Ag capped by a thin (31 nm) layer of SiO_2 to create a broadband, highly reflective surface. Figure A.2 shows the reflectivity of this layer over some oblique angles of incidence. This coating shows >98% reflectivity for most wavelengths over these angles, which is typical of protected silver coatings.

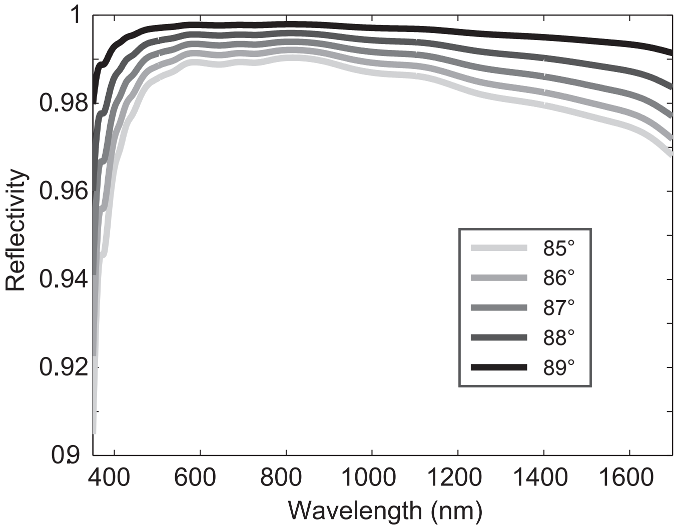

FIGURE A.2: Reflectivity of the mirrored surface for the hollow primary concentrator. The coating is composed of Ag and SiO_2 and exhibits high, broadband reflectivity for relevant angles.

We also designed an antireflection coating for the air-glass interface at the top of the solid glass prism containing the longpass filters, which was shown in Chapter 3. This coating was optimized to minimize reflection over the wavelengths of interest (350-1676 nm). The designed antireflection coating maintains very low reflection (>2%) over the wavelengths of interest for a wide range of incidence angles. The coating is composed of MgF_2, SiO_2, and very thin layers of TiO_2 and was optimized with the built-in needle optimization. The coating is 2.4 μm in total thickness with 49 layers and none of the layers are thinner than 1 nm. Figure A.3 shows the index profile of this coating.

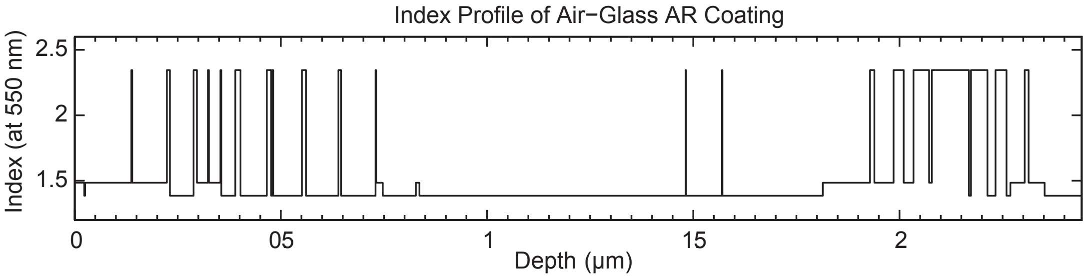

FIGURE A.3: Index profile of the air-glass antireflection coating comprising of MgF_2 (n=1.38), SiO_2 (n=1.48), and TiO_2 (n=2.34).

The seven longpass filters shown in Chapter 3.8 are composed of alternating layers of SiO_2 and TiO_2. Each filter contains hundreds of layers and is approximately 25-35 μm

Table A.1: Materials and thicknesses of the subcell antireflection coatings.

Cell Bandgap	Material	Thickness (nm)
0.74 eV	SiN	124
	TiO_2 (Rutile)	82
0.94 eV	SiN	49
	TiO_2	98
1.15 eV	SiN	17
	TiO_2	97
1.42 eV	Ta_2O_5	96
1.58 eV	SiN	103
	TiO_2 (Rutile)	94
1.78 eV	Ta_2O_5	67
2.15 eV	SiN	188

thick. None of the individual layers are thinner than 2 nm. The index profile was optimized to maximize reflectivity for photons with energies above the bandgap of the associated subcell and maximize transmission for photons with energies less than the bandgap. The index profile for each longpass filter is shown in Figure A.4.

Finally, we developed antireflection coatings for the glass-semiconductor interface between each solid glass secondary concentrator and subcell. We optimized single and dual layer antireflection coatings to minimize reflection over the designed bandwidth of conversion for each subcell. The optimized materials and thicknesses are shown in Table A.1.

Figure A.5 shows the reflectivities of each antireflection coating at two angles of incidence and the relevant subcell bandwidth for conversion (gray box). Each antireflection coating is relatively insensitive to incident angle over the designed bandwidth and with the exception of the coating for the 2.15 eV subcell, the reflectivities are $<2\%$. The reflectivities for the 2.15 eV subcell antireflection coating are much higher in the subcell band because this band is significantly larger than those of the other subcells.

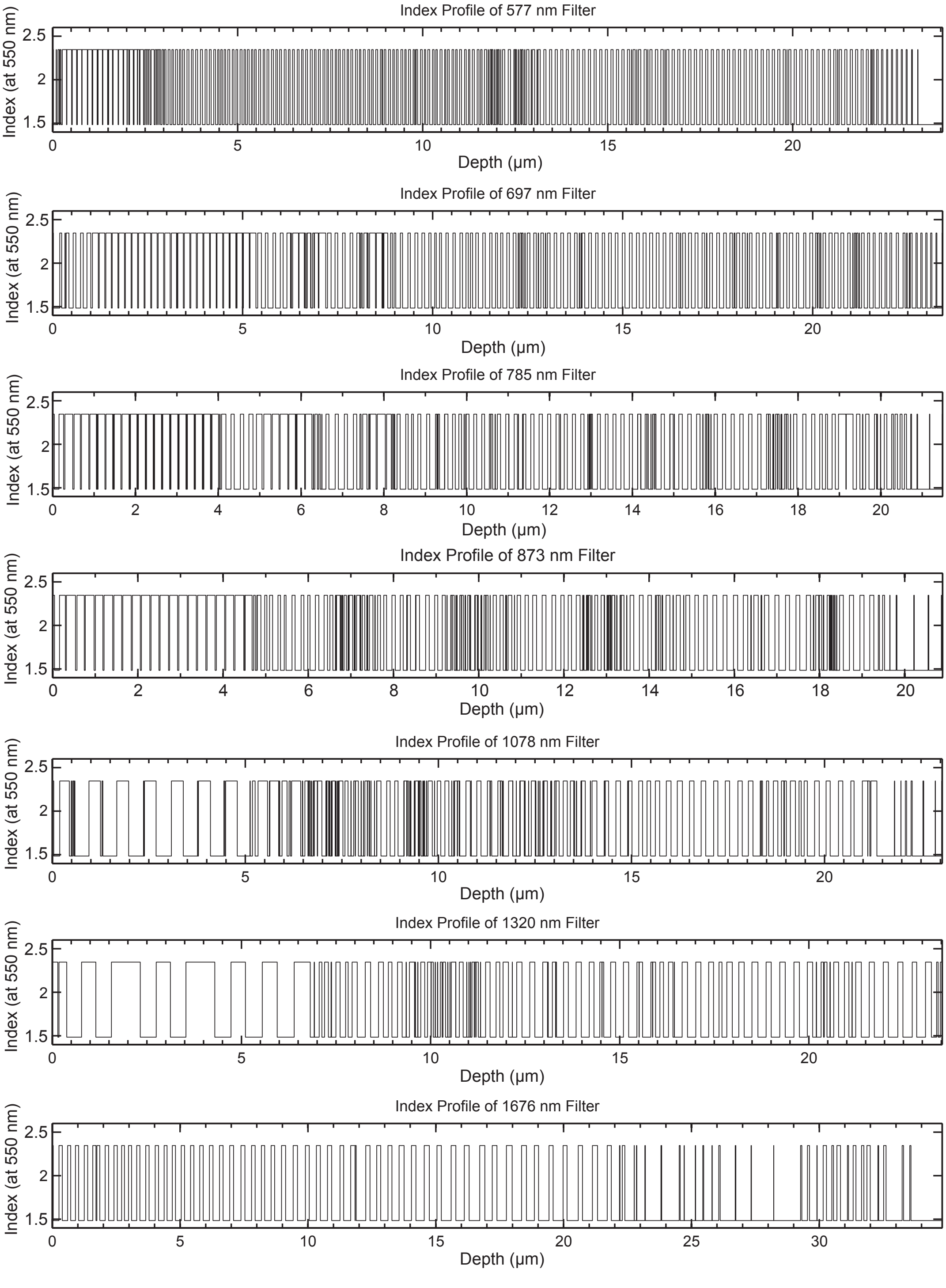

FIGURE A.4: Index profile of the seven longpass filters, comprising of SiO_2 (n=1.48) and TiO_2 (n=2.34).

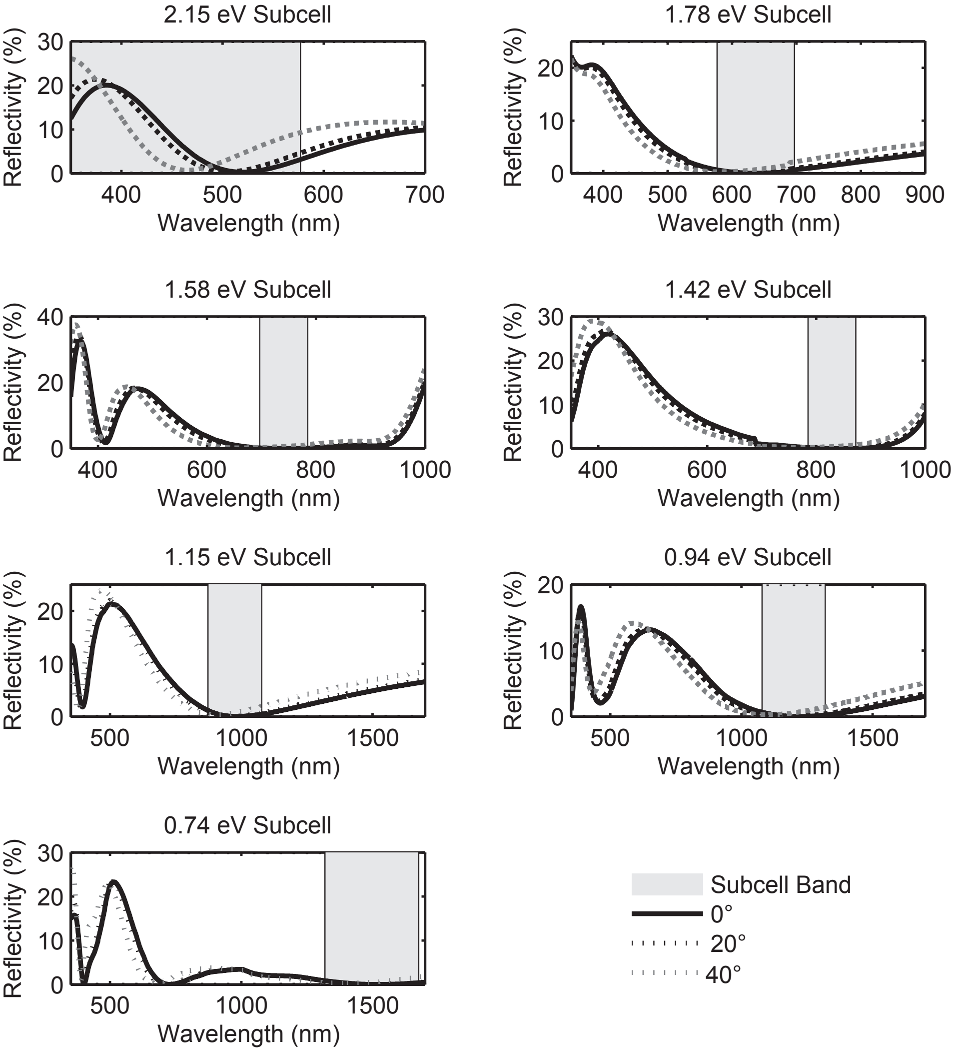

FIGURE A.5: Reflectivities of the glass-semiconductor antireflection coatings for the seven subcells. Each subcell's bandwidth for conversion is shown as a gray shaded box.

Appendix B

Ray Tracing Files and MATLAB Code for Optimizing the Concentrator Geometry of the PSR Design

This appendix describes both the ray tracing file of the polyhedral specular reflector created with the LightTools software and the MATLAB code used to open and edit the file, extract useful data from it, and calculate the efficiency for each simulated concentrator geometry.

B.1 Details of the LightTools Ray Tracing Model

Figure B.1 shows a screencapture of the polyhedral specular reflector model created in LightTools. First, we will detail the assembly of the PSR structure using the built-in CAD functions. Then, we will describe the source and receivers used for extracting the light collected at each subcell position.

Figure B.2 shows a screencapture of the optical splitting prism generated in LightTools. The opening aperture for this prism is 10 x 10 mm. We created seven thin (1 mm thick) glass parallelepipeds (45°) as surfaces for each of the filters described in Appendix A. The projection areas for these prisms are all 10 x 10 mm as defined by the input aperture.

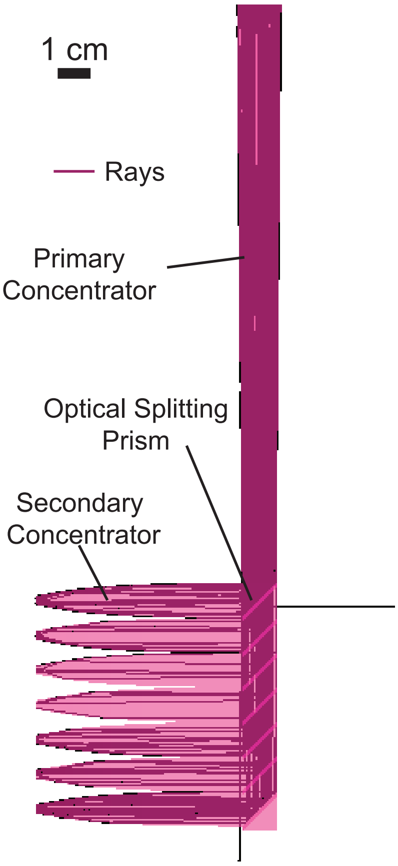

Figure B.1: Screencapture of a ray tracing simulation. The burgandy lines represent individual rays propagating through the polyhedral specular reflector.

Note that the thickness of these prisms will not matter since it will be embedded in a glass prism with identical optical properties, but the spacing between these pieces (10 mm) and the projection area for the prisms needs to be consistent with the desired geometry. The bulk material properties were set by creating a New User Material for fused silica and using Cauchy indices to describe the refractive index. Tabulated values for refractive index and absorption can also be used. The top surface of each prism is the filter surface, which is created by designating the optical coating to be from a loaded file (.opr file contains filter properties at different wavelengths and angles). The remaining surfaces should all be Smooth Optical surfaces with the Fresnel Loss setting applied (under Advanced Properties on Smooth Optical tab). Every surface, including filters and bare surfaces, in this model was assumed to have Probabilistic Ray Split (under Preferred Direction on Smooth Optical tab) to sample every ray path possible.

A large rectangular glass prism (using the same fused silica property) was generated to house the seven filters. The glass prism was 10 x 10 x 70 mm. All surfaces except for

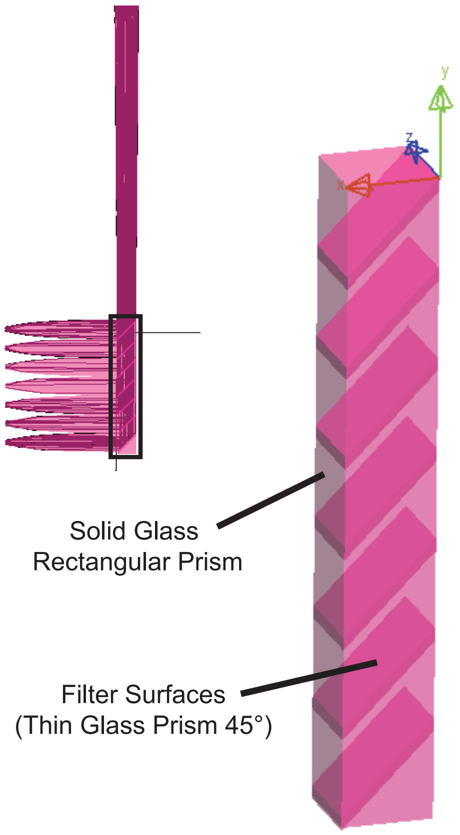

Figure B.2: Screencapture of optical splitting prism in LightTools. Thin glass pieces oriented at 45° are used as surfaces for the filters and these are embedded in a large, rectangular glass prism.

the top surface were assumed to be Smooth Optical surfaces. The top surface has the optical properties of the air-glass antireflection coating. Again, the surface is generated by loading a .opr file with angular and wavelength transmission data for the coating. Then, the seven filter prisms were embedded in the large rectangular prism by immersing the seven filters in the object under the Immersion menu.

Next, solid compound parabolic concentrators (CPCs) were added to the optical splitting prism. CPCs are located under Insert > Optical Element > CPC > Square. The CPC was oriented toward the optical splitting prism and centered on one of the seven filters. Each CPC was labeled as Conc1, Conc2, etc. starting from the top of the prism downward to make the scripting in the next section easier. The x position was made to slightly overlap with the optical splitting prism by 0.0001 mm to ensure good coupling in the model. Each CPC was then immersed in the large rectangular glass prism to simulate adhesion with an index-matched glue or the optical splitting prism and concentrators being fabricated as one monolithic piece. Each CPC input face was fixed at 10 mm (the size of the aperture) and the output face, input angle, and output angle were allowed to be free parameters in the optimization. The material was also set to be the same fused silica as used previously. The input face and concentrator sides are designated as Smooth Optical surfaces. The output face for each concentrator has the properties of the concentrator-cell antireflection coating for its designated subcell (generated with a .opr file).

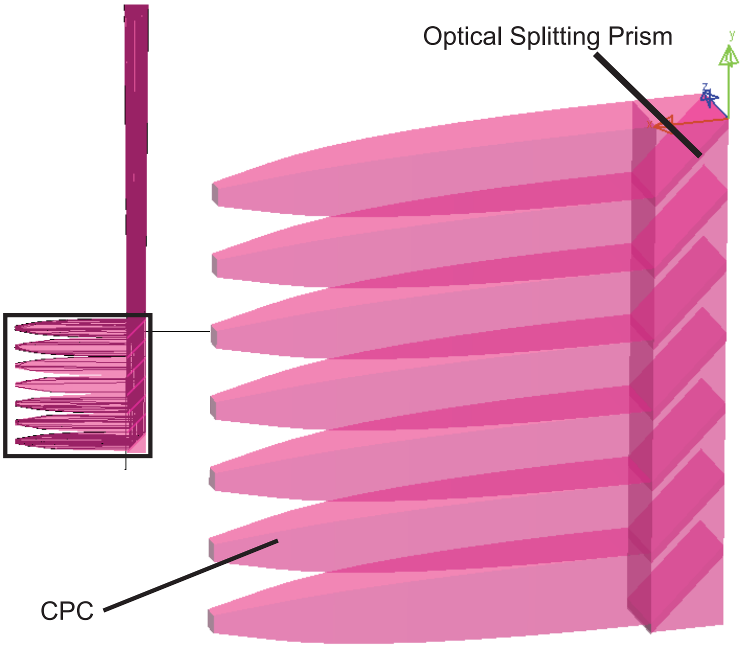

Figure B.3: Screencapture of optical splitting prism and solid CPCs in LightTools. Seven solid CPCs are aligned to the output side of the optical splitting prism and embedded in the glass prism.

Solid rectangular prisms were then added to provide a surface for a receiver that would act as the subcell. A solid prism was used in place of a dummy plane because many of the rays would be totally internally reflected if there was an air gap between the concentrator and the receiver. The size of the prism was matched to the output size of the secondary CPC and 0.01 mm thick. The subcell prism overlapped with the secondary concentrator by 0.0001 mm so that the cell can be immersed in the concentrator with which it overlaps. The face that transects the concentrator is set to Transmitting, while the opposite face, the ‘subcell,’ is set to Absorbing so that all rays terminate at this surface. The four remaining surfaces are set as perfect Mirror surfaces (R=100%) to ensure any rays that pass through the output face of the CPC are collected at the receiver. Figure **??** shows screencaptures of the subcells and receivers. All seven receivers were set to units of Radiometric Power and Define by CCT (Properties), Color Analyses were selected for both Illuminance and Intensity meshes under the Forward Simulation, the mesh sizing was made to be approximately 4 bins per mm, and under the Spectral Distribution menu, the Bin Interval was set to 1 nm, the Start Wavelength was set to 249.5 nm, and the End Wavelength was set to 1800.5 nm.

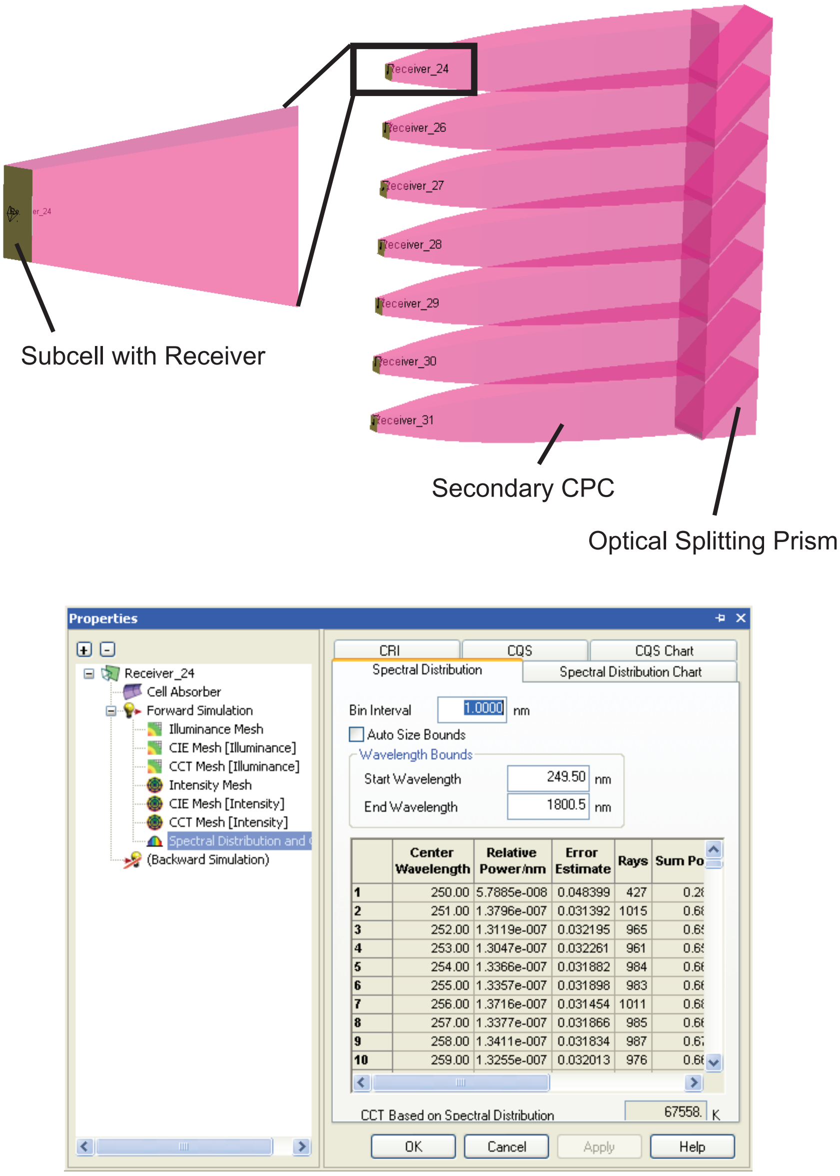

Bin Interval 1.0000 nm

☐ Auto Size Bounds

Wavelength Bounds

Start Wavelength 249.50 nm

End Wavelength 1800.5 nm

	Center Wavelength	Relative Power/nm	Error Estimate	Rays	Sum Po
1	250.00	5.7885e-008	0.048399	427	0.2
2	251.00	1.3796e-007	0.031392	1015	0.6
3	252.00	1.3119e-007	0.032195	965	0.6
4	253.00	1.3047e-007	0.032261	961	0.6
5	254.00	1.3366e-007	0.031882	984	0.6
6	255.00	1.3357e-007	0.031898	983	0.6
7	256.00	1.3716e-007	0.031454	1011	0.6
8	257.00	1.3377e-007	0.031866	985	0.6
9	258.00	1.3411e-007	0.031834	987	0.6
10	259.00	1.3255e-007	0.032013	976	0.6

CCT Based on Spectral Distribution 67558. K

Figure B.4: Screencapture of the subcell receivers in LightTools and the receiver options menu.

A hollow compound parabolic concentrator was added as the primary concentrator. In the side menu, a hollow CPC can be added by selecting Elements > Place Reflector > CPCPolygonReflector. The output size was fixed at 10 mm, the size of the optical splitting aperture, and the input angle was fixed at 1.8°, as discussed in Chapter 3. The output of the concentrator was centered on the optical splitting prism, as shown in Figure B.5. The material was set to be Aluminum, under the preset User Materials menu. However, this material is largely inconsequential as any rays transmitted through the concentrator will not be collected. The surface of the concentrator was defined to be a user coating with the SiO_2 coated Ag described in Appendix A.

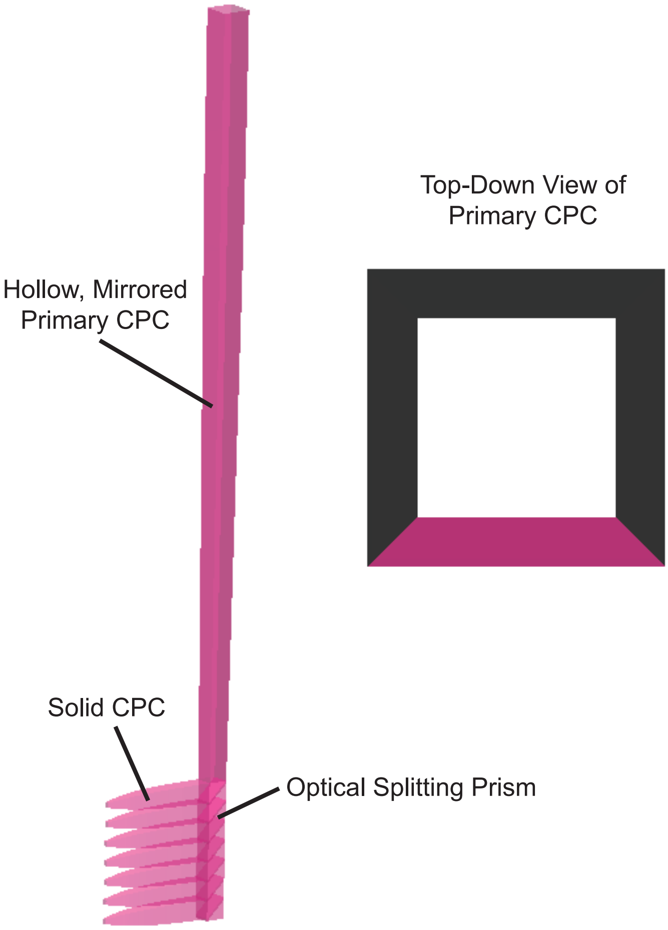

FIGURE B.5: Screencapture of optical splitting prism, solid CPCs, and primary CPC in LightTools. A hollow CPC is inserted and aligned above the optical splitting prism.

Finally, a source object was created to simulate the sun as shown in Figure B.6. A rectangular prism was inserted with the same cross section as the input to the primary concentrator. Then, the object was converted to an Object Source, with only the bottom face emitting light. The source outputs 1 Watt of Radiometric Power with a Lambertian angular distribution. The aim sphere has an Upper Angle of 0 degrees and a Lower Angle of 1.5 degrees, yielding a source with an overall divergence of 3° to account for circumsolar radiation. The source is directed toward and centered over the primary concentrator. The spectral region of the source is set to be equally weighted for all wavelengths from 280 - 1700 nm with a step of 1 nm. This ensures that all wavelengths are equally sampled for the highest accuracy. The results are later weighted by the AM1.5D spectrum. The input flux to the prototype is determined by first measuring the flux captured by a receiver on a dummy plane just below the source with all other optical components not included in the file. The Relative Power collected at each subcell position is divided by this input measurement after completion of the simulation to yield a distribution of input photons.

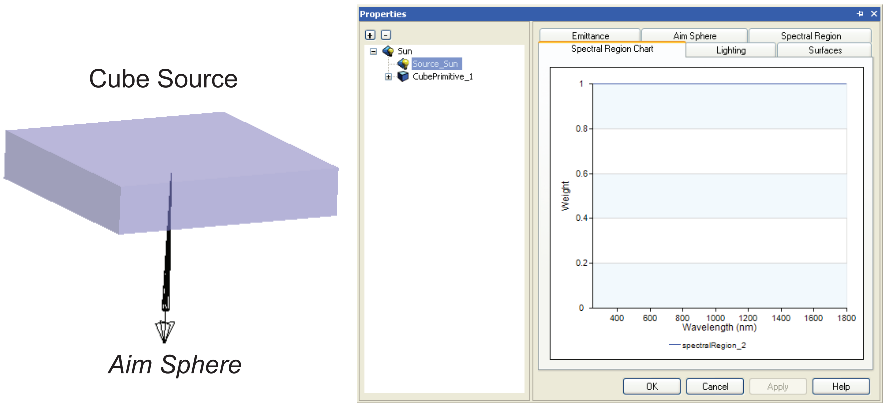

FIGURE B.6: Screencapture of source used for the PSR and Spectral Region Chart. The Spectral Region Chart shows equal weighting off all wavelengths (i.e., Weight = 1 for all wavelengths).

B.2 Details of the MATLAB Code to Change and Run the Ray Tracing Simulations

The following MATLAB code was used to optimize the concentrator geometry of the PSR design. This code opens a LightTools file which contains the PSR optical module and all of its predesigned optical coatings (Appendix A). Then, it defines the geometry for both concentrators (input angle, output angle, trimming) and runs the simulation. Then, the photon flux to each subcell position is exported and normalized by an input flux file (saved previously). The normalized files are finally fed into a modified detailed balance calculation where the file will be weighted by the AM1.5D spectrum and the contactless device efficiency for that design point is calculated. This process is iterated over many concentrator geometries until the plots in Chapter 3 are achieved.

Code that wraps around the functions and optimizes over many contact geometries:

```
% PSR: Optimizing Teacups
clear;

% Start count for number of simulations performed
count = 1;

% For all secondary CPC output angles
for jj = 3
    % For all secondary CPC input angles
    for ll = 3
        % load created file that determines scaling factor for different
        % trim lengths of the secondary concentrators
        load PSR_gen4_trimfiles_In1234_Out20253035_more.mat
        % Secondary CPC input and output angles from file
        OutputAngle = OutAngle(jj);
        InputAngle = InAngle(ll);

        % Secondary CPC size factors (length after trimming, new
        % concentration after trimming, input size for trim length to yield
        % input size of 10 mm after trimming, new output size after scaling
        HeightConcTrim = HeightConcAT{jj,ll};
        HeightConc = HeightConcBT{jj,ll};
        TrimLength = TrimLen{jj,ll};
        InSize = InputSize;
        NewOutputSize = OutputSize{jj,ll};

        % Get rid of other not needed variables
        clearvars -except ExcelTot count HeightConcTrim HeightConc TrimLength
    InSize NewOutputSize InputAngle OutputAngle jj ll;

        % Number of simulations performed
        SimNum = 3*2*3*4*1;

        % LightTools file name to load
        LTfileName = 'PSR_Gen4_real_optimize_paper_LP_trim.1';
        % File base to name after
        MatFile = 'PSR_Gen4real_trimPaper_';
        % Load saved input files
        load PSR_gen4_real_inputfile_4sizes;

        % Top CPC input angle
        InputAngleTop = 1.8;
        % Input size top (before trim)
        InputSizeTop = [30];
        % Input length after trim
        InputTrimTop = [300];

        %Cell data ordered highest to lowest
        ERE = [.0019;.08;.03;.225;.012;.016;.11];
        absorb = .92;
```

```
    % For all trim lengths of primary concentrator
    for kk = 1:length(InputTrimTop)
        % For all input sizes of primary concentrator (before trimming)
        for k = 1:length(InputSizeTop)
            % For all output angles of the secondary concentrator
            % (redundant)
            for i = 1:length(OutputAngle)
                % For all input angles of the secondary concentrator
                % (redundant)
                for j = 1:length(InputAngle)

                    % For all trim lengths of the secondary concentrators
                    for mm = 4
                        m = mm;
                        % Simulation Counter
                        sprintf('Simulation %d of %d',count,SimNum)
                        % Function that, using input data, adjusts
                        % LightTools file, runs the simulation, and
                        % extracts the data
                        [Cell1, Cell2,Cell3,Cell4,Cell5,Cell6,Cell7,ExcelFile
] = PSRdesign_opt_func(InputAngle(j),OutputAngle(i),InputAngleTop,
InputSizeTop(k),LTfileName,InSize(m),TrimLength(m),NewOutputSize(m),
InputTrimTop(kk));

                        % Strings for labeling save file
                        inStr = num2str(InputAngle(j));
                        outStr = num2str(OutputAngle(i));
                        sizeStr = num2str(InputSizeTop(k)/(10));
                        trimStr = num2str(round(HeightConcTrim(m)));
                        trimTopStr = num2str(round(InputTrimTop(kk)));
                        % Create file for saving
                        label = strcat(MatFile,sizeStr,'xtop_',trimTopStr,'
toptrim_',inStr,'in_',outStr,'out_',trimStr,'trim.mat');

                        % Function that takes in extracted data to
                        % calculate efficiency of structure
                        [ExcelFile] = PSR_dataref_funcp(ERE,absorb, Cell1,
Cell2,Cell3,Cell4,Cell5,Cell6,Cell7,Input{k,1},ExcelFile);

                        % Save data
                        save(label);

                        % Add results to running variable "ExcelTot"
                        ExcelTot(count,:) = ExcelFile;

                        % Update count
                        count = count+1;
                        % Clear extraneous variables
                        clearvars label Cell1 Cell2 Cell3 Cell4 Cell5 Cell6
Cell7 ExcelFile;
                    end
```

```
                    end
                end
            end
        end
    end
end
```

Function that opens and runs a ray tracing simulation in LightTools:

```
function [ Cell1, Cell2,Cell3,Cell4,Cell5,Cell6,Cell7,ExcelFile ] =
    PSR_opt_func_gen4_realtrim2(InputAngle,OutputAngle,InputAngleTop,InputSizeTop
    ,LTfileName,InputSize,TrimLength,NewOutSize, TopConcLength)
% Function to run and retrieve spectral files from LightTools simulation of
% PSR gen4 realistic structure with trimming of CPCs

% Connect to LightTools Server
lt=actxserver('LightTools.LTAPI');
ltml = actxserver('ltcom64.LTAPI2');

% Location of files
fileLoc='C:\Documents and Settings\Carissa\My Documents\LTUser\Carissa\Teacup\Gen
     4 Realistic Opt\';

% Open File
cmdStr=['Open "',fileLoc,LTfileName,'"'];
returnVal=ltml.LTCmd(lt,cmdStr)

% Turn off extra functions to make it run faster and turn scription option
% on
ltml.LTCmd(lt,'\VConsole');
ltml.LTCmd(lt,'\V3D');
ltml.LTSetOption(lt, 'SHOWFILEDIALOGBOX', 0);
ltml.LTSetOption(lt, 'SHOWDIALOGS', 0);
ltml.LTSetOption(lt, 'SCRIPTING', 1);

% Determine number of bins for each receiver.  Approximately 4 bins per mm
% of the output size.
approxOutsize = round(NewOutSize);
if approxOutsize < 1
    approxOutsize = 1;
end
sizeBin = round(approxOutsize*4);

%%%%%%%%%%%%%%%%%%%%%%%%%%%%%%%%%%%%
%%%%%% Adjust Secondary CPCs %%%%%%%
%%%%%%%%%%%%%%%%%%%%%%%%%%%%%%%%%%%%

 concList= ltml.LTDbList(lt, 'LENS_MANAGER[1]','CPC_PRIMITIVE');
 % For all seven secondary CPCs, adjust parameters to oversize them, move
 % the CPCs, trim the CPCs to new trimmed size.  Note: should name
 % concentrators Conc1, Conc2, Conc3, etc. for this to work.
```

```
 for i =1:7
     % Select concentrator
     [concKey,msg]=ltml.LTListNext(lt,concList);
     % Set the input size, output angle and input angle
     % Note, this oversizes the concentrator so we can trim it
     ltml.LTDbSet(lt,concKey,'OutputAngle',OutputAngle);
     ltml.LTDbSet(lt,concKey,'InputAngle',InputAngle);
     ltml.LTDbSet(lt,concKey,'InputSize',InputSize);
     % Return position of concentrator
     xpos = lt.DbGet(concKey,'X');
     % Move concentrator over so after it is trimmed, new input face will
     % already be at correct position
     xpos_new = xpos - TrimLength;
     ltml.LTDbSet(lt,concKey,'X',xpos_new);
     % Trim Concentrator by selecting concentrator and then trimming it at
     % position xpos
     trim_Str = ['Select Conc' num2str(i)];
     ltml.LTCmd(lt,trim_Str);
     x_trim = xpos;
     cmdStr = ['TrimSolid XYZ ', num2str(xpos), ',0,0 XYZ 0,0,0'];
     ltml.LTCmd(lt,cmdStr);
 end
 % Retrieve concentrator length (before trimming, same for all 7 cpcs)
 ConcHeight = lt.DbGet(concKey, 'OverallLength');
% Retrieve concentrator output size
OutputSize = lt.DbGet(concKey, 'OutputSize');


%%%%%%%%%%%%%%%%%%%%%%%%%%%%%%%%%%%%%%
%%%%%% Set Primary CPC Data %%%%%%%%%
%%%%%%%%%%%%%%%%%%%%%%%%%%%%%%%%%%%%%%

% Select next concentrator, which is the primary concentrator
[concInKey,msg]=ltml.LTListNext(lt,concList);
% Adjust input size and input angle
ltml.LTDbSet(lt,concInKey,'InputSize',InputSizeTop);
ltml.LTDbSet(lt,concInKey,'InputAngle',InputAngleTop);
% Trim top concentrator
ltml.LTCmd(lt,'Select Concentrator_21'); % In this model, concentrator labeled as
     Concentrator_21, adjust if renamed
% Set new trim height (.001 mm above top conc length because y position of
% top concentrator is 0.001
trim_height = TopConcLength + 0.001;
% Send trim command to command line
cmdStr = ['TrimSolid XYZ 0,', num2str(trim_height), ',0 XYZ 0,1000,0'];
ltml.LTCmd(lt,cmdStr);
% Retrieve new input size of primary concentrator by retrieving list of
% points of y vs. z, but for highest accuracy, first set number of points
% to maximum (5000)
ltml.LTDbSet(lt,concInKey,'NumPoints',5000);
for z = 1:5000
    conc_ptlist(z,2) = lt.DbGet(concInKey, 'ZAt',z,1);
```

```
    conc_ptlist(z,1) = lt.DbGet(concInKey, 'YAt',z,1);
end
% Interpolate from this data and find new input size
InputSizeTopNew = interp1(conc_ptlist(:,2),conc_ptlist(:,1),TopConcLength)*2;
% Retrieve output angle
OutTopAngle = lt.DbGet(concInKey, 'OutputAngle');

% Adjust the source
% Find the source box, under "cube_primative", in this model, I made the
% source before any other cubes (i.e. cells).  If not the case in your
% model, have this file step through the seven cells first before selecting
% the source box
cellList = ltml.LTDbList(lt, 'LENS_MANAGER[1]','CUBE_PRIMITIVE');
[cellKey,msg]=ltml.LTListNext(lt,cellList);
% Set length and width of box to be the new input size of the primary CPC
ltml.LTDbSet(lt,cellKey,'Length',InputSizeTopNew);
ltml.LTDbSet(lt,cellKey,'Width',InputSizeTopNew);
% Set z position so that source is centered over the primary CPC
sourceZPos = 5-(InputSizeTopNew/2);
ltml.LTDbSet(lt,cellKey,'Z',sourceZPos);
% Set y position so that it's 2 mm over the primary concentrator input
sourceYPos = TopConcLength + 2;
ltml.LTDbSet(lt,cellKey,'Y',sourceYPos);

%%%%%%%%%%%%%%%%%%%%%%%%%%%%%%%%%%%%%%%%%%%%%%%%
%%%%%% Adjust Cell Position and Sizes %%%%%%%%%%
%%%%%%%%%%%%%%%%%%%%%%%%%%%%%%%%%%%%%%%%%%%%%%%%


for i = 1:7
    % Adjust cell postition so it is at the end of the secondary CPCs
    % Find new cell position
    CellPos = ConcHeight-TrimLength+xpos+.009;
    % Move Cell
    [cellKey,msg]=ltml.LTListNext(lt,cellList);
    ltml.LTDbSet(lt,cellKey,'X',CellPos);

    % Resize Cell so it is the same size as output of CPC
    ltml.LTDbSet(lt,cellKey,'Width',OutputSize);
    ltml.LTDbSet(lt,cellKey,'Height',OutputSize);

    % Adjust receivers in cells
    % List receivers
    receiverList= ltml.LTDbList(lt, 'LENS_MANAGER[1]','SURFACE_RECEIVER');
    [RecKey,msg]=ltml.LTListNext(lt,receiverList);
    % List meshes within receiver list
    binList= ltml.LTDbList(lt, 'LENS_MANAGER[1]','Illuminance_Mesh');
    [temp,msg]=ltml.LTListNext(lt,binList);
    % adjust meshing size for both dimensions (~4 bin / mm)
    ltml.LTDbSet(lt,temp,'X_Dimension',sizeBin);
    ltml.LTDbSet(lt,temp,'Y_Dimension',sizeBin);
end
```

```
% Fill Excel file with parameters
% Top concentration = new input size^2 / (10 x 10 mm)
TopConc = InputSizeTopNew^2/(10)^2;
% Bottom concentration (10 x 10 mm) / Output size sec CPC^2
BottomConc = (10)^2/OutputSize^2;
% Overall concentration = input size primary CPC ^2 / output size secCPC^2
OverallConc = InputSizeTopNew^2/OutputSize^2;
% Height of secondary CPC after trimming
ConcHeightAT = ConcHeight- TrimLength;
% Excel file has data on primary CPC, then secondary CPC, then overall
% concentration and later will add in efficiency with perfect optics,
% actual efficiency from ray tracing, and optical efficiency
ExcelFile = [InputAngleTop, OutTopAngle, InputSizeTopNew, TopConcLength, TopConc,
     InputAngle,OutputAngle,OutputSize,ConcHeightAT,BottomConc,OverallConc];

%%%%%%%%%%%%%%%%%%%%%%%%%%%%%%%%%%%%%%%%%%%
%%%%%%%% Simulate and Retrieve Data %%%%%%%%
%%%%%%%%%%%%%%%%%%%%%%%%%%%%%%%%%%%%%%%%%%%

% Begin the simulations!
lt.Cmd('BeginAllSimulations')

% Retrieve data from receivers
% List Spectral Distributions (already opened RecKey as first receiver
% previously)
specList = ltml.LTDbList(lt, RecKey, 'SPECTRAL_DISTRIBUTION');
% Retrieve Cell 1 Data
    % Note: should probably just make Cell data (i.e. Cell1, Cell2, ...
    % into a MATLAB cell format like Subcell_Data{i,1} = Cell 1,
    % Subcell_Data{i,2} = Cell 2, ...
specKey = ltml.LTListNext(lt,specList);
for i = 1:1551
    Cell1(i,1) = lt.DbGet(specKey, 'Wavelength_At',i,1);
    Cell1(i,2) = lt.DbGet(specKey, 'Power_At',i,1);
    Cell1(i,3) = lt.DbGet(specKey, 'Error_Estimate_At',i,1);
    Cell1(i,4) = lt.DbGet(specKey, 'Number_of_Rays_At',i,1);
    Cell1(i,5) = lt.DbGet(specKey, 'Sum_Power_At',i,1);
    Cell1(i,6) = lt.DbGet(specKey, 'Variance_At',i,1);
    Cell1(i,7) = lt.DbGet(specKey, 'Flux_At',i,1);
end

% Receiver Cell 2
% Find next receiver list
[RecKey2,msg]=ltml.LTListNext(lt,receiverList);
% List spectral distribution
specList = ltml.LTDbList(lt, RecKey2, 'SPECTRAL_DISTRIBUTION');
specKey = ltml.LTListNext(lt,specList);
% Extract Data
for i = 1:1551
    Cell2(i,1) = lt.DbGet(specKey, 'Wavelength_At',i,1);
    Cell2(i,2) = lt.DbGet(specKey, 'Power_At',i,1);
```

```
    Cell2(i,3) = lt.DbGet(specKey, 'Error_Estimate_At',i,1);
    Cell2(i,4) = lt.DbGet(specKey, 'Number_of_Rays_At',i,1);
    Cell2(i,5) = lt.DbGet(specKey, 'Sum_Power_At',i,1);
    Cell2(i,6) = lt.DbGet(specKey, 'Variance_At',i,1);
    Cell2(i,7) = lt.DbGet(specKey, 'Flux_At',i,1);
end

% Receiver Cell 3
[RecKey3,msg]=ltml.LTListNext(lt,receiverList);
specList = ltml.LTDbList(lt, RecKey3, 'SPECTRAL_DISTRIBUTION');
specKey = ltml.LTListNext(lt,specList);
for i = 1:1551
    Cell3(i,1) = lt.DbGet(specKey, 'Wavelength_At',i,1);
    Cell3(i,2) = lt.DbGet(specKey, 'Power_At',i,1);
    Cell3(i,3) = lt.DbGet(specKey, 'Error_Estimate_At',i,1);
    Cell3(i,4) = lt.DbGet(specKey, 'Number_of_Rays_At',i,1);
    Cell3(i,5) = lt.DbGet(specKey, 'Sum_Power_At',i,1);
    Cell3(i,6) = lt.DbGet(specKey, 'Variance_At',i,1);
    Cell3(i,7) = lt.DbGet(specKey, 'Flux_At',i,1);
end

% Receiver Cell 4
[RecKey4,msg]=ltml.LTListNext(lt,receiverList);
specList = ltml.LTDbList(lt, RecKey4, 'SPECTRAL_DISTRIBUTION');
specKey = ltml.LTListNext(lt,specList);
for i = 1:1551
    Cell4(i,1) = lt.DbGet(specKey, 'Wavelength_At',i,1);
    Cell4(i,2) = lt.DbGet(specKey, 'Power_At',i,1);
    Cell4(i,3) = lt.DbGet(specKey, 'Error_Estimate_At',i,1);
    Cell4(i,4) = lt.DbGet(specKey, 'Number_of_Rays_At',i,1);
    Cell4(i,5) = lt.DbGet(specKey, 'Sum_Power_At',i,1);
    Cell4(i,6) = lt.DbGet(specKey, 'Variance_At',i,1);
    Cell4(i,7) = lt.DbGet(specKey, 'Flux_At',i,1);
end

% Receiver Cell 5
[RecKey5,msg]=ltml.LTListNext(lt,receiverList);
specList = ltml.LTDbList(lt, RecKey5, 'SPECTRAL_DISTRIBUTION');
specKey = ltml.LTListNext(lt,specList);
for i = 1:1551
    Cell5(i,1) = lt.DbGet(specKey, 'Wavelength_At',i,1);
    Cell5(i,2) = lt.DbGet(specKey, 'Power_At',i,1);
    Cell5(i,3) = lt.DbGet(specKey, 'Error_Estimate_At',i,1);
    Cell5(i,4) = lt.DbGet(specKey, 'Number_of_Rays_At',i,1);
    Cell5(i,5) = lt.DbGet(specKey, 'Sum_Power_At',i,1);
    Cell5(i,6) = lt.DbGet(specKey, 'Variance_At',i,1);
    Cell5(i,7) = lt.DbGet(specKey, 'Flux_At',i,1);
end

% Receiver Cell 6
[RecKey6,msg]=ltml.LTListNext(lt,receiverList);
specList = ltml.LTDbList(lt, RecKey6, 'SPECTRAL_DISTRIBUTION');
```

```
specKey = ltml.LTListNext(lt,specList);
for i = 1:1551
    Cell6(i,1) = lt.DbGet(specKey, 'Wavelength_At',i,1);
    Cell6(i,2) = lt.DbGet(specKey, 'Power_At',i,1);
    Cell6(i,3) = lt.DbGet(specKey, 'Error_Estimate_At',i,1);
    Cell6(i,4) = lt.DbGet(specKey, 'Number_of_Rays_At',i,1);
    Cell6(i,5) = lt.DbGet(specKey, 'Sum_Power_At',i,1);
    Cell6(i,6) = lt.DbGet(specKey, 'Variance_At',i,1);
    Cell6(i,7) = lt.DbGet(specKey, 'Flux_At',i,1);
end

% Receiver Cell 1
[RecKey7,msg]=ltml.LTListNext(lt,receiverList);
specList = ltml.LTDbList(lt, RecKey7, 'SPECTRAL_DISTRIBUTION');
specKey = ltml.LTListNext(lt,specList);
for i = 1:1551
    Cell7(i,1) = lt.DbGet(specKey, 'Wavelength_At',i,1);
    Cell7(i,2) = lt.DbGet(specKey, 'Power_At',i,1);
    Cell7(i,3) = lt.DbGet(specKey, 'Error_Estimate_At',i,1);
    Cell7(i,4) = lt.DbGet(specKey, 'Number_of_Rays_At',i,1);
    Cell7(i,5) = lt.DbGet(specKey, 'Sum_Power_At',i,1);
    Cell7(i,6) = lt.DbGet(specKey, 'Variance_At',i,1);
    Cell7(i,7) = lt.DbGet(specKey, 'Flux_At',i,1);
end


% Close the simulation (otherwise will run out of memory!)

returnVal=ltml.LTCmd(lt,'Close')
```

Function that processes data from ray tracing simulation to generate predicted contactless device efficiency:

```
function [ExcelFile] = PSR_dataref_funcp(ERE,absorb, Cell1, Cell2,Cell3,Cell4,
    Cell5,Cell6,Cell7,Input,ExcelFile)
% Function to take in spectral data from ray tracing simulation, weight the
% data by AM1.5D and calculate a contactless device efficiency

% load AM1.5D flux file
load E_flux_AM15D;
% Input size of primary concentrator from Excel File generated in ray
% tracing simulation
InputSize = ExcelFile(1,3);
% output size of secondary concentrator
Outsize = ExcelFile(1,8);

% Normalize and generate pardata (% of photons go where)
pardata = 1240./Input(:,1);
% Weighting by the "relative power" column of ray tracing simulation.  This
% is more accurate than rays because accounts for absorption losses, cosine
% factor, etc
```

```
pardata(:,2)= Cell1(:,2)./Input(:,2);
pardata(:,3) = Cell2(:,2)./Input(:,2);
pardata(:,4) = Cell3(:,2)./Input(:,2);
pardata(:,5) = Cell4(:,2)./Input(:,2);
pardata(:,6) = Cell5(:,2)./Input(:,2);
pardata(:,7) = Cell6(:,2)./Input(:,2);
pardata(:,8) = Cell7(:,2)./Input(:,2);

% Calculate area / concentration
% input area
conc_area = InputSize^2;
% Cell area
OutArea = Outsize^2;
cell_area = OutArea*ones(7,1);
% Concentration is input area divided by cell area
conc = conc_area./cell_area;
% Power in incident spectrum is 90 mW /cm2 * concentration
power_spec = .09*conc_area;

% bandgaps
Eg0 = 0.74;
Eg1 = 0.94;
Eg2 = 1.15;
Eg3 = 1.42;
Eg4 = 1.58;
Eg5 = 1.78;
Eg6 = 2.15;
bandgaps = [Eg0;Eg1;Eg2;Eg3;Eg4;Eg5;Eg6];
Eg =flipud(bandgaps);
lenEg = length(Eg);

% Change wavelength data of ray tracing into units of energy (eV)
E_par = flipud(pardata(:,1));
perc_par = flipud(pardata(:,2:end));
% generate actual spectra to each cell from AM15D, weight by AM1.5D
for i = 1:lenEg
    flux_adj_par(:,i) = genspec_par(E,flux,E_par,perc_par(:,i));
end

% Calculate power in each slice
for i = 1:lenEg
    % Use modified detailed balance to calculate power generated in each
    % subell with spectra from optics in ray tracing
    [slice_inc_power(i,1), speceff(i,1), cell_power(i,1), cell(:,i), Jtot, v,Jsc(
    i,1),] = indepDBpar(Eg(i),conc(i), flux_adj_par(:,i), E, ERE(i), absorb);
end

% Also calculate power generated with perfect optics for comparison
[slice_inc_power_perf, speceff_perf, cell_power_perf, cell_perf, Jtot_perf,
    v_perf] = indepDBpar(flipud(Eg),conc(1), flux, E, flipud(ERE), absorb);

% Power generated in each subcell
```

```
power_W = cell_power.*cell_area;
% Efficiency = sum of power generated in each subcell / power spectrum
tot_eff = sum(power_W)/power_spec;
% Efficiency with perfect spectrum splitting
tot_eff_perf = sum(cell_power_perf)/(.09*conc(1));

% Add to running excel file the efficiency with perfect optics, the optical
% efficency (eff with realistic optics / efficiency with perfect optics),
% and finally predicted contactless device efficiency!
ExcelAdd = [tot_eff_perf, tot_eff/tot_eff_perf, tot_eff];
ExcelFile  = [ExcelFile, ExcelAdd];
```

Appendix C

Additional Details for the High Contrast Grating Simulations

These simulations were performed in RCWA Diffract Mod. The built in optimizing function was used to vary the spacing (500, 600 nm), smaller radius (10, 20, 30, 40, and 50 nm), thickness (50-400 nm in 25 nm steps), and incident angle (0-45° in $15^{c}irc$ steps) for the dual radii structure. Some example average reflection and transmission profiles are shown below for 45° angle of incidence. In general, the bandwidth of the reflecting band increases with decreasing secondary radii and nanopillar spacing. Additionally, the bandwidth of the reflecting band does increase with increasing height, but at the cost of transmission of lower energy photons, resulting in a much more gradual filter cutoff.

There is a sharp dip near 950 nm for most of the designs. This most likely corresponds to a strong electric field enhancement between the small and large radii nanopillars and reduces the reflectivity of the structure.

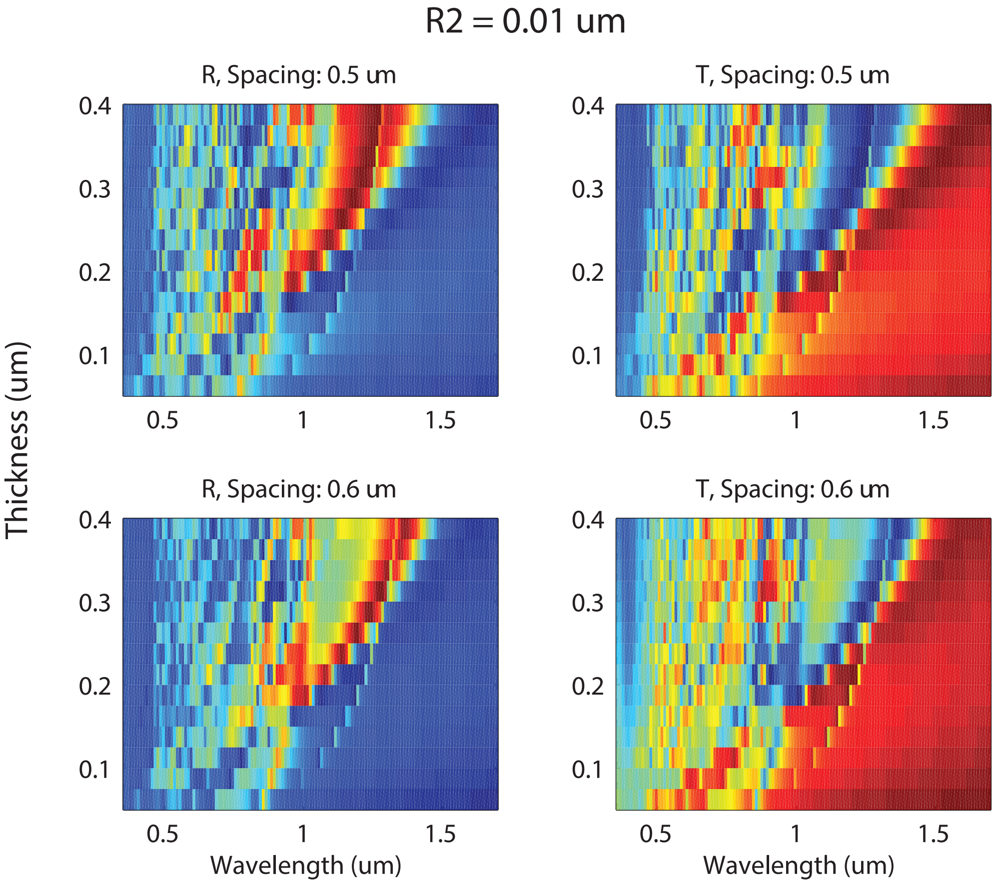

FIGURE C.1: Reflection and transmission of the dual lattice HCG filter with $R_2 = 10$ nm.

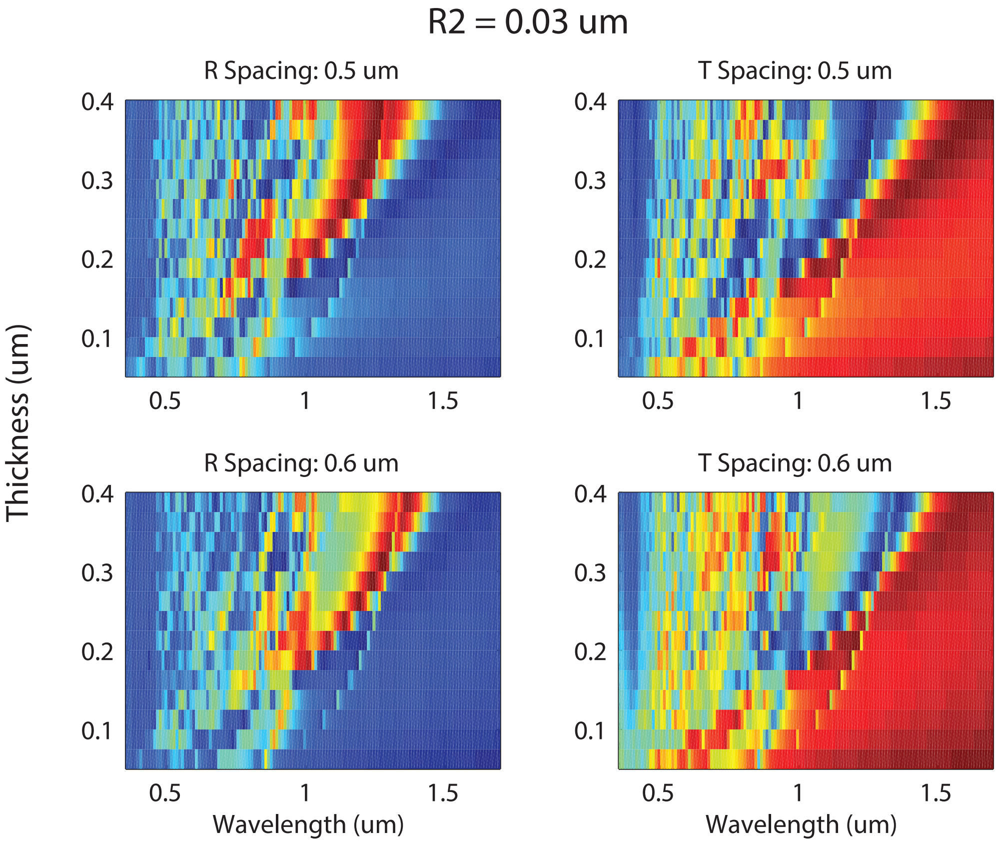

FIGURE C.2: Reflection and transmission of the dual lattice HCG filter with $R_2 = 30$ nm.

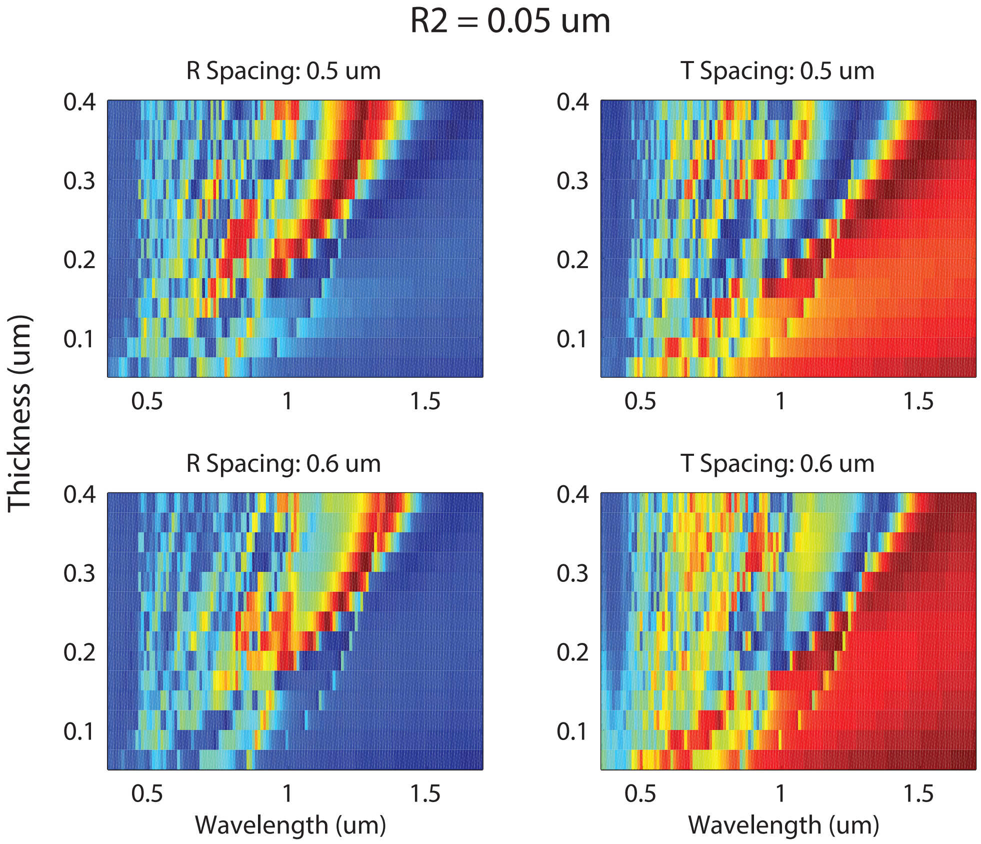

FIGURE C.3: Reflection and transmission of the dual lattice HCG filter with $R_2 = 50$ nm.

Appendix D

MATLAB Code for Calculating the Optical and Module Efficiencies of the Measured Optics

For each optical prototype, we generated a series of files from the silicon and germanium photodetectors labeled as filterxSi.csv (where x =1-7 for each subcell position) or incidentSiy (where y is the number of incident measurements). We then used the following matlab code to extract the fraction of incident light for each subcell position and calculate the optical efficiency and predicted module efficiency.

Code that wraps around the functions to extract the data and calculate the efficiency of the module:

```
%%%%%%%% Code to analyze and plot prototyping data from SARP %%%%%%%%

clear;
%%%%%%%%%%%%%%%%%%%%%%%%%%%%%%%%%%%%%%%%%%
%%%%%%%%%%%%%%% Input Data %%%%%%%%%%%%%%%
%%%%%%%%%%%%%%%%%%%%%%%%%%%%%%%%%%%%%%%%%%

% Concentration (x)
conc = 100;
% Folder containing data
folder = '2015 09 24 - PSR and LP\';
% Which incidents to average over
for ii = 1:7
```

```
    inc_avg_Si{ii,1} = [1;2];
    inc_avg_Ge{ii,1} = [1;2;3];
end
% Did you use PDMS to couple output to detector (1 = yes, 0 = no)
PDMS_corr = 1;
% Do you need Fresnel corrections (i.e. measuring on bare glass)
% (0 = no, 1 = 1 Fresnel correction, 2 = 2 fresnel corrections)
% Note: need 1 or 2 if looking at bare filter splitting prism, only 1
% needed if using AR coating
Fresnel_noCorr = 1;
% Do you want Fresnel corrections added to the plot? (1=yes, 0=no)
Fresnel_Plot = 0;

% Bandgaps and EREs of cells to model (currently set at target)
% Ordered highest to lowest bandgap
Eg = [2.15;1.78;1.58;1.42;1.15;.94;.74];
ERE = [.0019;.08;.03;.225;.012;.016;.11];

%%%%%%%%%%%%%%%%%%%%%%%%%%%%%%%%%%%%%%%%%%
%%%%%%%%%%%%%%% Load Data %%%%%%%%%%%%%%%%
%%%%%%%%%%%%%%%%%%%%%%%%%%%%%%%%%%%%%%%%%%

% Spectral Data
load E_flux_AM15D
% only go from 400 to 1680
wave = flipud(1240./E);
flux = flipud(flux);
wave_start = 400;
wave_end = 1680;
ind_start = find(wave>=wave_start,1,’first’);
ind_end = find(wave>=wave_end,1,’first’);
wave_exp = wave(ind_start:ind_end);
flux_exp = flux(ind_start:ind_end);
waveF = 400:5:1700.’; % Currently using 5 nm steps


% Glass Data
load Corning_7980_data
% Column 1, 1 reflection, Column 2, 2 reflections off of glass
refl_int(:,1) = interp1(glass_data(:,1),glass_data(:,4),waveF);
refl_int(:,2) = interp1(glass_data(:,1),glass_data(:,3),waveF);
glass_refl(:,1) = interp1(glass_data(:,1),glass_data(:,4),wave_exp);
glass_refl(:,2) = interp1(glass_data(:,1),glass_data(:,3),wave_exp);

% PDMS Data (to normalize detector-to-pdms coupling)
load PDMS_fittingdata;

% Detector Factor (detector slightly smaller than 1 x 1 cm)
detector_factor = .99*.99;

%%%%%%%%%%%%%%%%%%%%%%%%%%%%%%%%%%%%%%%%%%%%
%%%%%%%%%%%%%%% Extract Files %%%%%%%%%%%%%%
```

```
%%%%%%%%%%%%%%%%%%%%%%%%%%%%%%%%%%%%%%%%%%%%

%%%%%%%%%% EXTRACT SI DETECTOR DATA
% write function to extract data, give cell of normalized filter data
[waveF,filter_R,filtRefCSi,filtRefCGe] = PSR_prototype_filtersplit_extract_LP(
    folder, inc_avg_Si, inc_avg_Ge,Si_PDMS_fit, Ge_PDMS_fit);
% normalize by detector factor
filter_R = filter_R*detector_factor;



% bandgaps and eres
wave_bandstart = 1240./Eg;
wave_band = [400;wave_bandstart(1:6)];

% Color
cc = hsv(8);
cc = flipud(cc);

%%%%%%%%%%%%%%%%%%%%%%%%%%%%%%%%%%%%%%%%%%%%
%%%%%%%%%%%%%%%%% Plot Data %%%%%%%%%%%%%%%%
%%%%%%%%%%%%%%%%%%%%%%%%%%%%%%%%%%%%%%%%%%%%
for i = 1:7
    % PLOT #1
    % plot each cell spectrum on its own axis, No Fresnel
    %corrections included but could easily add them in if desired
    FigHandle = figure(1);
    set(FigHandle, 'Position', [0, 0, 600, 700]);
    subplot(7,1,i);
    figure(1);
    hold on;
    % Plot filter multiplied by filter correction necessary
    if PDMS_corr > 0
        pdms_corr = refl_int(:,1);
    else
        pdms_corr = ones(length(waveF),1);
    end

    % Filter plot has Fresnel corrections
    if Fresnel_Plot == 1 && Fresnel_noCorr > 0
        fresnel_corr = refl_int(:,Fresnel_noCorr);
    else
        fresnel_corr = ones(length(waveF),1);
    end

    % Plot data, corrected for PDMS coupling (concentrators), but no
    % Fresnel corrections (if looking at bare filter structure)
    plot(waveF,pdms_corr.*filter_R(:,i)./fresnel_corr,'color',cc(i+1,:),'
    LineWidth',2);
    % Plot bandgap to show where cutoff should be
    plot([ wave_band(i) wave_band(i)], [1 0], 'color', [.5 .5 .5], 'LineStyle', '
    :','LineWidth',2);
    axis([400 1700 0 1]);
```

```
% If last plot, label x axis
if i>6
    hXLabel = xlabel('Wavelength (nm)');
    set([hXLabel]  , ...
    'FontSize'   , 16);
else
    set(gca,...
        'XTickLabel','')
end
% If middle plot (subcell #4), label y axis
if i>3 && i<5
    hYLabel = ylabel('Reflection');
    set([hYLabel]  , ...
    'FontSize'   , 16);
end
% Set plotting preferences
set(gca, ...
    'Box'         , 'on'     , ...
    'TickDir'     , 'in'     , ...
    'XColor'      , [0 0 0], ...
    'YColor'      , [0 0 0], ...
    'LineWidth'   , 1.3         );
set(gca,'Color',[1,1,1])
set( gca                       , ...
    'FontSize'   , 14 );
% Label each box with subcell #
label_filter = ['Subcell #' num2str(i)];
htext = text(920,.7,label_filter);
set(htext, 'FontSize', 14);

% PLOT #2
% plot each cell spectrum on same plot
figure(2);
hold on;
% Plot fraction incident light at each subcell, currently no fresnel
% corrections
plot(waveF,pdms_corr.*filter_R(:,i)./fresnel_corr,'color',cc(i+1,:),'
LineWidth',2.5);
axis([400 1700 0 1]);
xlabel('Wavelength (nm)');
ylabel('Fraction Incident Light');

% Legend
legendtext{i,1} = [num2str(Eg(i)) ' eV cell position'];

% Plotting preferences
set(gca, ...
    'Box'         , 'on'     , ...
    'TickDir'     , 'in'     , ...
    'XColor'      , [0 0 0], ...
    'YColor'      , [0 0 0], ...
```

```
        'LineWidth'   , 1.3         );
    set(gca,'Color',[1,1,1])
    set( gca                       , ...
        'FontSize'   , 14 );


%%%%%%%%%%%%%%%%%%%%%%%%%%%%%%%%%%%%%%%%%%%%
%%%%% Calculate Opt Splitting Eff Data %%%%%
%%%%%%%%%%%%%%%%%%%%%%%%%%%%%%%%%%%%%%%%%%%%

    % create new variable, trans_meas, of fraction incident light at each
    % subcell that has the same wavelength step as the AM1.5D file
    trans_meas(:,i) = interp1(waveF,filter_R(:,i).*pdms_corr,wave_exp);
    % flux at each subcell is just flux of AM1.5D times trans_meas
    flux_cell(:,i) = flux_exp.*trans_meas(:,i);
    % Fresnel_noCorr
    if Fresnel_noCorr == 1
          flux_cell_R(:,i) = flux_exp.*trans_meas(:,i)./glass_refl(:,1);
    end
    if Fresnel_noCorr == 2
        flux_cell_R(:,i) = flux_exp.*trans_meas(:,i)./glass_refl(:,2);
    end

    % Calculate power produced in each subcell (no Fresnel corr)
    [slice_inc_power, speceff, cell_power(i,1), cell, Jtot, v] = indepDBpar(Eg(i)
    , conc, flipud(flux_cell(:,i)), flipud(1240./wave_exp), ERE(i), .92);
    % Calculate power produced in each subcell with Fresnel corr
    if Fresnel_noCorr > 0
        [slice_inc_power_R, speceff_R, cell_power_R(i,1), cell_R, Jtot_R, v_R] =
    indepDBpar(Eg(i), conc, flipud(flux_cell_R(:,i)), flipud(1240./wave_exp), ERE
    (i), .92);
    end
end

% Calculate efficiency for a system with perfect optics
[slice_inc_powerp, speceffp, cell_powerp, cellp, Jtotp, vp] = indepDB(flipud(Eg),
    conc*ones(7,1), flipud([flux_exp]), flipud(1240./wave_exp), flipud(ERE), .92)
    ;
perf_eff = sum(cell_powerp)/(conc*.09);

% Total cell power and efficiency (no Fresnel)
cell_powerTOT = sum(cell_power);
cell_eff = cell_powerTOT./(.09*conc) % note: contactless device eff
% Optical eff = cell eff predicted / cell eff perfect
OPT_EFF = cell_eff/perf_eff


% Total cell power and efficiency (with Fresnel corr)
if Fresnel_noCorr > 0
        cell_powerTOT_R = sum(cell_power_R);
        cell_eff_R = cell_powerTOT_R/(conc*.09) % note: contactless device eff
    % Optical eff = cell eff predicted / cell eff perfect
```

```
        OPT_EFF_R = cell_eff_R/perf_eff
end
```

Function that opens and extracts the data from the source files:

```
function [wave,filter_R,filtRefCSi,filtRefCGe] =
    PSR_prototype_filtersplit_extract_LP(folder, inc_avg_Si, inc_avg_Ge,
    Si_fitting_data, Ge_fitting_data)

% function to extract SARP data from .csv files and normalize to incident
% measurements.  Returns filter reflection as well as extracted reference
% spectra data.

for j=1:7
    for i = 1:length(inc_avg_Si{j,1})
        filename = [folder 'incidentSi' num2str(inc_avg_Si{j,1}(i,1)) '.csv'];
        incidentSi{j,1}(:,:,i) = csvread(filename,5);
    end

    incSiavg(:,j) = sum(incidentSi{j,1}(:,2,:),3)/length(inc_avg_Si{j,1});
    increfSiavg(:,j) = sum(incidentSi{j,1}(:,3,:),3)/length(inc_avg_Si{j,1});

    for i = 1:length(inc_avg_Ge{j,1})
        filename = [folder 'incidentGe' num2str(inc_avg_Ge{j,1}(i,1)) '.csv'];
        incidentGe{j,1}(:,:,i) = csvread(filename,5);
    end

    incGeavg(:,j) = sum(incidentGe{j,1}(:,2,:),3)/length(inc_avg_Ge{j,1});
    increfGeavg(:,j) = sum(incidentGe{j,1}(:,3,:),3)/length(inc_avg_Ge{j,1});
end
waveSi = incidentSi{1}(:,1,1);
waveGe = incidentGe{1}(:,1,1);
% find where spectra overlap
 ind1 = find(waveSi==880);
 ind1Ge = find(waveGe==880);
 ind2 = find(waveGe==waveSi(end));
 wave = [waveSi;waveGe(ind2+1:end)];

cc = hsv(7); cc=flipud(cc);

for i = 1:7
    filenameGe = [folder 'filter' num2str(i) '_Ge.csv'];
    filenameSi = [folder 'filter' num2str(i) '_Si.csv'];
    filterRawSi(:,:,i) = csvread(filenameSi,5);
    filterRawGe(:,:,i) = csvread(filenameGe,5);

    % Calculate reference corrections
    filtRefCSi(:,i) = filterRawSi(:,3,i)./increfSiavg(:,i);
    filtRefCGe(:,i) = filterRawGe(:,3,i)./increfGeavg(:,i);
    filtRefCGe(ind2:end,i) = 1;
    % calculate reflection with referenc correction
```

```
    reflectionSi(:,i) = filterRawSi(:,2,i)./(incSiavg(:,i).*filtRefCSi(:,i).*
    Si_fitting_data);
    reflectionGe(:,i) = filterRawGe(:,2,i)./(incGeavg(:,i).*filtRefCGe(:,i).*
    Ge_fitting_data);

end

% average data
reflection = reflectionSi(1:(ind1-1),:);
reflection = [reflection;(reflectionSi(ind1:end,:)+reflectionGe(ind1Ge:ind2,:))
    /2];
reflection = [reflection; reflectionGe(ind2+1:end,:)];
filter_R = reflection;
```

Detailed balance calculation function:

```
% Function giving the detailed balance efficiency for spectral splitting
% ensembles.  These cells are independently connected and not constrained
% to current matching.

% Inputs are cell band gaps, Eg (vector ordered lowest to highest);
% concentration, C; incident spectrum in photon flux/cm2-s-eV and
% corresponding eV (lowest to highest), flux and E; external radiative
% efficiency, ERE; and percent collected current, absorb

% Outputs are spectral power incident on each cell, power; spectral
% efficiency of each cell, speceff; power converted by each cell, detbal;
% cell Voc, Jsc and fill factor, cell; and J-V data for each cell, Jtot and
% v


function [slice_inc_power, speceff, cell_power, cell, Jtot, v] = indepDBpar(Eg,C,
     flux, E, ERE, absorb)
%function [cell_power] = indepDBpar(Eg,C, flux, E, ERE, absorb)
%Constants
hbar=1.05457148e-34; %m2kg/s
c=299792458; %m/s
k=1.3806503e-23; % m2kg/s2K
T=300; %K
q=1.60217646e-19; %C
kT=k*T/q;
% etendu accounts for optical environment of cell via top and bottom index
% values and geometric factor.  Here the top index is 1 for air and bottom
% index is 3.6 for semiconductor substrate.
nitop1=1;
nibottom1=0;
etendue1=pi*nitop1^2+pi*nibottom1^2;

power = zeros(length(Eg),1);
speceff = zeros(length(Eg),1);
```

```
Egmaxv = [Eg; max(E)];
number = 1000;  % No difference in 4 places with 1000 vs 10000

specindex = zeros(length(Eg),2);
Gen = zeros(length(Eg),1);

% Calculated absorption of photons in each cell (all photons above bandgap
% and below next cell band gap considered perfectly absorbed)

for l=1:length(Eg)
    Egg = Egmaxv(l);
    Etop = Egmaxv(l+1);
    n = length(flux(E<=Egg));
    nn = length(flux(E<=Etop));
    if n==nn
        nn = n+1;
    end
    NNgen = C*trapz(E(n:nn),flux(n:nn));
    % calculates generation in split spectrum
    Gen(l) = NNgen;
    PP_gen = C*trapz(E(n:nn),flux(n:nn).*E(n:nn));
    power(l,1) = q*PP_gen;
    dP_inc = NNgen*E(n+1);
    speceff(l,1) = dP_inc/PP_gen;
    specindex(l,1) = n;
    specindex(l,2) = nn;
end
slice_inc_power = power;

% Calculate radiative emmision from cell at different operating voltages.

v=zeros(number,length(Eg));
x=zeros(number,length(Eg));
N=zeros(number,length(Eg));                        % N is in units of eV^3
J0=N; Jtot=N; Pn=N;

cell = zeros(length(Eg),4);
for l=1:length(Eg)
    Egg = Egmaxv(l);
    bias1=linspace(0,(Egg-0.0001),number);
    v(:,l) = bias1';
    %x1=linspace(Egg,Egg+1,number);
    x1=logspace(log10(Egg),log10(Egg+10),number);
    x(:,l) = x1';
    for i=1:length(bias1)
        N(i,l)=trapz(x(:,l),x(:,l).^2./(exp(x(:,l)/kT)-1)-x(:,l).^2./(exp((x(:,l)
    -v(i,l))/kT)-1));
    end
    % combine radiative and generated currents, accounting for ERE and
    % imperfect absorption/collection
    Nrad=(q^3*N(:,l).*etendue1.*q./(4*pi^3*hbar^3*c^2*100^2)); %A/cm^2
    J0(:,l) = Nrad./ERE;
```

```
    Jtot(:,l)=q*absorb*Gen(l)+J0(:,l);
    Pn(:,l) = Jtot(:,l).*v(:,l);
    zer = find(Jtot(:,l)<=0,1,'first');
%      cell(l,1) = v(zer,l);
%      cell(l,2) = Jtot(1,l);
%      cell(l,4) = J0(zer,l);
end

maxpn = max(Pn);
cell_power = maxpn';
cell(:,3) = maxpn'./(cell(:,1).*cell(:,2));



% No need to mesh or spline currents when calculating independently
% connected cells
```

Appendix E

MATLAB Code for Calculating the Efficiency of Each of the Designs in Chapter 5

The following MATLAB functions were developed to calculate the power, current, and voltage for each subcell in the geometries described in Chapter 5.

This function calculates the efficiency of the B cases. B is varied by multiplying the radinplus variable, which represents the radiated photons directed to the subcell from the next highest bandgap.

```
function [maxpower,maxcur,maxvol,rad_out] = Eff_MaxPwr_Bcase(Eg,Eg_plus,
    radin_plus,C)

% Function to calculate max power point for two subcell theory case
% discussed in EES paper by Eisler, et. al. (2014).  This describes a
% nonspecific spectrum-splitting structure where each subcell has its own
% back reflector and possibly some radiative coupling.  The input to this
% function takes the radiation from the next highest bandgap subcell and
% can be modified for different values of B by multiplying it by a factor
% between 0 and 1.

% Input
% Eg - bandgap of current subcell
% Eg_plus - bandgap of next highest bandgap subcell
% radin_plus - radiative emission from next highest bandgap subcell
% C - concentration

% Output
% maxpower - maximum power point of current subcell
```

```
% maxcur - current at maximum power point
% maxvol - voltage at maximum power point
% rad_out - radiative emission from current bandgap subcell

%%%%%%%%%%%%%%%%%%%%%%%%%%%%%%%%%%%%%%
%%%%%% Constants and Formatting %%%%%%%
%%%%%%%%%%%%%%%%%%%%%%%%%%%%%%%%%%%%%%
load E_flux_AM15D; % load AM1.5D flux file, energy (eV) and flux (1/(cm2eVs))
format long; % formatting #'s
c2=(2.99792458e10)^2; % speed of light squared, cm2/s2
plc3 = (4.135665e-15)^3; % Planck's constant^3 (eV-s)^3
kb1=1.3806503e-23; % Boltzmann's constant (J / K)
elec=1.60217733e-19; % electron charge (C)
kb2=kb1/elec; %Boltzmann's constant in eV / K
Ts = 6000; % Sun temperature (K)
To=300; %Cell temperature (K)
kTo = kb2*To; % thermal energy of cell eV
power_cons = (2*pi*elec/(plc3*c2)); % Radiative prefactor for cell emission (C/(
    eV3 cm2 s))
carnot = (1-To/Ts); % Max Carnot eff

%%%%%%%%%%%%%%%%%%%%%%%%%%%%%%%%%%%%%%%
%%% Setting Up Numerical Integration %%%
%%%%%%%%%%%%%%%%%%%%%%%%%%%%%%%%%%%%%%%

count = 0; % count # of times performed calculation
VocReg = Eg*carnot; % max Voc for cases we are considering (C<Cmax)
vgen = linspace(0,VocReg,1000); % numerical calculation of many values of voltage
vs = flipud(vgen.'); % Create vector from max voltage to 0
LEV = length(vs); % length of vs

ind_E = find(E>=Eg,1,'first'); % determine beginning of cell absorption band
ind_Eplus = find(E<=Eg_plus,1,'last'); % end of cell absorption band

% Calculate Jsc from spectral width of sun (delta)
sun1 = trapz(E(ind_E:ind_Eplus),flux(ind_E:ind_Eplus))*elec*C;
% Calculate current from previous cell
cell1 = radin_plus;

% Create empty vectors for current, power, and radiation out
Current = zeros(LEV,1);
Power = zeros(LEV,1);
radout = zeros(LEV,1);

% Create vector of energy values to integrate over (Eg -> "infinity")
% Note: Eg + 2eV was tested as the minimum value to give the same answer as
%        Eg + 10eV ("infinity")
Es_int = linspace(Eg,Eg+2,100000).';

% Calculate power produced for each voltage
for jj = 1:LEV
    % Cell radiation (integral part)
```

```
    radout(jj,1) = trapz(Es_int, Es_int.^2./(exp((Es_int-vs(jj))/kTo)-1));
    % Total current = current from sun + current from cell above - current
    % from radiative recombination
    Current(jj,1) = sun1+power_cons*(cell1-radout(jj,1));
    % Power = Current * Voltage
    Power(jj,1) = Current(jj,1)*vs(jj);

    % Try to determine max power point before having to calculate power for
    % every voltage point
    if jj > 1
        % Determine slope around power point just calculated
        slope_test = Power(jj,1) - Power(jj-1,1);
        % If previous point more efficient, remember this point, break the
        % code and go to next step to further refine to a more precise
        % voltage
        if slope_test < 0
            index = jj;
            if jj < 3
                ind_sub = 1;
            else
                ind_sub = 2;
            end
            break
        end
    end

    % If reach end of code and haven't hit max point, assume max point is
    % last voltage point
    if jj == LEV
        index = jj;
        ind_sub = 2;
    end
end

% Create new vector of voltages to sweep over, this time right around Vmax
% from previous optimization
vgen_new = flipud(linspace(vs(index),vs(index-ind_sub),1000).');
LEVn = length(vgen_new); % length of voltage vector

% Create empty vectors for current, power, and radiation out
Current_new = zeros(LEVn,1);
Power_new = zeros(LEVn,1);

% Calculate power produced for each voltage (new voltage vector)
for ii = 1:LEVn
    radout_new = trapz(Es_int, Es_int.^2./(exp((Es_int-vgen_new(ii))/kTo)-1));
    Current_new(ii,1) = sun1+power_cons*(cell1-radout_new);
    Power_new(ii,1) = Current_new(ii,1)*vgen_new(ii);

    if ii > 1
        slope_test = Power_new(ii,1) - Power_new(ii-1,1);
        % If previous point more efficient, remember this point, break the
```

```
        % code and go to next step to further refine to a more precise
        % voltage
        if slope_test < 0
            index2 = ii;
            if ii < 3
                ind_sub2 = 1;
            else
                ind_sub2 = 2;
            end
            break;
        end
    end

    if ii == LEVn
        index2 = ii;
        ind_sub2 = 2;
    end
end

% Repeat process one more time to further refine max power point
vgen_new2 = linspace(vgen_new(index2-ind_sub2),vgen_new(index2),5000);
LEVn2 = length(vgen_new2);

Power_new2 = zeros(LEVn2,1);
Current_new2 = zeros(LEVn2,1);
radout_new2 = zeros(LEVn2,1);

% Calculate power produced for each voltage (new voltage vector)
for iii = 1:LEVn2
    radout_new2(iii,1) = trapz(Es_int, Es_int.^2./(exp((Es_int-vgen_new2(iii))/
    kTo)-1));
    Current_new2(iii,1) = sun1+power_cons*(cell1-radout_new2(iii,1));
    Power_new2(iii,1) = Current_new2(iii,1)*vgen_new2(iii);

    if iii > 1
        slope_test2 = Power_new2(iii,1) - Power_new2(iii-1,1);
        if slope_test2 < 0
            count = count+1;
            % Only break when at least 10 points away from maximum
            if count >10
                break
            end
        end
    end

end

%%%%%%%%%%%%%%%%%%%%%%%%%%%%%%%%%%%%%%%
%%%%%%%% Find Max Power Point %%%%%%%%%
%%%%%%%%%%%%%%%%%%%%%%%%%%%%%%%%%%%%%%%

% Find max power point from last calculation
```

```
[value, ind] = max(Power_new2);
% Output max power point, current at max power point, voltage at max power
% point, and radiation out at max power point
maxpower = value;
maxcur = Current_new2(ind,1);
maxvol = vgen_new2(ind);
rad_out = radout_new2(ind);
```

This function calculates the efficiency and power for the selective reflector case.

```
function [maxpower,maxcur,maxvol,rad_out] = Eff_MaxPwr_SelectiveReflector(Eg,
    Eg_plus,C)

% Function to calculate max power point for selective reflector geometry.
% Each subcell is on a selective reflector that reflects all photons
% between Eg and Eg_plus.

% Input
% Eg - bandgap of current subcell
% Eg_plus - bandgap of next highest bandgap subcell
% C - concentration

% Output
% maxpower - maximum power point of current subcell
% maxcur - current at maximum power point
% maxvol - voltage at maximum power point
% rad_out - radiative emission from current bandgap subcell

%%%%%%%%%%%%%%%%%%%%%%%%%%%%%%%%%%%%%%
%%%%%% Constants and Formatting %%%%%%
%%%%%%%%%%%%%%%%%%%%%%%%%%%%%%%%%%%%%%
load E_flux_AM15D; % load AM1.5D flux file, energy (eV) and flux (1/(cm2 eV s))
format long; % formatting #'s
c2=(2.99792458e10)^2; % speed of light squared, cm2/s2
plc3 = (4.135665e-15)^3; % Planck's constant^3 (eV-s)^3
kb1=1.3806503e-23; % Boltzmann's constant (J / K)
elec=1.60217733e-19; % electron charge (C)
kb2=kb1/elec; %Boltzmann's constant in eV / K
Ts = 6000; % Sun temperature (K)
To=300; %Cell temperature (K)
kTo = kb2*To; % thermal energy of cell eV
power_cons = (2*pi*elec/(plc3*c2)); % Radiative prefactor for cell emission (C/(
    eV3 cm2 s))
carnot = (1-To/Ts); % Max Carnot eff

%%%%%%%%%%%%%%%%%%%%%%%%%%%%%%%%%%%%%%%
%%% Setting Up Numerical Integration %%%
%%%%%%%%%%%%%%%%%%%%%%%%%%%%%%%%%%%%%%%

count = 0; % count # of times performed calculation
VocReg = Eg*carnot; % max Voc for cases we are considering (C<Cmax)
```

```
vgen = linspace(0,VocReg,1000); % numerical calculation of many values of voltage
vs = flipud(vgen.'); % Create vector from max voltage to 0
LEV = length(vs); % length of vs

ind_E = find(E>=Eg,1,'first'); % determine beginning of cell absorption band
ind_Eplus = find(E<=Eg_plus,1,'last'); % end of cell absorption band


% Calculate Jsc from spectral width of sun (delta)
sun1 = trapz(E(ind_E:ind_Eplus),flux(ind_E:ind_Eplus))*elec*C;

% Create empty vectors for current, power, and radiation out
Current = zeros(LEV,1);
Power = zeros(LEV,1);
radout = zeros(LEV,1);

% Create vector of energy values to integrate over (Eg -> Eg_plus) because
% selective reflector, only radiate photons between Eg and Eg_plus
Es_int = linspace(Eg,Eg_plus,100000).';

% Calculate power produced for each voltage
for jj = 1:LEV
    % Cell radiation (integral part)
    radout(jj,1) = trapz(Es_int, Es_int.^2./(exp((Es_int-vs(jj))/kTo)-1));
    % Total current = current from sun + current from cell above - current
    % from radiative recombination
    Current(jj,1) = sun1-(power_cons*radout(jj,1));
    % Power = Current * Voltage
    Power(jj,1) = Current(jj,1)*vs(jj);

    % Try to determine max power point before having to calculate power for
    % every voltage point
    if jj > 1
        % Determine slope around power point just calculated
        slope_test = Power(jj,1) - Power(jj-1,1);
        % If previous point more efficient, remember this point, break the
        % code and go to next step to further refine to a more precise
        % voltage
        if slope_test < 0
            index = jj;
            if jj < 3
                ind_sub = 1;
            else
                ind_sub = 2;
            end
            break
        end
    end

    % If reach end of code and haven't hit max point, assume max point is
    % last voltage point
    if jj == LEV
```

```
        index = jj;
        ind_sub = 2;
    end
end

% Create new vector of voltages to sweep over, this time right around Vmax
% from previous optimization
vgen_new = flipud(linspace(vs(index),vs(index-ind_sub),1000).');
LEVn = length(vgen_new); % length of voltage vector

% Create empty vectors for current, power, and radiation out
Current_new = zeros(LEVn,1);
Power_new = zeros(LEVn,1);

% Repeat same process to further narrow down max power point
for ii = 1:LEVn
    radout_new = trapz(Es_int, Es_int.^2./(exp((Es_int-vgen_new(ii))/kTo)-1));
    Current_new(ii,1) = sun1 - (power_cons*radout_new);
    Power_new(ii,1) = Current_new(ii,1)*vgen_new(ii);
    if ii > 1
        slope_test = Power_new(ii,1) - Power_new(ii-1,1);
        if slope_test < 0
            index2 = ii;
            if ii < 3
                ind_sub2 = 1;
            else
                ind_sub2 = 2;
            end
            break;
        end
    end

    if ii == LEVn
        index2 = ii;
        ind_sub2 = 2;
    end
end

% Repeat process one more time to further refine max power point
vgen_new2 = linspace(vgen_new(index2-ind_sub2),vgen_new(index2),5000);
LEVn2 = length(vgen_new2);

Power_new2 = zeros(LEVn2,1);
Current_new2 = zeros(LEVn2,1);
radout_new2 = zeros(LEVn2,1);

% Calculate power produced for each voltage (new voltage vector)
for iii = 1:LEVn2
    radout_new2(iii,1) = trapz(Es_int, Es_int.^2./(exp((Es_int-vgen_new2(iii))/
    kTo)-1));
    Current_new2(iii,1) = sun1 - (power_cons*radout_new2(iii,1));
    Power_new2(iii,1) = Current_new2(iii,1)*vgen_new2(iii);
```

```
    if iii > 1
        slope_test2 = Power_new2(iii,1) - Power_new2(iii-1,1);
        if slope_test2 < 0
            count = count+1;

            if count >10
                break
            end
        end
    end
end

[value, ind] = max(Power_new2);
maxpower = value;
maxcur = Current_new2(ind,1);
maxvol = vgen_new2(ind);
rad_out = radout_new2(ind);
```

This function calculates the efficiency and power for the air gap tandem stack case.

```
function [maxpower,maxcur,maxvol,rad_out] = Eff_MaxPwr_AirGapTandem(Eg,Eg_plus,
    radin_plus,C)

% Function to calculate max power point for air gap tandem stack.  Light is
% emitted from both faces of the cell (4pi) and 50% of photons are
% downshifted.

% Input
% Eg - bandgap of current subcell
% Eg_plus - bandgap of next highest bandgap subcell
% radin_plus - radiative emission from next highest bandgap subcell
% C - concentration

% Output
% maxpower - maximum power point of current subcell
% maxcur - current at maximum power point
% maxvol - voltage at maximum power point
% rad_out - radiative emission from current bandgap subcell

%%%%%%%%%%%%%%%%%%%%%%%%%%%%%%%%%%%%%%%
%%%%%% Constants and Formatting %%%%%%%
%%%%%%%%%%%%%%%%%%%%%%%%%%%%%%%%%%%%%%%
load E_flux_AM15D; % load AM1.5D flux file, energy (eV) and flux (1/(cm2eVs))
format long; % formatting #'s
c2=(2.99792458e10)^2; % speed of light squared, cm2/s2
plc3 = (4.135665e-15)^3; % Planck's constant^3 (eV-s)^3
kb1=1.3806503e-23; % Boltzmann's constant (J / K)
elec=1.60217733e-19; % electron charge (C)
kb2=kb1/elec; %Boltzmann's constant in eV / K
Ts = 6000; % Sun temperature (K)
To=300; %Cell temperature (K)
```

```
kTo = kb2*To; % thermal energy of cell eV
power_cons = (2*pi*elec/(plc3*c2)); % Radiative prefactor for cell emission (C/(
    eV3 cm2 s))
carnot = (1-To/Ts); % Max Carnot eff

%%%%%%%%%%%%%%%%%%%%%%%%%%%%%%%%%%%%%%%%
%%% Setting Up Numerical Integration %%%
%%%%%%%%%%%%%%%%%%%%%%%%%%%%%%%%%%%%%%%%

count = 0; % count # of times performed calculation
VocReg = Eg*carnot; % max Voc for cases we are considering (C<Cmax)
vgen = linspace(0,VocReg,1000); % numerical calculation of many values of voltage
vs = flipud(vgen.'); % Create vector from max voltage to 0
LEV = length(vs); % length of vs

ind_E = find(E>=Eg,1,'first'); % determine beginning of cell absorption band
ind_Eplus = find(E<=Eg_plus,1,'last'); % end of cell absorption band

% Calculate Jsc from spectral width of sun (delta)
sun1 = trapz(E(ind_E:ind_Eplus),flux(ind_E:ind_Eplus))*elec*C;
% Calculate current from previous cell
cell1 = radin_plus;

% Create empty vectors for current, power, and radiation out
Current = zeros(LEV,1);
Power = zeros(LEV,1);
radout = zeros(LEV,1);
% Create vector of energy values to integrate over (Eg -> "infinity")
% Note: Eg + 2eV was tested as the minimum value to give the same answer as
%       Eg + 10eV ("infinity")
Es_int = linspace(Eg,Eg+2,100000).';

% Calculate power produced for each voltage
for jj = 1:LEV
    % Cell radiation (integral part)
    radout(jj,1) = trapz(Es_int, Es_int.^2./(exp((Es_int-vs(jj))/kTo)-1));
    % Total current = current from sun + current from cell above - current
    % from radiative recombination
    % Note: have to multiply radout by 2 since radiative prefactor for air
    % gap tandem stack should be 4 pi not 2 pi
    Current(jj,1) = sun1+power_cons*(cell1-(2*radout(jj,1)));
    % Power = Current * Voltage
    Power(jj,1) = Current(jj,1)*vs(jj);

    % Try to determine max power point before having to calculate power for
    % every voltage point
    if jj > 1
        % Determine slope around power point just calculated
        slope_test = Power(jj,1) - Power(jj-1,1);
        % If previous point more efficient, remember this point, break the
        % code and go to next step to further refine to a more precise
        % voltage
```

```
        if slope_test < 0
            index = jj;
            if jj < 3
                ind_sub = 1;
            else
                ind_sub = 2;
            end
            break
        end
    end
    % If reach end of code and haven't hit max point, assume max point is
    % last voltage point
    if jj == LEV
        index = jj;
        ind_sub = 2;
    end
end

% Create new vector of voltages to sweep over, this time right around Vmax
% from previous optimization
vgen_new = flipud(linspace(vs(index),vs(index-ind_sub),1000).');
LEVn = length(vgen_new);
% Create empty vectors for current, power, and radiation out
Current_new = zeros(LEVn,1);
Power_new = zeros(LEVn,1);

% Calculate power produced for each voltage (new voltage vector)
for ii = 1:LEVn
    radout_new = trapz(Es_int, Es_int.^2./(exp((Es_int-vgen_new(ii))/kTo)-1));
    Current_new(ii,1) = sun1+power_cons*(cell1-(2*radout_new));
    Power_new(ii,1) = Current_new(ii,1)*vgen_new(ii);
    if ii > 1
        slope_test = Power_new(ii,1) - Power_new(ii-1,1);

        if slope_test < 0
            index2 = ii;
            if ii < 3
                ind_sub2 = 1;
            else
                ind_sub2 = 2;
            end
            break;
        end
    end

    if ii == LEVn
        index2 = ii;
        ind_sub2 = 2;
    end

end
```

```
% Repeat process one more time to further refine max power point
vgen_new2 = linspace(vgen_new(index2-ind_sub2),vgen_new(index2),5000);
LEVn2 = length(vgen_new2);
Power_new2 = zeros(LEVn2,1);
Current_new2 = zeros(LEVn2,1);
radout_new2 = zeros(LEVn2,1);
% Calculate power produced for each voltage (new voltage vector)
for iii = 1:LEVn2
    radout_new2(iii,1) = trapz(Es_int, Es_int.^2./(exp((Es_int-vgen_new2(iii))/
    kTo)-1));
    Current_new2(iii,1) = sun1+power_cons*(cell1-(2*radout_new2(iii,1)));
%     Current(jj,1) = power_cons*(sun1-radout);
    Power_new2(iii,1) = Current_new2(iii,1)*vgen_new2(iii);
    if iii > 1
        slope_test2 = Power_new2(iii,1) - Power_new2(iii-1,1);

        if slope_test2 < 0
            count = count+1;

            if count >10
                break
            end
        end
    end

end

%%%%%%%%%%%%%%%%%%%%%%%%%%%%%%%%%%%%%%%
%%%%%%%% Find Max Power Point %%%%%%%%%
%%%%%%%%%%%%%%%%%%%%%%%%%%%%%%%%%%%%%%%

% Find max power point from last calculation
[value, ind] = max(Power_new2);
% Output max power point, current at max power point, voltage at max power
% point, and radiation out at max power point
maxpower = value;
maxcur = Current_new2(ind,1);
maxvol = vgen_new2(ind);
rad_out = 2*radout_new2(ind);
```

This function calculates the efficiency and power for the traditional tandem stack case.

```
function [maxpower,maxcur,maxvol,rad_up,rad_down] = Eff_MaxPwr_TraditionalTandem(
    Eg,Eg_plus,radin_plus,C,ntop,nbot,theta_top,theta_bot)

% Function to calculate max power point for a traditional tandem stack
% multijunction cell.  Subcells are optically in contact with another so
% the radiative emission will be higher than other geometries and the
% amount of downshifting will be higher too.

% Input
```

```
% Eg - bandgap of current subcell
% Eg_plus - bandgap of next highest bandgap subcell
% radin_plus - radiative emission from next highest bandgap subcell
% C - concentration
% n_top - index above cell (n=1 for the cases we look at)
% n_bot - index of subcell (n=3.5 for the cases we are looking at)
% theta_top - escape cone between subcell and air
% theta_bot - escape cone between subcell and another subcell (index
% matched so 90deg)

% Output
% maxpower - maximum power point of current subcell
% maxcur - current at maximum power point
% maxvol - voltage at maximum power point
% rad_up - radiative emission from current bandgap directed upward to next
%          highest bandgap subcell
% rad_down - radiative emission from current bandgap directed dpwnward to
%            next lowest bandgap subcell

%%%%%%%%%%%%%%%%%%%%%%%%%%%%%%%%%%%%%%%
%%%%%% Constants and Formatting %%%%%%%
%%%%%%%%%%%%%%%%%%%%%%%%%%%%%%%%%%%%%%%
load E_flux_AM15D; % load AM1.5D flux file, energy (eV) and flux (1/(cm2eVs))
format long; % formatting #'s
c2=(2.99792458e10)^2; % speed of light squared, cm2/s2
plc3 = (4.135665e-15)^3; % Planck's constant^3 (eV-s)^3
kb1=1.3806503e-23; % Boltzmann's constant (J / K)
elec=1.60217733e-19; % electron charge (C)
kb2=kb1/elec; %Boltzmann's constant in eV / K
Ts = 6000; % Sun temperature (K)
To=300; %Cell temperature (K)
kTo = kb2*To; % thermal energy of cell eV
power_cons = (2*pi*elec/(plc3*c2)); % Radiative prefactor for cell emission (C/(
    eV3 cm2 s))
carnot = (1-To/Ts); % Max Carnot eff
% Etendue
etendue = pi*(ntop^2*sind(theta_top)^2 + nbot^2*sind(theta_bot)^2);

%%%%%%%%%%%%%%%%%%%%%%%%%%%%%%%%%%%%%%%%
%%% Setting Up Numerical Integration %%%
%%%%%%%%%%%%%%%%%%%%%%%%%%%%%%%%%%%%%%%%

count = 0; % count # of times performed calculation
VocReg = Eg*carnot; % max Voc for cases we are considering (C<Cmax)
vgen = linspace(0,VocReg,1000); % numerical calculation of many values of voltage
vs = flipud(vgen.'); % Create vector from max voltage to 0
LEV = length(vs); % length of vs

ind_E = find(E>=Eg,1,'first'); % determine beginning of cell absorption band
ind_Eplus = find(E<=Eg_plus,1,'last'); % end of cell absorption band

% Calculate Jsc from spectral width of sun (delta)
```

```
sun1 = trapz(E(ind_E:ind_Eplus),flux(ind_E:ind_Eplus))*elec*C;
% Calculate current from previous cell
cell1 = radin_plus;

% Create empty vectors for current, power, and radiation out
Current = zeros(LEV,1);
Power = zeros(LEV,1);
radout = zeros(LEV,1);
% Create vector of energy values to integrate over (Eg -> "infinity")
% Note: Eg + 2eV was tested as the minimum value to give the same answer as
%       Eg + 10eV ("infinity")
Es_int = linspace(Eg,Eg+2,100000).';

% Calculate power produced for each voltage
for jj = 1:LEV
    % Cell radiation (integral part)
    radout(jj,1) = trapz(Es_int, Es_int.^2./(exp((Es_int-vs(jj))/kTo)-1));
    % Total current = current from sun + current from cell above - current
    % from radiative recombination
    % Etendue modifies total amount of radiated photons
    Current(jj,1) = sun1+power_cons*(cell1-(etendue*radout(jj,1)));
    % Power = Current * Voltage
    Power(jj,1) = Current(jj,1)*vs(jj);

    % Try to determine max power point before having to calculate power for
    % every voltage point
    if jj > 1
        % Determine slope around power point just calculated
        slope_test = Power(jj,1) - Power(jj-1,1);
         % If previous point more efficient, remember this point, break the
        % code and go to next step to further refine to a more precise
        % voltage
        if slope_test < 0
            index = jj;
            if jj < 3
                ind_sub = 1;
            else
                ind_sub = 2;
            end
            break
        end
    end

     % If reach end of code and haven't hit max point, assume max point is
    % last voltage point
    if jj == LEV
        index = jj;
        ind_sub = 2;
    end
end

% Create new vector of voltages to sweep over, this time right around Vmax
```

```
% from previous optimization
vgen_new = flipud(linspace(vs(index),vs(index-ind_sub),1000).');
LEVn = length(vgen_new);
% Create empty vectors for current, power, and radiation out
Current_new = zeros(LEVn,1);
Power_new = zeros(LEVn,1);
% Calculate power produced for each voltage (new voltage vector)
for ii = 1:LEVn
    radout_new = trapz(Es_int, Es_int.^2./(exp((Es_int-vgen_new(ii))/kTo)-1));
    Current_new(ii,1) = sun1+power_cons*(cell1-(etendue*radout_new));
    Power_new(ii,1) = Current_new(ii,1)*vgen_new(ii);
    if ii > 1
        slope_test = Power_new(ii,1) - Power_new(ii-1,1);
        if slope_test < 0
            index2 = ii;
            if ii < 3
                ind_sub2 = 1;
            else
                ind_sub2 = 2;
            end
            break;
        end
    end
    if ii == LEVn
        index2 = ii;
        ind_sub2 = 2;
    end
end

% Repeat process one more time to further refine max power point
vgen_new2 = linspace(vgen_new(index2-ind_sub2),vgen_new(index2),5000);
LEVn2 = length(vgen_new2);

Power_new2 = zeros(LEVn2,1);
Current_new2 = zeros(LEVn2,1);
radout_new2 = zeros(LEVn2,1);

% Calculate power produced for each voltage (new voltage vector)
for iii = 1:LEVn2
    radout_new2(iii,1) = trapz(Es_int, Es_int.^2./(exp((Es_int-vgen_new2(iii))/
    kTo)-1));
    Current_new2(iii,1) = sun1+power_cons*(cell1-(etendue*radout_new2(iii,1)));
    Power_new2(iii,1) = Current_new2(iii,1)*vgen_new2(iii);
    if iii > 1
        slope_test2 = Power_new2(iii,1) - Power_new2(iii-1,1);
        if slope_test2 < 0
            count = count+1;

            if count >10
                break
            end
        end
```

```
    end
end

%%%%%%%%%%%%%%%%%%%%%%%%%%%%%%%%%%%%%%%
%%%%%%%% Find Max Power Point %%%%%%%%%
%%%%%%%%%%%%%%%%%%%%%%%%%%%%%%%%%%%%%%%

% Find max power point from last calculation
[value, ind] = max(Power_new2);
% Output max power point, current at max power point, voltage at max power
% point, and radiation out at max power point
maxpower = value;
maxcur = Current_new2(ind,1);
maxvol = vgen_new2(ind);
rad_up = (pi*ntop^2*sind(theta_top)^2/etendue)*etendue*radout_new2(ind);
rad_down = (pi*nbot^2*sind(theta_bot)^2/etendue)*etendue*radout_new2(ind);
```

This function calculates the efficiency and power for the polyhedral specular reflector.

```
function [maxpower,maxcur,maxvol,rad_out,rad_down] = Eff_MaxPwr_PSRcase(Eg,
    Eg_plus,radin_plus,C,PercRecycle,PercDownshift)

% Function to calculate max power point for PSR case discussed in EES paper
% (Eisler, et. al., 2014).  Each subcell is on its own back reflector.
% There is some radiative coupling (PercDownshift) and some photons are
% reflected back onto the same subcell (PercRecycle).

% Input
% Eg - bandgap of current subcell
% Eg_plus - bandgap of next highest bandgap subcell
% radin_plus - radiative emission from next highest bandgap subcell
% C - concentration
% PercDownshift - fraction of photons downshifted to next lowest bandgap
% subcell
% PercRecycle - fraction of photons reflected back onto the same subcell

% Output
% maxpower - maximum power point of current subcell
% maxcur - current at maximum power point
% maxvol - voltage at maximum power point
% rad_out - radiative emission from current bandgap subcell
% rad_down - radiative emission from current subcell * PercDownshift

%%%%%%%%%%%%%%%%%%%%%%%%%%%%%%%%%%%%%%%
%%%%%% Constants and Formatting %%%%%%%
%%%%%%%%%%%%%%%%%%%%%%%%%%%%%%%%%%%%%%%
load E_flux_AM15D; % load AM1.5D flux file, energy (eV) and flux (1/(cm2eVs))
format long; % formatting #'s
c2=(2.99792458e10)^2; % speed of light squared, cm2/s2
plc3 = (4.135665e-15)^3; % Planck's constant^3 (eV-s)^3
kb1=1.3806503e-23; % Boltzmann's constant (J / K)
```

```
elec=1.60217733e-19; % electron charge (C)
kb2=kb1/elec; %Boltzmann's constant in eV / K
Ts = 6000; % Sun temperature (K)
To=300; %Cell temperature (K)
kTo = kb2*To; % thermal energy of cell eV
power_cons = (2*pi*elec/(plc3*c2)); % Radiative prefactor for cell emission (C/(
    eV3 cm2 s))
carnot = (1-To/Ts); % Max Carnot eff

%%%%%%%%%%%%%%%%%%%%%%%%%%%%%%%%%%%%%%%
%%% Setting Up Numerical Integration %%%
%%%%%%%%%%%%%%%%%%%%%%%%%%%%%%%%%%%%%%%
count = 0; % count # of times performed calculation
VocReg = Eg*carnot; % max Voc for cases we are considering (C<Cmax)
vgen = linspace(0,VocReg,1000); % numerical calculation of many values of voltage
vs = flipud(vgen.'); % Create vector from max voltage to 0
LEV = length(vs); % length of vs

ind_E = find(E>=Eg,1,'first'); % determine beginning of cell absorption band
ind_Eplus = find(E<=Eg_plus,1,'last'); % end of cell absorption band

% Calculate Jsc from spectral width of sun (delta)
sun1 = trapz(E(ind_E:ind_Eplus),flux(ind_E:ind_Eplus))*elec*C;
% Calculate current from previous cell
cell1 = radin_plus;

% Create empty vectors for current, power, and radiation out
Current = zeros(LEV,1);
Power = zeros(LEV,1);
radout = zeros(LEV,1);

% Create vector of energy values to integrate over (Eg -> "infinity")
% Note: Eg + 2eV was tested as the minimum value to give the same answer as
%       Eg + 10eV ("infinity")
Es_int = linspace(Eg,Eg+2,100000).';

% Calculate power produced for each voltage
for jj = 1:LEV
    % Cell radiation (integral part)
    radout(jj,1) = trapz(Es_int, Es_int.^2./(exp((Es_int-vs(jj))/kTo)-1));
    % Total current = current from sun + current from cell above - current
    % from radiative recombination
    % note: radout reduced because some photons recycled onto same subcell
    Current(jj,1) = sun1+power_cons*(cell1-(1-PercRecycle)*radout(jj,1));
    % Power = Current * Voltage
    Power(jj,1) = Current(jj,1)*vs(jj);

    % Try to determine max power point before having to calculate power for
    % every voltage point
    if jj > 1
        % Determine slope around power point just calculated
        slope_test = Power(jj,1) - Power(jj-1,1);
```

```
        % If previous point more efficient, remember this point, break the
        % code and go to next step to further refine to a more precise
        % voltage
        if slope_test < 0
            index = jj;
            if jj < 3
                ind_sub = 1;
            else
                ind_sub = 2;
            end
            break
        end
    end

    % If reach end of code and haven't hit max point, assume max point is
    % last voltage point
    if jj == LEV
        index = jj;
        ind_sub = 2;
    end
end

% Create new vector of voltages to sweep over, this time right around Vmax
% from previous optimization
vgen_new = flipud(linspace(vs(index),vs(index-ind_sub),1000).');
LEVn = length(vgen_new);
% Create empty vectors for current, power, and radiation out
Current_new = zeros(LEVn,1);
Power_new = zeros(LEVn,1);
% Calculate power produced for each voltage (new voltage vector)
for ii = 1:LEVn
    radout_new = trapz(Es_int, Es_int.^2./(exp((Es_int-vgen_new(ii))/kTo)-1));
    Current_new(ii,1) = sun1+power_cons*(cell1-(1-PercRecycle)*radout_new);
    Power_new(ii,1) = Current_new(ii,1)*vgen_new(ii);
    if ii > 1
        slope_test = Power_new(ii,1) - Power_new(ii-1,1);

        if slope_test < 0
            index2 = ii;
            if ii < 3
                ind_sub2 = 1;
            else
                ind_sub2 = 2;
            end
            break;
        end
    end

    if ii == LEVn
        index2 = ii;
        ind_sub2 = 2;
    end
```

```
end

% Repeat process one more time to further refine max power point
vgen_new2 = linspace(vgen_new(index2-ind_sub2),vgen_new(index2),5000);
LEVn2 = length(vgen_new2);

Power_new2 = zeros(LEVn2,1);
Current_new2 = zeros(LEVn2,1);
radout_new2 = zeros(LEVn2,1);
% Calculate power produced for each voltage (new voltage vector)
for iii = 1:LEVn2
    radout_new2(iii,1) = trapz(Es_int, Es_int.^2./(exp((Es_int-vgen_new2(iii))/
    kTo)-1));
    Current_new2(iii,1) = sun1+power_cons*(cell1-(1-PercRecycle)*radout_new2(iii
    ,1));
    Power_new2(iii,1) = Current_new2(iii,1)*vgen_new2(iii);
    if iii > 1
        slope_test2 = Power_new2(iii,1) - Power_new2(iii-1,1);
        if slope_test2 < 0
            count = count+1;
            if count >10
                break
            end
        end
    end
end

%%%%%%%%%%%%%%%%%%%%%%%%%%%%%%%%%%%%%%%
%%%%%%%% Find Max Power Point %%%%%%%%%
%%%%%%%%%%%%%%%%%%%%%%%%%%%%%%%%%%%%%%%

% Find max power point from last calculation
[value, ind] = max(Power_new2);
% Output max power point, current at max power point, voltage at max power
% point, and radiation out at max power point
maxpower = value;
maxcur = Current_new2(ind,1);
maxvol = vgen_new2(ind);
rad_out = (1-PercRecycle)*radout_new2(ind);
rad_down = PercDownshift*rad_out;
```

Appendix F

Calculating Concentration, Radiative Coupling, and Light Trapping for the PSR

A schematic of the polyhedral specular reflector is shown in Figure F.1. The first subcell always covers the full aperture opening to have photons encounter each subcell in order from highest to lowest bandgap, otherwise the spectrum will not be split properly. In Chapter 5, the subcells are arranged at a 45° angle. For a subcell length of L, the aperture of the multijunction cell is L/$\sqrt{2}$. This geometry will determine both the concentration on each subcell and the final destination of the radiatively emitted photons. For a 45° PSR, the concentration factor is $1/\sqrt{2}$, the ratio of the subcell to the input aperture.

To determine the fraction of photons reflected back into the same subcell (RB_n) and the fraction of photons downshifted to the next bandgap (B_n), the destination of each photon as a function of angle is determined as a function of position and this is averaged over the length of the subcell (L). For the example photons shown in Figure 1s, emitted photons occupying the angles of the blue cone (θ_1 to θ_1') will be reflected back into the same subcell and represent RB_n. The emitted photons occupying the green cone (θ_1 to θ_2) will be reflected to the next subcell and represent B_n. These cones will change as a function of position, so we determine the average angle occupancy as a function of x. Then we integrate that expression over the length of the cell, normalizing by L, as outlined below for calculating the fraction of photons reflected back into the same subcell.

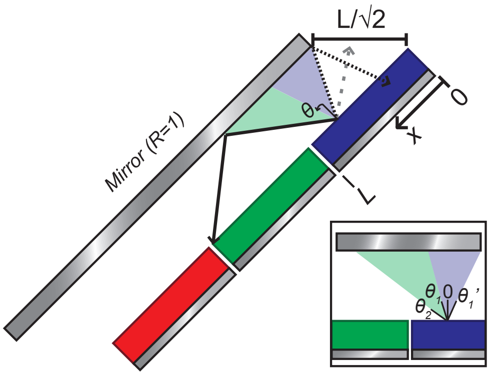

FIGURE F.1: Schematic of the 45° polyhedral specular reflector (PSR) design studied. The blue cone represents the angular range of photons that are reflected back into the same subcell at that example point. The green cone represents the range of angles of photons that are emitted into the next subcell. The inset shows the relevant angles for radiative emission discussed.

The fraction of photons reflected back onto the same subcell as a function of x is given by:

$$x = \frac{\int_{\theta_1'}^{\theta_1} cos(\alpha) d\alpha}{\int_0^{\pi/2} cos(\alpha) d\alpha} \tag{F.1}$$

The fraction of photons reflected back onto the same subcell averaged over the entire subcell:

$$x = \frac{\int_0^L sin(\theta_1(x)) - sin(\theta_1'(x)) dx}{\int_0^L dx} \tag{F.2}$$

This same process is repeated for determining the fraction of photons reflected to the next subcell. This yields a B_n of 0.204 for all subcells and an RB_n of 0.414 for all subcells except the first in the stack (n>1). The fraction of photons reflected back onto the same subcell is different for the first subcell (blue in Figure F.1) because the mirror does not completely cover the first subcell, which is a consequence of having the aperture wide enough to project the illuminated area across the whole length of the first subcell. Thus the RB_1 of the first subcell is 0.207.

It should also be noted that the geometry of the PSR (angle and aperture size) can be adjusted to yield different values for C_{geom}, RB, and B. For example, the aperture size can be reduced which will bring the mirror closer to the subcells, increasing the number of angles that fall within the cone of light that is reflected back into the same subcell (increasing RB). However, this also reduces the concentration of incident light on each subcell and reduces the number of downshifted photons (B). Additionally, the angle of the PSR can be reduced. This will decrease the concentration loss (aperture to cell length ratio is smaller) but will reduce RB and B.

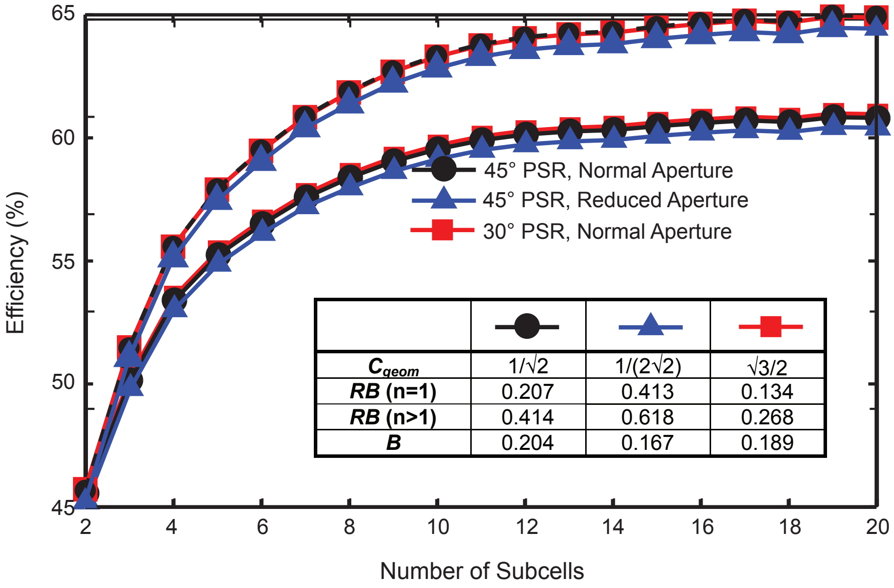

	●	▲	■
C_{geom}	1/√2	1/(2√2)	√3/2
***RB* (n=1)**	0.207	0.413	0.134
***RB* (n>1)**	0.414	0.618	0.268
B	0.204	0.167	0.189

FIGURE F.2: Efficiency versus number of subcells for different PSR geometries: the 45° PSR presented in the thesis (black circle), a 45° PSR with a reduced input aperture size (blue triangle), and a 30° PSR (red square). The inset shows the relevant parameters (C_{geom}, RB, and B) for each geometry.

Figure F.2 shows the efficiency as a function of number of subcells for the three PSR geometries and the inset displays the values for C_{geom}, RB, and B. Although the reduced aperture 45° PSR has a much larger RB because of the new mirror spacing, the reduced concentration reduces the overall efficiency beyond any additional light trapping benefit. Additionally, changing the angle of the PSR to 30° slightly increases the efficiency for a 2 and 3 subcell structure but slightly decreases the efficiency beyond the 45° PSR for cells with 4 or more subcells. The 30° PSR has smaller RB and B values than the original 45° PSR but it has a significantly larger concentration factor. Therefore for a small number of subcells (<4), the concentration factor is more important and the 30° PSR is most efficient. For a larger number of subcells ($/geq4$), the increased light trapping and radiative coupling of the 45° PSR makes it more efficient than the 30° PSR. Therefore the geometry of the PSR can be optimized depending on the number of subcells and performance of the optical components.

Bibliography

[1] Weston A. Hermann. Quantifying global exergy recources. *Energy*, 31(12):1685–1702, 2006. doi: http://dx.doi.org/10.1016/j.energy.2005.09.006.

[2] Richard Perez, Ken Zweibel, and Thomas E. Hoff. Solar power generation in the us: Too expensive, or a bargain? *Energy Policy*, 39(11):7290–7297, 2011. doi: http://dx.doi.org/10.1016/j.enpol.2011.08.052.

[3] Energy Information Administration. Annual energy outlook 2014, 2014.

[4] Emily Cathryn Warmann. *Design strategies for ultra-high efficiency photovoltaics.* PhD thesis, California Institute of Technology, 2014.

[5] W Shockley and H J Queisser. Detailed Balance Limit of Efficiency of P-N Junction Solar Cells. *Journal of Applied Physics*, 32(3):510–&, 1961. doi: 10.1063/1.1736034.

[6] Jeffery L Gray. The Physics of the Solar Cell. In A Luque and S Hegedus, editors, *Handbook of Photovoltaic Science and Engineering*, pages 102–104. John Wiley & Sons, West Sussex, United Kingdom, 2003.

[7] Martin A Green. *Third Generation Photovoltaics: Advanced Solar Energy Conversion.* Springer-Verlag, Berlin, Heidelberg, 2003.

[8] Martin A Green, Keith Emery, Yoshihiro Hishikawa, Wilhelm Warta, and Ewan D Dunlop. Solar cell efficiency tables (version 46). *Progress in Photovoltaics: Research and Applications*, 23(7):805–812, 2015. doi: 10.1002/pip.2637.

[9] A Polman and H A Atwater. Photonic design principles for ultrahigh-efficiency photovoltaics. *Nature Materials*, 11(3):174–177, 2012. doi: 10.1038/nmat3263.

[10] Martin A Green. Radiative efficiency of state-of-the-art photovoltaic cells. *Progress in Photovoltaics: Research and Applications*, 20(4):472–476, 2012. doi: 10.1002/pip.1147.

[11] O D Miller. Strong Internal and External Luminescence as Solar Cells Approach the Shockley–Queisser Limit. *IEEE Journal of Photovoltaics*, 2(3):303, 2012.

[12] E D Kosten, J H Atwater, J Parsons, A Polman, and H A Atwater. Highly efficient GaAs solar cells by limiting light emission angle. *Light: Science and Applications*, 2(e45), 2013. doi: http://dx.doi.org/10.1038/lsa.2013.1.

[13] Emily D. Kosten, Brendan M. Kayes, and Harry A. Atwater. Experimental demonstration of enhanced photon recycling in angle-restricted gaas solar cells. *Energy Environ. Sci.*, 7:1907–1912, 2014. doi: 10.1039/C3EE43584A.

[14] B M Kayes, Nie Hui, R Twist, S G Spruytte, F Reinhardt, I C Kizilyalli, and G S Higashi. 27.6% Conversion efficiency, a new record for single-junction solar cells under 1 sun illumination. In *Photovoltaic Specialists Conference (PVSC), 2011 37th IEEE*, pages 4–8, 2011. ISBN 0160-8371. doi: 10.1109/pvsc.2011.6185831.

[15] S P Philipps, A W Bett, K Horowitz, and S Kurtz. Current Status of Concentrator (CPV) Technology, 2015.

[16] Richard M. Swanson. The promise of concentrators. *Progress in Photovoltaics: Research and Applications*, 8(1):93–111, 2000. ISSN 1099-159X. doi: 10.1002/(SICI)1099-159X(200001/02)8:1⟨93::AID-PIP303⟩3.0.CO;2-S.

[17] Darby L Winn, Michael J Hale, Tyler J Grassman, Jonathan Z Sexton, Andrew C Kummel, Matthias Passlack, and Ravi Droopad. Electronic properties of adsorbates on gaas(001)-c(2x8)/(2x4). *The Journal of chemical physics*, 127(13):134705, October 2007. ISSN 0021-9606. doi: 10.1063/1.2786097.

[18] S.R. Bank, L.L. Goddard, Mark A. Wistey, Homan B. Yuen, and James S. Harris. On the temperature sensitivity of 1.5- mu;m gainnassb lasers. *Selected Topics in Quantum Electronics, IEEE Journal of*, 11(5):1089–1098, Sept 2005. ISSN 1077-260X. doi: 10.1109/JSTQE.2005.853852.

[19] Nelson Tansu, Jeng-Ya Yeh, and Luke J Mawst. Physics and characteristics of high performance 1200 nm ingaas and 1300–1400 nm ingaasn quantum well lasers obtained by metal–organic chemical vapour deposition. *Journal of Physics: Condensed Matter*, 16(31):S3277, 2004.

[20] Michael Wiemer, Vijit Sabnis, and Homan Yuen. 43.5% efficient lattice matched solar cells. page 810804, 2011. doi: 10.1117/12.897769.

[21] Jongho Lee, Jian Wu, Mingxing Shi, Jongseung Yoon, Sang-Il Park, Ming Li, Zhuangjian Liu, Yonggang Huang, and John A Rogers. Stretchable GaAs Photovoltaics with Designs That Enable High Areal Coverage. *Adv. Mater.*, 23(8): 986–991, 2011. doi: 10.1002/adma.201003961.

[22] Sarah Kurtz and John Geisz. Multijunction solar cells for conversion of concentrated sunlight to electricity. *Opt. Express*, 18(S1):A73–A78, Apr 2010. doi: 10.1364/OE.18.000A73.

[23] C J Sandroff, M S Hedge, and C C Chang. Structure and Stability of Passivating Arsenic Sulfide Phases on GaAs-Surfaces. *J Vac Sci Technol B*, 7(4):841–844, 1989.

[24] S R Lunt, G N Ryba, P G Santangelo, and N S Lewis. Chemical studies of the passivation of GaAs surface recombination using sulfides and thiols. *Journal of Applied Physics*, 70(12):7449–7467, 1991.

[25] S R Lunt, P G Santangelo, and N S Lewis. Passivation of GaAs surface recombination with organic thiols. *Journal of Vacuum Science and Technology B*, 9(4): 2333–2336, 1991.

[26] V L Berkovits, V P Ulin, D Paget, J E Bonnet, T V L'vova, P Chiaradia, and V M Lantratov. Chemical and photochemical processes in sulfide passivation of GaAs(100): In situ optical study and photoemission analysis. *J Vac Sci Technol A*, 16(4):2528–2538, 1998.

[27] Weichao Wang, Geunsik Lee, Min Huang, Robert M Wallace, and Kyeongjae Cho. First-principles study of GaAs(001)-beta 2(2x4) surface oxidation and passivation with H, Cl, S, F, and GaO. *J Appl Phys*, 107(10):103720, 2010. doi: 10.1063/1.3369540.

[28] N Dmitruk, O Borkovskaya, and I Mamontova. Sulfide passivation of a textured interface of a gallium arsenide surface-barrier photovoltaic cell. *Technical Physics*, 1999.

[29] H Hasegawa, H Ishii, T Sawada, T Saitoh, S Konishi, Y A Liu, and H Ohno. Control of Fermi Level Pinning and Recombination Processes at GaAs-Surfaces by Chemical and Photochemical Treatments. *J Vac Sci Technol B*, 6(4):1184–1192, 1988.

[30] C Kirchner, M George, B Stein. . . , B Stein, W J Parak, H E Gaub, and M Seitz. Corrosion Protection and Long-Term Chemical Functionalization of Gallium Arsenide in an Aqueous Environment. *Advanced . . .* , 12(4):266–276, 2002.

[31] C S Liu and J F Kauffman. Excitation Power Dependence of Photoluminescence Enhancement from Passivated GaAs. *Applied Physics Letters*, 66(25):3504–3506, 1995.

[32] Lakshminarayana Polavarapu, Stefanos Mourdikoudis, Isabel Pastoriza-Santos, and Jorge Perez-Juste. Nanocrystal engineering of noble metals and metal chalcogenides: controlling the morphology, composition and crystallinity. *CrystEngComm*, 17:3727–3762, 2015. doi: 10.1039/C5CE00112A.

[33] I Schnitzer, E Yablonovitch, C Caneau, and T J Gmitter. Ultrahigh Spontaneous Emission Quantum Efficiency, 99.7and 72 *Applied Physics Letters*, 62(2):131–133, 1993.

[34] R Ranganathan and E Yablonovitch. Non-destructive testing by absolute room temperature photoluminescence quantum efficiency of GaAs solar cells. *Record of the 25th auunual PVSC*, 1996.

[35] V L Berkovits, V P Ulin, M Losurdo, P Capezzuto, G Bruno, G Perna, and V Capozzi. Wet chemical nitridation of GaAs (100) by hydrazine solution for surface passivation. *Applied Physics Letters*, 80:3739, 2002.

[36] M Skowronski, S T Neild, and R E Kremer. Location of energy levels of oxygen vacancy complex in GaAs. *Applied Physics Letters*, 57(9):902–904, 2009.

[37] Y Park and M Skowronski. Photoluminescence of GaAs doped with dimethylaluminum methoxide during organometallic vapor phase epitaxy. *Journal of Applied Physics*, 75(5):2640–2643, 1994.

[38] K C Shin, M H Kwark, M H Choi, M H Oh, and Y B Tak. Photochemical Investigation of the 1.356 eV Band and Stoichiometry in Undoped GaAs. *Journal of Applied Physics*, 65(2):736–741, 1989.

[39] Y Fu, M Willander, G B Chen, Y L Ji, and W Lu. Photoluminescence spectra of doped GaAs films. *Applied Physics A: Materials Science & Processing*, 79(3): 619–623, 2004.

[40] T Tiedje, E Yablonovitch, G D Cody, and B G Brooks. Limiting Efficiency of Silicon Solar-Cells. *Ieee T Electron Dev*, 31(5):711–716, 1984.

[41] D J Griffiths. *Introduction to Electrodynamics*. Prentice-Hall, Inc, Upper Saddle River, 3rd edition, 1999.

[42] C H Henry, R A Logan, and F R Merritt. Effect of Surface Recombination on Current in AlxGa1-xAs Heterostructures. *Journal of Applied Physics*, 49(6):3530–3542, 1978.

[43] S P Tobin, S M Vernon, C Bajgar, S J Wojtczuk, M R Melloch, A Keshavarzi, T B Stellwag, S Venkatensan, M S Lundstrom, and K A Emery. Assessment of MOCVD-Grown and MBE-Grown GaAs for High-Efficiency Solar-Cell Applications. *Ieee T Electron Dev*, 37(2):469–477, 1990.

[44] P D Demoulin, S P Tobin, M S Lundstrom, M S Carpenter, and M R Melloch. Influence of Perimeter Recombination on High-Efficiency GaAs P/N Heteroface Solar-Cells. *Ieee Electr Device L*, 9(8):368–370, 1988.

[45] J S Blakemore. Semiconducting and Other Major Properties of Gallium-Arsenide. *Journal of Applied Physics*, 53(10):R123–R181, 1982.

[46] C. Donolato. Theory of beam induced current characterization of grain boundaries in polycrystalline solar cells. *Journal of Applied Physics*, 54(3):1314–1322, 1983. doi: http://dx.doi.org/10.1063/1.332205.

[47] Richard Corkish, Tom Puzzer, A. B. Sproul, and Keung L. Luke. Quantitative interpretation of electron-beam-induced current grain boundary contrast profiles with application to silicon. *Journal of Applied Physics*, 84(10):5473–5481, 1998. doi: http://dx.doi.org/10.1063/1.368310.

[48] G. Micard, G. Hahn, A. Zuschlag, S. Seren, and B. Terheiden. Quantitative evaluation of grain boundary activity in multicrystalline semiconductors by light beam induced current: An advanced model. *Journal of Applied Physics*, 108(3): 034516, 2010. doi: http://dx.doi.org/10.1063/1.3462447.

[49] Simon M. Sze and Kwok K. Ng. *Physics of Semiconductor Devices*. John Wiley & Sons, Hoboken, New Jersey, 2007.

[50] E Yablonovitch, T J Gmitter, and R Bhat. Inhibited and Enhanced Spontaneous Emission from Optically Thin AlGaAs GaAs Double Heterostructures. *Phys. Rev. Lett.*, 61(22):2546–2549, 1988.

[51] B A Kuruvilla, S V Ghaisas, A Datta, S Banerjee, and S K Kulkarni. Passivation of GaAs (100) Using Selenium Sulfide. *Journal of Applied Physics*, 73(9):4384–4387, 1993. doi: 10.1063/1.352775.

[52] C H Henry. Limiting Efficiencies of Ideal Single and Multiple Energy-Gap Terrestrial Solar-Cells. *Journal of Applied Physics*, 51(8):4494–4500, 1980.

[53] A Marti and G L Araujo. Limiting efficiencies for photovoltaic energy conversion in multigap systems. *Solar Energy Materials and Solar Cells*, 43(2):203–222, 1996. doi: 10.1016/0927-0248(96)00015-3.

[54] G L Araujo and A Marti. *On the Detailed Balance Limit of Ideal Multiple Bandgap Solar Cells*. 1991. ISBN 0-87942-636-5. doi: 10.1109/pvsc.1991.169226.

[55] A G Imenes and D R Mills. Spectral beam splitting technology for increased conversion efficiency in solar concentrating systems: a review. *Solar Energy Materials and Solar Cells*, 84(1-4):19–69, 2004. doi: 10.1016/j.solmat.2004.01.038.

[56] B Mitchell, G Peharz, G Siefer, M Peters, T Gandy, J C Goldschmidt, J Benick, S W Glunz, A W Bett, and F Dimroth. Four-junction spectral beam-splitting photovoltaic receiver with high optical efficiency. *Progress in Photovoltaics*, 19(1): 61–72, 2011. doi: 10.1002/pip.988.

[57] A Barnett, C Honsberg, D Kirkpatrick, S Kurtz, D Moore, D Salzman, R Schwartz, J Gray, S Bowden, K Goossen, M Haney, D Aiken, M Wanlass, and K Emery. 50% Efficient Solar Cell Architectures and Designs. In *Photovoltaic Energy Conversion, Conference Record of the 2006 IEEE 4th World Conference on*, volume 2, pages 2560–2564, 2006.

[58] C N Eisler, E C Warmann, C A Flowers, M Dee, E D Kosten, and H A Atwater. Design Improvements for Polyhedral Specular Reflector Spectum-Splitting Module for Ultra-High Efficiency (¿50%). In *41st IEEE Photovoltaics Specialists Conference*, Denver, CO, 2014.

[59] C N Eisler, E D Kosten, E C Warmann, and H A Atwater. Spectrum Splitting Photovoltaics: Polyhedral Specular Reflector Design for Ultra-High Efficiency Modules. In *Photovoltaic Specialists Conference (PVSC), 2013 39th IEEE*, Tampa, FL, 2013.

[60] E D Kosten, J Lloyd, E C Warmann, and H A Atwater. Spectrum Splitting Photovoltaics: Light Trapping Filtered Concentrator for Ultrahigh Photovoltaic Efficiency. In *Photovoltaic Specialists Conference (PVSC), 2013 39th IEEE*, Tampa, FL, 2013.

[61] M Escarra, S Darbe, E C Warmann, and H A Atwater. Spectrum-Splitting Photovoltaics: Holographic Spectrum Splitting in Eight-Junction, Ultra-high Efficiency Module. In *IEEE PVSC*, Tampa, FL, 2013.

[62] E C Warmann, C N Eisler, E D Kosten, M Escarra, and H A Atwater. Spectrum Splitting Photovoltaics: Proposed Band Gaps and Materials to Achieve 50% System Efficiency. In *Photovoltaic Specialists Conference (PVSC), 2013 39th IEEE*, 2013.

[63] M Ellion Edmund. High Efficiency Photovoltaic Assembly, 1987.

[64] Vidya Ganapati. *Optical Design Considerations for High Conversion Efficiency in Photovoltaics*. PhD thesis, University of California at Berkeley, 2015.

[65] J. F. Geisz, M. A. Steiner, I. García, S. R. Kurtz, and D. J. Friedman. Enhanced external radiative efficiency for 20.8single-junction gainp solar cells. *Applied Physics Letters*, 103(4), 2013. doi: http://dx.doi.org/10.1063/1.4816837.

[66] Stéphane Larouche and Ludvik Martinu. Openfilters: open-source software for the design, optimization, and synthesis of optical filters. *Appl. Opt.*, 47(13):C219–C230, May 2008. doi: 10.1364/AO.47.00C219.

[67] W. T. Welford and Roland Winston. *High Collection Nonimaging Optics*. Academic Press, Inc., California, USA, 1989.

[68] C A Flowers, C N Eisler, and H A Atwater. Electrically Independent Subcircuits for a Seven-Junction Spectrum- Splitting Photovoltaic Module. In *IEEE Photovoltaics Specialists Conference*, Denver, CO, 2014.

[69] Marc Steiner, Simon P Philipps, Martin Hermle, Andreas W Bett, and Frank Dimroth. Validated front contact grid simulation for GaAs solar cells under concentrated sunlight. *Progress in Photovoltaics: Research and Applications*, 19(1): 73–83, 2011. doi: 10.1002/pip.989.

[70] A R Moore. An optimized grid design for a sun-concentrator solar cell. *RCA Review*, 40:140–152, 1979.

[71] SolarEdge. Power Optimizer Specifications - P600 / P700, 2015. URL http://www.solaredge.com/files/pdfs/products/power-optimizers/p-series-commercial-us-application-note.pdf.

[72] A Antonini, M Stefancich, D Vincenzi, C Malagù, F Bizzi, A Ronzoni, and G Martinelli. Contact grid optimization methodology for front contact concentration solar cells. *Solar Energy Materials and Solar Cells*, 80(2):155–166, 2003. doi: http://dx.doi.org/10.1016/j.solmat.2003.07.001.

[73] J Scott Ward, Anna Duda, Daniel J Friedman, John Geisz, William McMahon, and Michelle Young. High aspect ratio electrodeposited Ni/Au contacts for GaAs-based III–V concentrator solar cells. *Progress in Photovoltaics: Research and Applications*, 23(5):646–653, 2015. doi: 10.1002/pip.2490.

[74] I García, I Rey-Stolle, B Galiana, and C Algora. A 32.6% efficient lattice-matched dual-junction solar cell working at 1000 suns. *Applied Physics Letters*, 94(5):53509, 2009. doi: doi:http://dx.doi.org/10.1063/1.3078817.

[75] C.F.R. Mateus, M.C.Y. Huang, Yunfei Deng, Andrew R. Neureuther, and C.J. Chang-Hasnain. Ultrabroadband mirror using low-index cladded subwavelength grating. *Photonics Technology Letters, IEEE*, 16(2):518–520, Feb 2004. ISSN 1041-1135. doi: 10.1109/LPT.2003.821258.

[76] Isabelle Staude, Andrey E. Miroshnichenko, Manuel Decker, Nche T. Fofang, Sheng Liu, Edward Gonzales, Jason Dominguez, Ting Shan Luk, Dragomir N. Neshev, Igal Brener, and Yuri Kivshar. Tailoring directional scattering through magnetic and electric resonances in subwavelength silicon nanodisks. *ACS Nano*, 7(9):7824–7832, 2013. doi: 10.1021/nn402736f. PMID: 23952969.

[77] Parikshit Moitra, Brian A. Slovick, Zhi Gang Yu, S. Krishnamurthy, and Jason Valentine. Experimental demonstration of a broadband all-dielectric metamaterial perfect reflector. *Applied Physics Letters*, 104(17):171102, 2014. doi: http://dx.doi.org/10.1063/1.4873521.

[78] Vadim Karagodsky and Connie J. Chang-Hasnain. Physics of near-wavelength high contrast gratings. *Opt. Express*, 20(10):10888–10895, May 2012. doi: 10.1364/OE.20.010888.

[79] Nanfang Yu, Patrice Genevet, Mikhail A. Kats, Francesco Aieta, Jean-Philippe Tetienne, Federico Capasso, and Zeno Gaburro. Light propagation with phase

discontinuities: Generalized laws of reflection and refraction. *Science*, 334(6054): 333–337, 2011. doi: 10.1126/science.1210713.

[80] A.J.M. van Erven, M. Steltenpool, M. Bos, J. Rutten, G. van der Hofstad, J. Muller, H. de Groot, J. de Ruijter, A. Tavakoliyaraki, B. Titulaer, and G. Rajeswaran. Gen5 production tool for light management textures. In *Photovoltaic Specialists Conference (PVSC), 2012 38th IEEE*, pages 000690–000693, June 2012. doi: 10.1109/PVSC.2012.6317703.

[81] S Darbe and H A Atwater. Resonant dielectric high-contrast gratings as spectrum splitting optical elements for ultrahigh efficiency (¿50In *IEEE PVSC*, New Orleans, LA, 2015.

[82] Y Yao, H Liu, and W Wu. Fabrication of High Contrast Gratings for the Spectrum Splitting Dispersive Element in a Concentrated Photovoltaic System. *J. Vis. Exp.*, 101, 2015. doi: 10.3791/52913.

[83] NREL. Nrel levelized cost of energy calculator, 2015. URL `http://www.nrel.gov/analysis/tech_lcoe.html`.

[84] Vasilis M. Fthenakis and Hyung Chul Kim. Life cycle assessment of high-concentration photovoltaic systems. *Progress in Photovoltaics: Research and Applications*, 21(3):379–388, 2013. ISSN 1099-159X. doi: 10.1002/pip.1186.

[85] Martin A Green, Keith Emery, Yoshihiro Hishikawa, Wilhelm Warta, and Ewan D Dunlop. Solar cell efficiency tables (version 41). *Progress in Photovoltaics: Research and Applications*, 21(1):1–11, 2013. doi: 10.1002/pip.2352.

[86] Carsten Baur, Martin Hermle, Frank Dimroth, and Andreas W Bett. Effects of optical coupling in III-V multilayer systems. *Applied Physics Letters*, 90(19): 192103–192109, 2007. doi: 10.1063/1.2737927.

[87] M A Steiner, J F Geisz, T E Moriarty, R M France, W E McMahon, J M Olson, S R Kurtz, and D J Friedman. Measuring IV Curves and Subcell Photocurrents in the Presence of Luminescent Coupling. *Photovoltaics, IEEE Journal of*, PP(99): 1–9, 2012. doi: 10.1109/jphotov.2012.2228298.

[88] D J Friedman, J F Geisz, and M A Steiner. Analysis of Multijunction Solar Cell Current–Voltage Characteristics in the Presence of Luminescent Coupling. *Photovoltaics, IEEE Journal of*, 3(4):1429–1436, 2013. doi: 10.1109/jphotov.2013.2275189.

[89] Andrew S Brown and M A Green. Radiative coupling as a means to reduce spectral mismatch in monolithic tandem solar cell stacks theoretical considerations. In *Photovoltaic Specialists Conference, 2002. Conference Record of the Twenty-Ninth IEEE*, pages 868–871, 2002. ISBN 1060-8371. doi: 10.1109/pvsc.2002.1190717.

[90] A De Vos. Detailed Balance Limit of the Efficiency of Tandem Solar-Cells. *Journal of Physics D-Applied Physics*, 13(5):839–846, 1980.

[91] A De Vos. *Thermodynamics of Solar Energy Conversion.* Wiley-VCH, Verlag, Weinheim, 2008.

[92] Viorel Badescu, Alexis De Vos, Alina Mihaela Badescu, and Aleksandra Szymanska. Improved model for solar cells with down-conversion and down-shifting of high-energy photons. *Journal of Physics D-Applied Physics*, 40(2):341–352, 2007. doi: 10.1088/0022-3727/40/2/009.

[93] Zeev R Abrams, Avi Niv, and Xiang Zhang. Solar energy enhancement using down-converting particles: A rigorous approach. *Journal of Applied Physics*, 109 (11), 2011. doi: 10.1063/1.3592297.

[94] Andrew S Brown. *Ultimate Efficiency Limits of Multiple Energy Threshold Photovoltaic Devices.* PhD thesis, 2003.

[95] Martin A Green. Time-Asymmetric Photovoltaics. *Nano Letters*, 12(11):5985–5988, 2012. doi: 10.1021/nl3034784.

[96] Martin A Green. Analytical treatment of Trivich-Flinn and Shockley-Queisser photovoltaic efficiency limits using polylogarithms. *Progress in Photovoltaics*, 20 (2):127–134, 2012. doi: 10.1002/pip.1120.

[97] A De Vos and H Pauwels. On the thermodynamic limit of photovoltaic energy conversion. *Applied Physics A: Materials Science & Processing*, 25(2):119–125, 1981. doi: 10.1007/bf00901283.

[98] R T Ross. Some Thermodynamics of Photochemical Systems. *Journal of Chemical Physics*, 46(12):4590–&, 1967. doi: 10.1063/1.1840606.

[99] W Ruppel and P Wurfel. Upper Limit for the Conversion of Solar-Energy. *Ieee Transactions on Electron Devices*, 27(4):877–882, 1980. doi: 10.1109/t-ed.1980.19950.

[100] Carissa N Eisler, Ze'ev R Abrams, Matthew T Sheldon, Xiang Zhang, and Harry A Atwater. Multijunction solar cell efficiencies: effect of spectral window, optical environment and radiative coupling. *Energy & Environmental Science*, 7(11):3600–3605, 2014. doi: 10.1039/c4ee01060d.

[101] U Ortabasi, A Lewandowski, R McConnell, Daniel J Aiken, P L Sharps, and B G Bovard. Dish/photovoltaic cavity converter (PVCC) system for ultimate solar-to-electricty conversion efficiency-general concept and first performance predictions. In *Photovoltaic Specialists Conference, 2002. Conference Record of the Twenty-Ninth IEEE*, pages 1616–1620, 2002. ISBN 1060-8371. doi: 10.1109/pvsc.2002.1190925.